Density Functional Theory Calculations on the Sorption of Organoarsenicals onto Hydrated Iron (III) Oxyhydroxide Clusters

by

Adrian Adamescu

A thesis
presented to the University of Waterloo
in fulfillment of the
thesis requirement for the degree of
Doctor of Philosophy
in
Chemistry

Waterloo, Ontario, Canada, 2017

Examining Committee Membership

The following served on the Examining Committee for this thesis. The decision of the Examining Committee is by majority vote.

External Examiner	NAME: Dr. Randall Dumont Title: Associate Professor
Supervisor(s)	NAME: Dr. Marcel Nooijen Title: Associate Professor
	NAME: Dr. Ian Hamilton Title: Professor
	NAME: Dr. Hind Al-Abadleh Title: Associate Professor
Internal Member	NAME: Dr. Pierre-Nicholas Roy Title: Professor
Internal-external Member	NAME: Dr. Philippe Van Cappellen Title: Canada Excellence Research Chair
Other Member(s)	NAME: Dr. Michael Denk Title: Associate Professor
	NAME: Dr. Carol Ptacek Title: Professor

Author's Declaration

I hereby declare that I am the sole author of this thesis. This is a true copy of the thesis, including any required final revisions, as accepted by my examiners. I understand that my thesis may be made electronically available to the public.

Abstract

Organic forms of arsenic are introduced into the environment by natural and anthropogenic processes and they pose a threat to human health. The fate of these pollutants depends on their interactions with reactive soils components, such as iron oxyhydroxides. Reaction pathway information and transition states are essential for understanding adsorption mechanisms of pollutants at the liquid–solid interface. Density functional theory (DFT) calculations on the energies, optimal geometries, vibrational frequencies for organic arsenical complexes, p-arsanilic acid (pAsA), monomethylarsonic acid (MMA) and dimethylarsinic acid (DMA) with iron oxyhydroxide clusters are performed. In addition, changes in Gibbs free energy, enthalpy, and entropy for various types of ligand exchange reactions leading to both inner- and outer-sphere complexes are presented, along with activation barriers and transition states. Results are compared to calculations using the well-studied arsenate system and various experiments that use surface sensitive techniques.

DFT calculations show that the formation of inner- and outer-sphere complexes with pAsA, MMA and DMA is thermodynamically favourable, but also that the activation barriers are crucial in understanding the types of complexes that form. It is shown that the mono-substituted arsenicals, pAsA and MMA, are more likely to form inner-sphere complexes, but that the di-substituted DMA, may be hindered to do so because of higher activation barriers along its reaction pathway.

The calculations reported herein include explicit and implicit solvation, as well as dispersion corrections, that are shown to be particularly useful for calculations where outer-sphere complexes are involved. Calculations include both a smaller iron oxyhydroxide surface with 2 Fe atoms at its core and an extended iron oxyhydroxide surface with 4 Fe atoms at its core. The 4Fe geometries were shown to be particularly important for outer-sphere and monodentate complexes where the 2Fe complexes suffered from an over-relaxation problem that overestimates the stability of a complex.

The Mulliken charge distribution analysis performed on the DMA systems revealed that there is no charge transferred in the formation of the outer-sphere complexes, suggesting outer-sphere complex formation is purely electrostatic while charge is transferred from the ligand to the metal when inner-sphere complexes form. The theoretical infrared spectra for pAsA, DMA and MMA are compared to experimental results and the formation of outer-sphere and inner-sphere complexes are discussed. The theoretical frequencies are also used to calculate a new scaling factor (F=1.0065) to correct the stretching vibrations of the As-O bond of organoarsenicals for anharmonicity.

Acknowledgments

I would like to thank my supervisors Dr. Marcel Nooijen, Dr. Hind Al-Abadleh and Dr. Ian Hamilton for giving me the opportunity to work with them. The help and guidance they provided throughout my journey as a PhD student is immeasurable and I have nothing to offer but gratitude. Working with them has been a pleasure from start to finish and I wish them the best as I move on to my next step in life. In addition, I would also like to thank my committee members Dr. Pierre-Nicholas Roy, Dr. Michael Denk, Dr. Carol Ptacek and Dr. Philippe Van Cappellen for their advice and valuable input during our meetings and in the writing of this thesis. Thank you also to my external examiner Dr. Randall Dumont who asked great questions and pointed out some key corrections. Thank you to all the past and current members of our research group who have provided me with a lot of helpful input during group meetings.

Thank you to my parents Mariana and Mircea and my sister Alina. I'm proud of you all for being so strong and I'm proud of my father for pulling through. I have witnessed a miracle to see my father come back to life after his heart attack. I would like to say a special thank you to my beautiful wife Andreea. I couldn't have done it without your help and encouragement. You are a blessing from above. I love you.

Soli Deo gloria!

Table of Contents

List of Figures

List of Tables

CHAPTER I. Introduction

1.1 Arsenicals in the Environment

Arsenic (As) is the 20th most abundant element in the Earth's crust and occurs naturally in over 200 different minerals, and is released into the environment by the weathering of rocks. Arsenic concentrations in soil can range from 1 to 40 parts per million (ppm) depending on the local geology, but are on average around 3–4 ppm and it occurs mostly in the form of inorganic arsenic (iAs).[1] Arsenic compounds can also be biomethylated by microbes like *Escherichia coli*, *Flavobacterium* sp. and *Methanobacterium* sp., as well as fungi such as *Aspergillus glaucus*, *Candida humicola* to form organoarsenicals, such as monomethylarsonic acid (MMA), dimethylarsinic acid (DMA), and trimethylarsine oxide (TMA).[2,3] The biomethylation process proposed by Challenger in 1945 involves a stepwise reduction and oxidative methylation as shown in Figure 1.1.[4,5]

Under oxidizing conditions, in aerobic environments, arsenate, H_3AsO_4, is the stable species and is strongly sorbed onto clays, iron, aluminum and manganese oxyhydroxides, as well as organic matter.[6] Under reducing conditions, arsenite, H_3AsO_3, is the dominant arsenic compound and is more mobile and toxic. As seen in the redox potential (Eh) and pH diagram in Figure 1.2, $H_2AsO_4^-$ is the dominant arsenate species at low pH (under pH 6.9) in oxidising conditions, but at higher pH, $HAsO_4^{2-}$ becomes dominant. The H_3AsO_4 and AsO_4^{3-} species may be present in

extremely acidic and alkaline conditions, respectively. Under reducing conditions at pH less than about pH 9.2, the uncharged arsenite species H_3AsO_3 will dominate.[7,8]

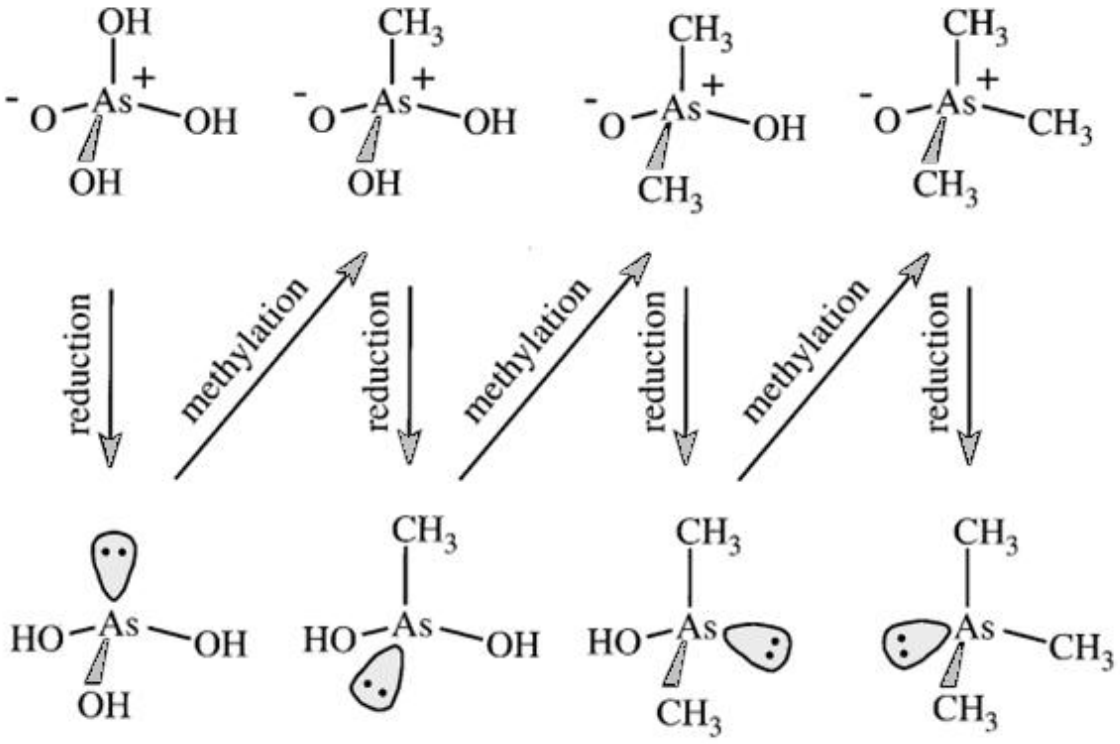

Figure 1.1 The reduction steps in the Challenger Mechanism involve the formation of arsenicals with a lone pair of electrons on the arsenic atom, which then undergo methylation to form MMA, DMA and TMA species. Image reproduced after Bentley and Chasteen, 2002.[4]

There are also a number of anthropogenic sources of As that include mining, use of herbicides, combustion of fossil fuels, wood preservatives and feed additives in the poultry industry that enters the soil through the application of manure as fertilizers.[8] Arsenicals have also been detected in the leachates of landfills rich in waste containing As such as glass, alloys, and semiconductors.[9] Base-metal and gold (Au) production facilities are one of the major anthropogenic sources of As released in Canada. In 1992, MacLatchy estimated that about 15 tonnes of As were released annually by Canadian

base-metal smelters and refineries in liquid effluent, 310 tonnes per year were released into the atmosphere, and 770 tonnes per year were disposed of on land as solid waste.[10]

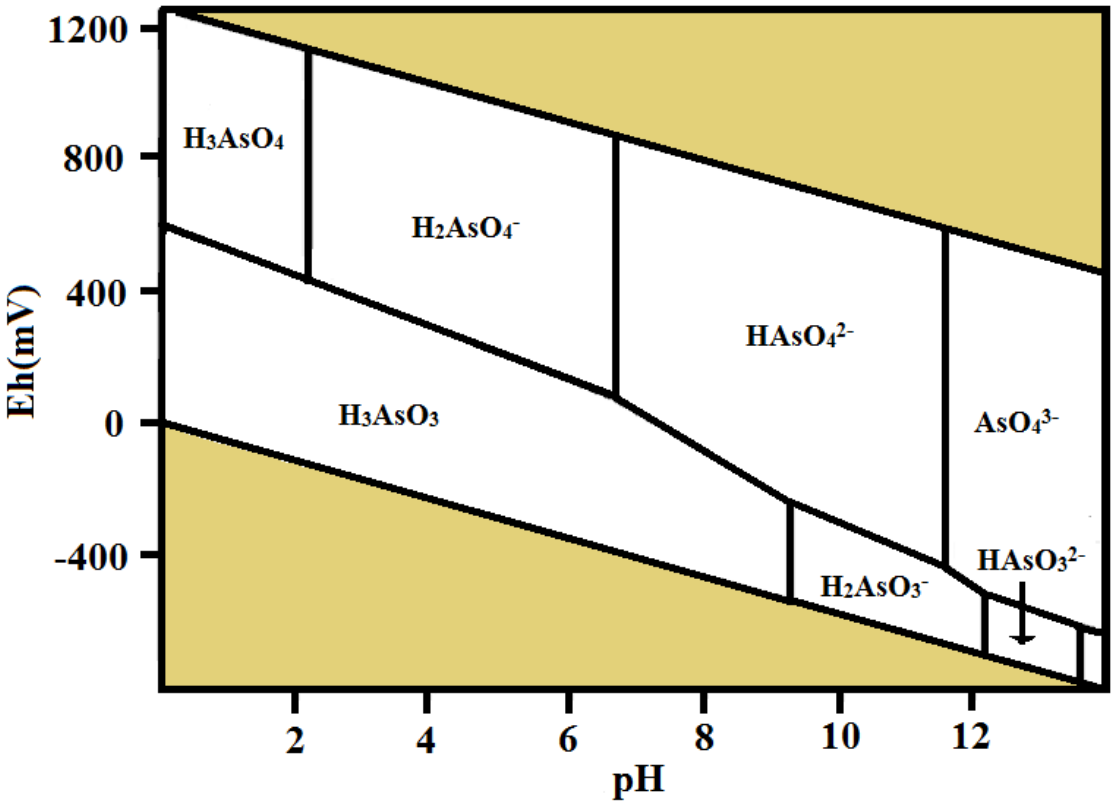

Figure 1.2 Eh-pH diagram for aqueous As species.
Image reproduced after Smedley and Kinniburgh, 2002.[8]

Organic species of arsenic also have had wide human applications in recent decades. Some of the most important are DMA and MMA used as pesticides and herbicides on golf courses and agricultural lands. For example, in 1990 alone, approximately 2700 metric tons of MMA were used on cotton fields in the US. In Canada, MMA use started in 1980 to prevent the destruction of forests in British Columbia from attack of the mountain pine beetle, but after further consideration of the potential harm, the application of MMA was no longer used after 2005.[11] Synthetic

aromatic organoarsenicals, such as p-arsanilic acid (pAsA) and 3-nitro-4-hydroxyphenylarsonic acid (roxarsone) were also frequently used as feed additives in the poultry and swine industries to improve feed efficiency, increase weight gain and help prevent against coccidiosis, a parasitic disease that infects the intestinal tracts of poultry.[12] The majority of these compounds re-enter the environment through poultry litter because they are not metabolized[13] and are used as fertilizers on agricultural lands.[14,15]

Table 1 shows the structures of three common organoarsenicals and their corresponding pK_a values.[16,17] Note that, due to their pK_a values, these organoarsenicals will have a single negative charge under a wide and environmentally relevant pH range. These three organoarsenicals and their interactions with positively charged iron oxyhydroxide clusters will be the focus of this thesis.

Table 1.1 Structures and pK_a values of some important organoarsenicals commonly identified in environmental samples.

Compound	Structure	pK_a values
Monomethylarsonic acid (**MMA**)	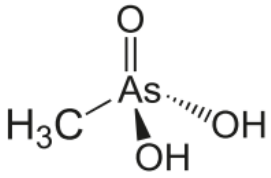	pK_{a1}: 3.6 pK_{a2}: 8.2
Dimethylarsinic acid (**DMA**)	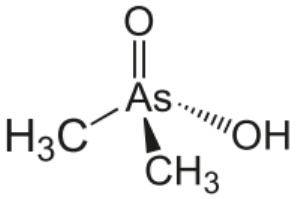	pK_{a1}: 6.14
p-Arsanilic acid (**pAsA**)	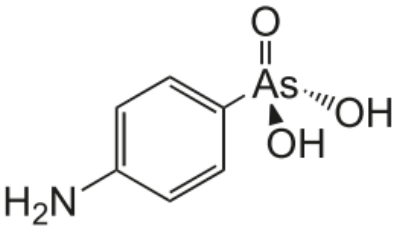	pK_{a1}: 1.9 ($-NH_3^+$) pK_{a2}: 4.1 pK_{a3}: 9.2

1.2 Toxicity of Arsenicals

Arsenic is very toxic and has been linked to many cancers of the bladder, lungs, skin, kidney, nasal passages, liver and prostate[18], as well as hypertension and other cardiometabolic diseases.[19] The toxicity of arsenic varies with the chemical form and the oxidation state of the species. One study reported the arsenicals of oxidation state three to be most toxic and showed the toxicity order of arsenic compounds in several cell lines to be DMA(III), MMA(III) > iAs(III) > iAs(V) > DMA(V), MMA(V).[20]

Of the various sources of As in the environment, drinking water poses the greatest threat to human health. The chronic exposure to arsenic in drinking water (even at small amounts) can cause arsenicosis.[21] The current World Health Organization (WHO) guideline value for As in drinking water is 10 μg/L or 10 parts per billion (ppb), but there are areas in the world that exceed many times this value. In various parts of Bangladesh, sources of drinking water have arsenic concentrations that exceed 100 ppb.[22]

1.3 Arsenic Removal

It is evident from the previous section that remediation technologies that can remove arsenic from drinking water and soils are essential. There are various methods that have been developed to deal with arsenicals such as treatments that include microbes to affect the bio-geochemical cycling of arsenic[23], electrocoagulation and electrodialysis[24] or the use of various minerals to immobilize arsenic such as dolomite[25], zeolites[26] and even copper doped hydroxyapatite[27]. Perhaps one of the most effective and cost efficient ways to remove arsenic though is using natural iron oxide minerals. Studies show that magnetite, hematite and goethite are very effective at binding arsenic over a wide pH range.[28] Even a small household method using laterite soil (a soil rich in iron and aluminum) has been shown to be very efficient in removing arsenic from drinking water, with concentrations decreasing from 20 ppm to less than 10 ppb after a few minutes of stirring.[29]

1.4 Studying the Surface Complexation of Arsenicals

Most environmental processes in geochemical systems occur at the liquid/solid interface. Hence, the study of arsenicals at the interface requires sophisticated surface sensitive techniques, such as Attenuated Total Reflectance Fourier Transform Infrared (ATR-FTIR) spectroscopy, and X-ray Absorption Spectroscopy (XAS) techniques such as X-ray Absorption Near Edge Structure (XANES) and Extended X-ray Absorption Fine Structure (EXAFS).

ATR-FTIR spectroscopy is based on the total internal reflection of an infrared (IR) beam of light inside a crystal of high refractive index, typically zinc selenide (ZnSe) or germanium (Ge) as shown in Figure 1.3 below. At the region of contact, an evanescent wave extends a few microns (0.5 – 5 μm) beyond the crystal and into the sample. In the regions of the IR spectrum where the sample absorbs energy, the evanescent wave will be attenuated while the energy from each evanescent wave is passed back to the IR beam. The IR beam is then reflected back out of the crystal and to the detector.[30] Short path lengths of a few microns are required to subtract out the signals of highly IR absorbing solvents, such as water. In this way the signal of the solutes becomes distinguishable.

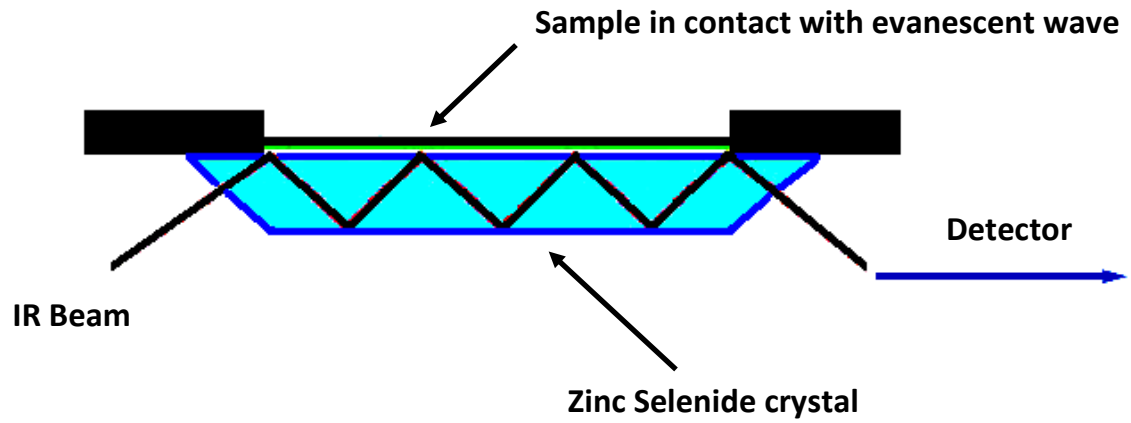

Figure 1.3 The workings of an ATR-FTIR system

In the case of arsenicals, the energy is absorbed due to the As-O stretching vibrations, ν(As-O), in the 600-1000 cm^{-1} range. When arsenicals form bonds to metal oxides the shifts in the frequencies of ν(As-O) can be used to study sorption and identify the types of surface complexation that occurs. For example, the change in the As-O stretching frequencies is seen in Figure 1.4 below, where the ν(As-O) signal of DMA in the bulk[31] (left) is compared to DMA adsorbed to hematite[32] (right). The DMA in the bulk data shows peaks around 879 and 831 cm^{-1} that are assigned to ν(As-O), as well as at 735 cm^{-1} assigned to ν(As-OH), while the DMA on hematite shows much broader spectral features that are indicative of simultaneous formation of inner and outer-sphere complexation. In this study, the observed downshifts at 793 and 775 cm^{-1} are assigned to ν(As-OFe) and are to be due to inner-sphere complex formation and changes in the vibrational freedom of DMA upon sorption to the iron oxide, while the 877 cm^{-1} peak is assigned to ν(As=O) in outer-sphere complexes and the 840 cm^{-1} to the un-complexed (i.e. free) ν(As-O), whose bond order could be influenced by either electron withdrawal

due to surface binding of the other As-O bond, electrostatic attraction with neighbouring electron deficient sites, or strong solvation effects.

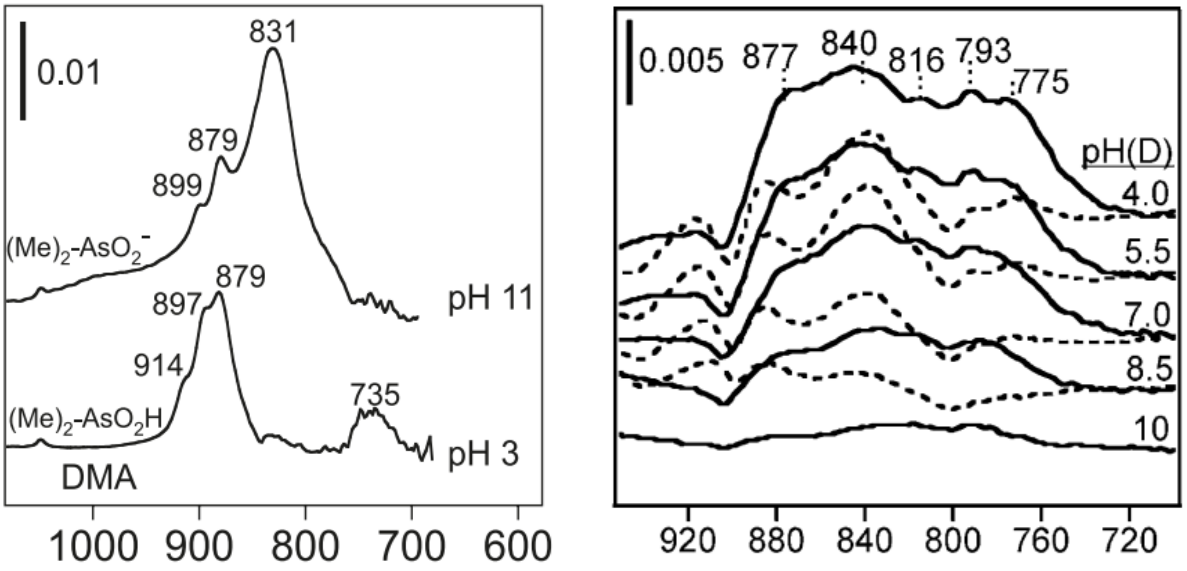

Figure 1.4 ATR-FTIR data showing DMA in the bulk (left) and the spectral shifts after sorption onto a hematite surface (right) at different pH (solid line) and pD (broken line) ranges. Re-used with permission from References 31 and 32.

In XANES and EXAFS, core electrons are ejected by an incident X-ray that exceeds the Ionization Energy (or Edge Energy) and the outgoing photoelectrons are studied as they interact with the scattered waves from their neighbouring atoms. The way EXAFS and XANES operate is also shown in Figure 1.5 below.

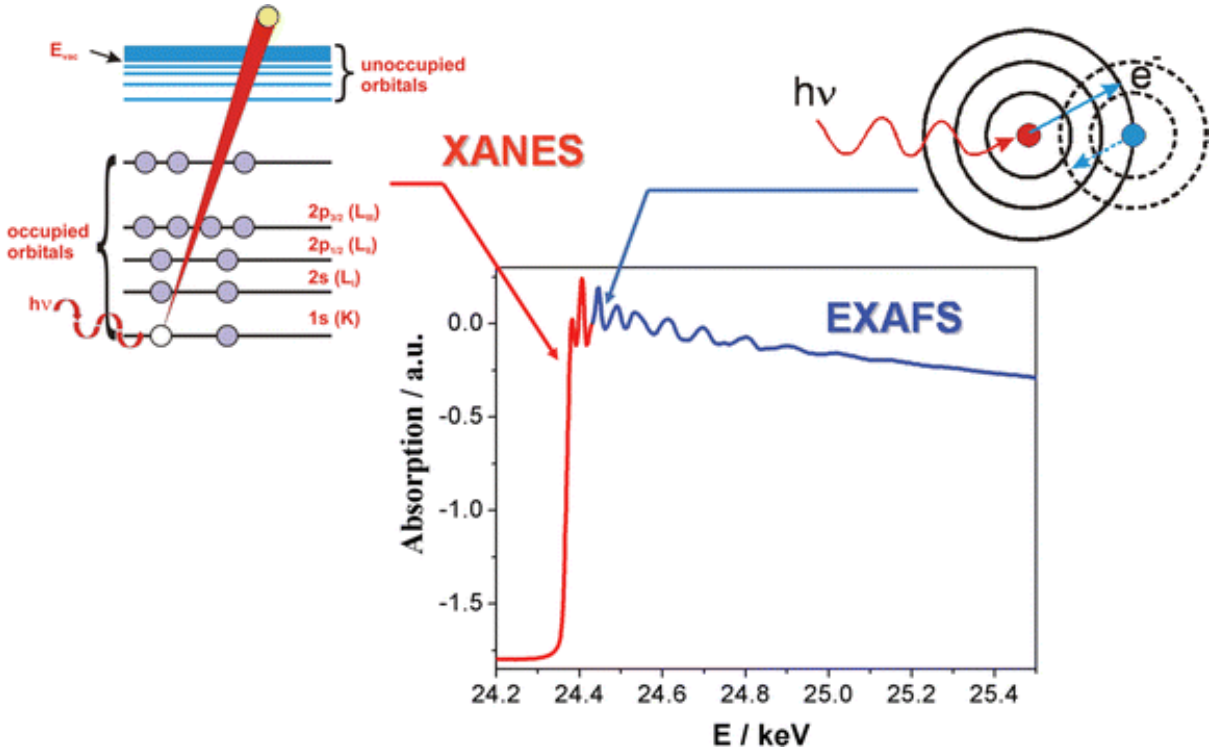

Figure 1.5 Data extracted from XANES and EXAFS experiments reveals information about an atom's coordination environment and inter-atomic distances. Image reproduced with permission from Grunwaldt and Baiker, 2005.[33]

Both methods contain different information about the coordination and chemical states of elements. The XANES region will have peaks, in the 5–150 eV range, that are formed by scattered waves from neighbouring atoms and can reveal detailed information about the oxidation state of the atoms, while the EXAFS region, in the higher energy ranges (beyond 150 eV), can reveal information about inter-atomic distances and coordination geometries.

1.5 The Computational Approach to Studying the Surface Complexation of Arsenic

The interaction of arsenicals with reactive soil particles at the water/solid interface will control their transport and bioavailability[34] and it is necessary to use the surface-sensitive techniques mentioned in the previous chapter to study these interactions. However, the addition of computational chemistry and density functional theory (DFT), in particular, to experimental studies can be very valuable. Calculations can provide molecular-level details about interfacial processes that aid in the interpretation of experimental data, can be used to improve the current predictive abilities of surface complexation models (SCMs) by incorporating binding mechanisms, and can also offer information that is hard to obtain experimentally.

A common example would be the use of DFT calculations in interpreting infrared data. The infrared spectra of arsenate, phosphate and other oxyanions onto iron oxides have been studied at length, but since the vibrational bands are quite broad, they can be difficult to interpret, resulting in different explanations for their binding mechanisms. Often times a mix of monodentate (MD) and bidentate (BD) configurations are being proposed[35,36,37,38] while other studies point out that outer-sphere (OS) complexes could not be ruled out.[39] DFT calculations are very valuable in answering many of these questions. There are numerous computational studies that looked at energies and binding thermodynamics,[40,41] transition states[42,43,44] and vibrational frequencies[45,46,47] that have given great insights about how various arsenicals interact with sorbents.

1.6 Thesis Objectives

The objectives of this thesis are to offer a detailed theoretical analysis on the interactions of a variety of organoarsenicals, specifically pAsA, MMA and DMA, with hydrated iron (III) oxyhydroxide surfaces using density functional theory. Calculations are performed to determine favourable complex formation, mechanisms of binding, reaction thermodynamics, activation barriers and transition states, and frequency calculations for comparison with experimental work. Calculations are meant to complement experimental data to offer a better understanding of the adsorption processes, offer help in infrared spectral interpretation and provide geometrical parameters that are useful for modeling X-ray absorption data using EXAFS.

In Chapter 2, density functional theory (DFT) and its theoretical foundations are discussed and an explanation given to the choices made for modelling the iron hydroxide surface with the solvation and dispersion models. Chapter 3 provides the theoretical data and an analysis of pAsA and iron oxyhydroxide clusters with two iron centres, including Gibbs free energies for sorption and desorption reactions, activation barriers and transition states and an analysis of the IR data in comparison with the experimental data. Calculations with dispersion corrections are also introduced and compared with calculations that do not include them. In Chapter 4, the DMA molecule and its interactions with iron oxyhydroxide clusters are examined. This chapter includes adsorption thermodynamics, infrared data and an in-depth analysis of the Mulliken charges upon adsorption. This chapter also introduces the extended iron hydroxide

surface with four iron centres and its effects on studying the sorption of arsenicals. Chapter 5 focuses on MMA in comparison with the arsenicals in the previous chapters and includes sorption reaction thermodynamics and an IR analysis using the extended iron oxyhydroxide surface. Chapter 6 gives the conclusions and significance of the work presented with practical applications and recommendations that will help further studies. In this final chapter, a correction factor is also provided that is more useful for low frequency calculations with iron and arsenic. The Appendices A through E, in respective order show the water molecules used as leaving groups in adsorption and desorption reactions, gives the optimized arsenate complexes that are used for comparison with the data for organoarsenicals in this thesis, presents the IRC calculation used to show how a transition state for DMA connects reactant to product, shows the MMA data for a complex without dispersion for comparison and gives the background data used in the calculation of a new correction factor.

CHAPTER II. Theoretical Background

"It is also a good rule not to put too much confidence in experimental results until they have been confirmed by theory." -- Sir Arthur Eddington

2.1 Density Functional Theory

The time-independent Schrödinger equation for an isolated N-electron molecular system using the Born-Oppenheimer approximation (that separates the nuclei and the electrons into separate mathematical problems) is given by

$$\hat{H}\Psi = E\Psi \qquad \text{(Equation 2.1)}$$

where E is the electronic energy, $\Psi = \Psi(x_1, x_2, \ldots, x_N)$ is the wave function and $\hat{H}$ is the Hamiltonian operator,

$$\hat{H} = \hat{T} + \hat{V}_{ne} + \hat{V}_{ee} \qquad \text{(Equation 2.2)}$$

where $\hat{T}$ is the kinetic energy operator

$$\hat{T} = \sum_{i=1}^{N} \left(-\frac{1}{2}\nabla_i^2\right) \qquad \text{(Equation 2.3)}$$

$\hat{V}_{ne}$ is the electron-nucleus attraction energy operator

$$\hat{V}_{ne} = \sum_{i=1}^{N} \upsilon(\bar{r}_i) \qquad \text{(Equation 2.4)}$$

$\hat{V}_{ee}$ is the electron-electron repulsion energy operator

$$\hat{V}_{ee} = \sum_{i<j}^{N} \frac{1}{\bar{r}_{ij}} \qquad \text{(Equation 2.5)}$$

Where Equations 2.2 – 2.5 use atomic units in which the mass of the electron, m_e = 1, the charge unit is the charge of the electron, *e*, and the length unit is the Bohr radius a_0 = 0.5292Å.

There are a few examples where the Hamiltonian has a simple form and the Schrödinger equation can be solved exactly, such as the particle in a box example and the hydrogen atom, but in real world scenarios where multiple electrons interact with multiple nuclei calculations become more complicated. The Schrödinger equation is a *many-body problem* and the electronic wave function cannot be found without simultaneously considering the individual wave functions associated with all the other electrons.

In Density Functional Theory (DFT)[48,49,50] this problem is addressed by introducing the electron density, $n(\vec{r})$. The electron density is obtained by integrating $\Psi^*\Psi$ over the coordinates of all the electrons except one. For a normalized Ψ it is given by:

$$n(\vec{r}) = N\int d^3r_2 \cdots \int d^3r_N \Psi^*(\vec{r},\vec{r}_2,...\vec{r}_N)\Psi(\vec{r},\vec{r}_2,...\vec{r}_N) \quad \text{(Equation 2.6)}$$

Unlike the wave function, the electron density is an observable (e.g. it can be measured experimentally by X-ray diffraction) and if it is integrated over all space it will give the total number of electrons, N.

$$\int n(\vec{r})d\vec{r} = N \quad \text{(Equation 2.7)}$$

Moreover, $n(\vec{r})$ is a function that will exhibit a maximum at a position of an atom, because of the attractive force exerted by the nucleus, and vanishes as $\vec{r} \rightarrow \infty$. There is also a clear advantage of using the electron density over the wave function approach since it reduces the many-body problem of N electrons with 3N spatial coordinates, to only three coordinates regardless of the number of electrons.

The groundwork for density functional theory was laid in the 1960s with two mathematical theorems proved by Kohn and Hohenberg:

> **Theorem 1**: The ground state energy from Schrödinger's equation is a unique functional of the electron density. (i.e. the ground state energy E from Schrödinger's equation can be expressed as $E[n(\vec{r})]$)

Although Theorem 1 proved that a functional exists it did not provide that functional. The second Theorem however goes on to prove an important property of that functional.

> **Theorem 2:** The electron density that minimizes the energy of the overall functional is the true electron density corresponding to the full solution of the Schrödinger equation.

In other words, if we can vary the electron density until the energy from the functional is at a minimum, that will be the correct ground-state electron density.

Kohn and Sham have shown how to approximate Ψ as a product of one-electron wave functions. The Kohn-Sham equations are shown below:

$$\left[-\frac{\hbar^2}{2m}\nabla^2 + V(\vec{r}) + V_H(\vec{r}) + V_{XC}(\vec{r})\right]\psi_i(\vec{r}) = \varepsilon_i\psi_i(\vec{r}) \qquad \text{(Equation 2.8)}$$

The solution of these equations are single electron wave functions, $\psi_i(\vec{r})$, that depend on 3 spatial coordinates. The three potentials, V, V_H and V_{XC} describe the interaction between the electron and all the nuclei, the repulsion between the electron and the total electron density (the Hartree potential) and the exchange and correlation contributions respectively.

$$V(\vec{r}) = -\sum_k^{nuclei} \frac{Z_k}{|\vec{r} - \vec{r}_k|} \qquad \text{(Equation 2.9)}$$

$$V_H(\vec{r}) = e^2 \int \frac{n(\vec{r}')}{|\vec{r} - \vec{r}'|} d\vec{r}' \qquad \text{(Equation 2.10)}$$

$$V_{XC}(\vec{r}) = \frac{\delta E_{XC}(\vec{r})}{\delta n(\vec{r})} \qquad \text{(Equation 2.11)}$$

As seen from Equations 2.10 and 2.11 above, both V_H and V_{XC} depend on the electron density, $n(\vec{r})$, but to find the electron density one requires the single electron wave functions, $\psi_i(\vec{r})$, but knowing these wave functions requires solving the Kohn-Sham equations which brings us back to where we started. Therefore, to break this cycle, the problem of solving the Kohn-Sham equations has to be done iteratively using the following steps:

1. Start with an initial guess for $n(\vec{r})$.
2. Solve the Kohn-Sham equations using the electron density, $n(\vec{r})$, to find the wave functions, $\psi_i(\vec{r})$.
3. Calculate the electron density, $n_{KS}(\vec{r})$, defined by the Kohn-Sham wave functions, $\psi_i(\vec{r})$ from the previous Step 2, $n_{KS}(\vec{r}) = 2\sum \psi_i^*(\vec{r})\psi_i(\vec{r})$.
4. Compare $n_{KS}(\vec{r})$ with $n(\vec{r})$. If they are the same, $n(\vec{r})$ is the ground state electron density that can be used to compute the total energy. If they differ, update the trial electron density, $n(\vec{r})$, and go back to Step 2.

These steps are then repeated until convergence is reached, leading to a solution to the Kohn-Sham equations.

To conclude this section on a historical note, in 1998 Kohn won the Nobel Prize[51] for "his development of the density functional theory" and now DFT is being used in material science, soil science, geochemistry, protein folding and many other fields, with hundreds of papers being published every year.

2.2 Computational Methods

2.2.1 Choice of Functional and Basis Set

In the previous section we have seen that to solve the Kohn-Sham equations the exchange-correlation energy, E_{XC}, is needed (Equation 2.11). However, E_{XC} is not known. It is defined to include all the quantum chemical effects that are not included in the other terms of the equation. One of the main goals of modern DFT is to find better

functionals that can approximate these two quantities (exchange and correlation) that best describe nature.

There is one case however, where this functional can be derived exactly - a uniform electron gas, where the electron density is constant at all points in space. *Local density approximation* (LDA) functionals use this idea to derive exchange-correlation energy functionals of the form shown in Equation 2.12 below,

$$E_{XC}^{LDA}\left[n(\vec{r})\right] = \int n(\vec{r})\varepsilon_{XC}\left[n(\vec{r})\right]d\vec{r} \qquad \text{(Equation 2.12)}$$

where ε_{XC} is the exchange-correlation energy per particle of a uniform electron gas of electron charge density $n(\vec{r})$.

While LDA might be a reasonable first approximation, it tends to overestimate the exchange-correlation energy.[52] Hence a gradient approach allows for corrections in electron density as it moves away from the source. The functionals that take this approach are called *generalized gradient approximation* (GGA) functionals.

Some of the first GGA exchange functionals were developed by Becke in 1988, abbreviated by "B", which provides corrections using the gradient of the density, as well as the correlation functional developed by Lee, Yang and Parr, abbreviated by "LYP", designed to compute the full correlation energy.[53,54] The Becke 3 Parameter hybrid functionals, use a mixture of Hatree-Fock (HF) exchange and DFT exchange-correlation, with constants for the exchange and correlation energies that were derived by Becke.[55] One of these hybrid functionals is the B3LYP functional, which also uses

the correlation provided by the LYP. The B3LYP is one of the most popular functionals used in DFT to date with an overall good performance which will also be demonstrated in this thesis, especially in comparison with experimental results from the field of environmental geochemistry.

Basis sets are functions that describe atomic orbitals and are used in linear combinations to create molecular orbitals. The basis set will restrict the electrons to a particular region of space. So the larger the basis set the fewer constraints on the electron, leading to a more accurate approximation of the real molecular orbitals or electron density. The basis set size can be increased by using double zeta (DZ) or triple zeta (TZ) basis sets, which would double or triple the number of basis functions. For example, in the case of the Carbon atom with 6 electrons in the 1s, 2s, $2p_x$, $2p_y$ and $2p_z$ orbitals, a minimum of 5 basis functions (single-zeta) are required to describe the atoms orbitals, so the DZ or the TZ basis set would use 10 or 15 basis functions respectively. Since valence electrons are more chemically important than core electrons, *split-valence* basis sets are more typical, with a single-zeta for the core orbitals and double or triple-zeta for valence orbitals.

To further increase the size of the basis set (and hence the precision of the calculation) polarization functions and diffuse basis functions can also be used. Polarization functions add flexibility to the orbitals that better represent electron density in bonding regions, while diffuse functions increase the electronic radius where the electrons can be found. Diffuse functions are particularly important for calculations with

anionic molecules and weaker van der Waals interactions. In Pople notation the basis set 6-311+G(d,p) conveys that it is a split-valence triple zeta basis set with 6 d-type basis functions added for heavy atoms, 3 p-type basis functions for H atoms and the "+" stating that diffuse orbitals are added for heavy atoms. The first number "6" indicates the number of Gaussians used to construct each core atomic orbital basis function and the numbers "311" following the hyphen convey that the valence orbitals are composed of three basis functions each, with the first basis function composed of 3 Gaussians and the second and third composed of 1 Gaussian.

2.2.2 Choice of Solvation Model

To properly mimic a hydrated environment, several explicit water molecules are added in the calculations. This approach however has its limitations, since every extra molecule of water added also adds many more degrees of freedom and makes calculations computationally expensive. Thus, the use of a solvation model that treats the solvent as a continuous medium encompassing the solute seems desirable. However, continuum models have their drawbacks as well and particularly problematic are the regions close to the solute, where properties are different from the bulk. With this thought in mind a middle ground is established, where just enough explicit water molecules are added around the area of interest to fill the first solvation shell and an implicit continuum solvation model is used to deal with long range solvation phenomena.

Polarized continuum models (PCM)[56] use a solute cavity, a union of overlapping spheres around the atoms of the solute molecule, where the radii of these spheres are empirically determined. The solute cavity is then surrounded by a continuous dielectric medium to mimic solvation effects. This is shown in Figure 2.1 below where the DMA molecule with its surrounding explicit waters are used to form the cavity (white region), while the surrounding blue region represents the continuum dielectric medium in which the solute is placed. The dielectric medium in our case is water. The solvation model used in this thesis is the integral equation formalism of the PCM and is henceforth referred to as the IEFPCM solvation model.

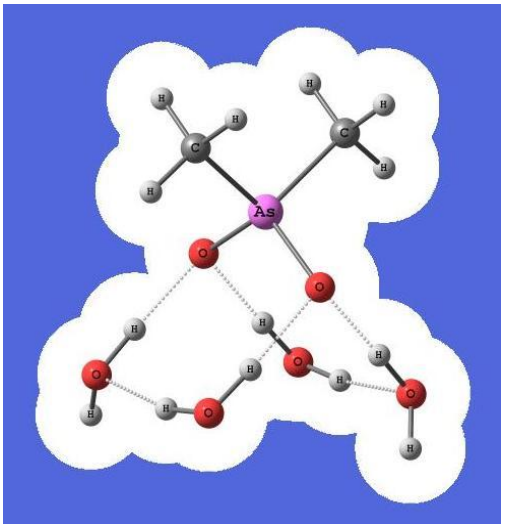

Figure 2.1 A cavity built from overlapping spheres around DMA and 4 explicit waters in a continuum solvent (blue).

2.2.3 Choice of Dispersion Model

On top of accounting for solvation effects, it is also important to account for the long range attractive van der Waals interactions by adding a dispersion model. DFT

calculations that account for dispersion effects are known to improve chemical accuracy[57] affecting both inter-atomic distances[58] and hydrogen bond lengths.[59] Therefore, calculations were performed using the D3 version of Grimme's dispersion and using Becke-Johnson (BJ) damping. This version of the dispersion model (from now on referred to as the GD3BJ) has been shown to be on average an improvement over the simpler GD3 model for 12 density functionals, including the B3LYP functional.[60]

2.2.4 Choice of modelling the Iron Oxyhydroxide Surface

Two model Fe(III) surfaces are considered in this thesis for arsenicals adsorption: The 2Fe surface and the extended 4Fe surface (Figure 2.2), each with their own advantages and disadvantages. While the 2 Fe surface is less computationally expensive to model, it has been shown to produce complexes that are "over-relaxed" when interacting with the adsorbent. This idea will be explained further in the thesis.

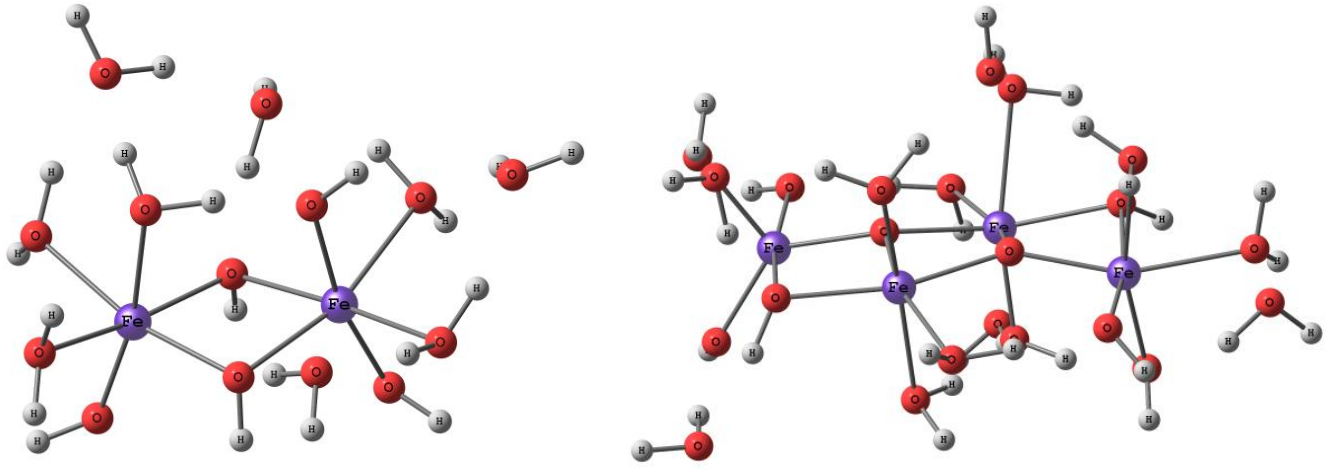

Figure 2.2 The modelled iron oxyhydroxide surfaces considered for simulating adsorption of Organoarsenicals with (A) containing 2 Fe centres and (B) 4 Fe centres.

Calculations that involve Fe(III) surfaces were performed at high spin. The electron configuration of Fe^{3+} is $1s^2 2s^2 2p^6 3s^2 3p^6 3d^5$, with each electron in the 3d orbitals being unpaired and occupying only one of the *five* d-orbitals. Since the multiplicity is calculated as N+1, where N is the number of unpaired electrons and there are 5 unpaired electrons for every Fe^{3+} atom, the multiplicity of a cluster that has M number of Fe^{3+} atoms becomes 5M+1. Hence clusters that contained two Fe^{3+} atoms, were calculated with a multiplicity of 11 (i.e. 5x2 = 10 unpaired electrons) and clusters with four Fe^{3+} atoms, were calculated with a multiplicity of 21 (i.e. 5x4 = 20 unpaired electrons).

It was also observed that having less than three OH_2 ligands on the Fe^{3+} atoms of the modelled iron oxyhydroxide cluster produces a change in the coordination geometry, going from an octahedral to trigonal bipyramidal geometry because one of the H_2O molecules escapes. This change has been observed in other computational studies with high spin Fe^{3+} atoms in "dehydrated" environments.[61] For all Fe^{3+} complexes with 3 OH_2 ligands or more, the octahedral coordination geometry was found to be stable.

In all cases, the charge of the iron oxyhydroxide surfaces is kept at +1 because the point of zero charge (pzc) for iron oxides is in the 7-9 pH range.[62] Keeping the same charge for the smaller and extended surface also allows for an analysis of how a +1 charge distributed over two and four Fe centers affects adsorption.

2.2.5 Energy Optimization and Frequency Calculations

Calculations are set up with an initial geometry for a molecule or cluster of interest, which after multiple iterations will relax to find a geometry that is at an energy minimum on the potential energy surface (PES). This type of calculation is called an *energy minimization* or *geometry optimization* calculation. The calculated energy is the Electronic Energy (E_0), which is a negative value given in atomic units (a.u.) and represents the energy relative to the separate electrons and nuclei.

Building the initial chemical structure to use as a starting geometry in an energy optimization calculation takes a bit of practice and chemical intuition. A PES minimum does not always guarantee that the model is at a global minimum. It might just be a local minimum or a saddle point along the PES. Therefore, clusters were generally built gradually by first optimizing only the surface (i.e. the adsorbent), then adding the molecule that will interact with the surface (i.e. the adsorbate) and then adding the explicit water molecules that surround that cluster, one or two waters at a time while performing an energy optimization each time.

Calculations of vibrational frequencies for the modelled geometries are computed by determining the second derivatives of the energy with respect to the atomic coordinates (i.e. d^2E/dr^2). Hence frequency calculations can only be computed after a geometry optimization where a stationary point was reached and at the same level of theory. Calculating frequencies at 6-311+G(d,p) for a 6-31G(d) optimized geometry would produce meaningless results. Furthermore, if the calculated vibrational

frequencies are *real* (i.e. all positive), then the modelled geometry is at a PES minimum. If however, one vibrational frequency is imaginary (negative), then the modelled geometry is a transition state (i.e. a saddle point on the PES). If the modelled geometry has more than one imaginary frequency, then the geometry is unstable and a new input geometry is needed.

Calculating vibrational frequencies also allows the calculation of thermodynamic properties, like the Enthalpy, Gibbs free energy or the Entropy for any given reactions in the following way:

$$\Delta H^{\circ}_{ads} = \sum (E_0 + H_{corr})_{products} - \sum (E_0 + H_{corr})_{reactants} \qquad \text{(Equation 2.13)}$$

$$\Delta G^{\circ}_{ads} = \sum (E_0 + G_{corr})_{products} - \sum (E_0 + G_{corr})_{reactants} \qquad \text{(Equation 2.14)}$$

$$\Delta S^{\circ}_{ads} = \left(\Delta H^{\circ}_{ads} - \Delta G^{\circ}_{ads} \right) / T \qquad \text{(Equation 2.15)}$$

where H_{corr} and G_{corr} are the thermal corrections to enthalpy and thermal corrections to Gibbs free energy respectively. The superscript (^{o}) is added to Equations 2.13, 2.14 and 2.15 to indicate that calculations were performed at standard temperature (298.15 degrees Kelvin) and pressure (1 atmosphere).

2.2.6 Transition State Calculations

Transition states for adsorption reactions can inform us about binding mechanisms and activation barriers, but finding them is not an easy task. To find

transitions states for organo-arsenical complexes transitioning from outer-sphere to monodentate to bidentate, a stepwise optimization approach was taken where several restricted distance optimizations were performed along an idealized reaction pathway. Starting with the optimized outer-sphere complex, the inter-atomic distance between the AsO moiety and the central Fe atom of the modelled surface, d(AsO-Fe), was reduced by 0.1 Ångströms (Å) each step. A restricted optimization was performed at each step where the d(AsO-Fe) was held fixed while the rest of the complex was allowed to relax. The electronic energy along the a reaction pathway will change, as seen in Figure 2.3 below, where the minima are the geometries for the outer-sphere and monodentate complexes.

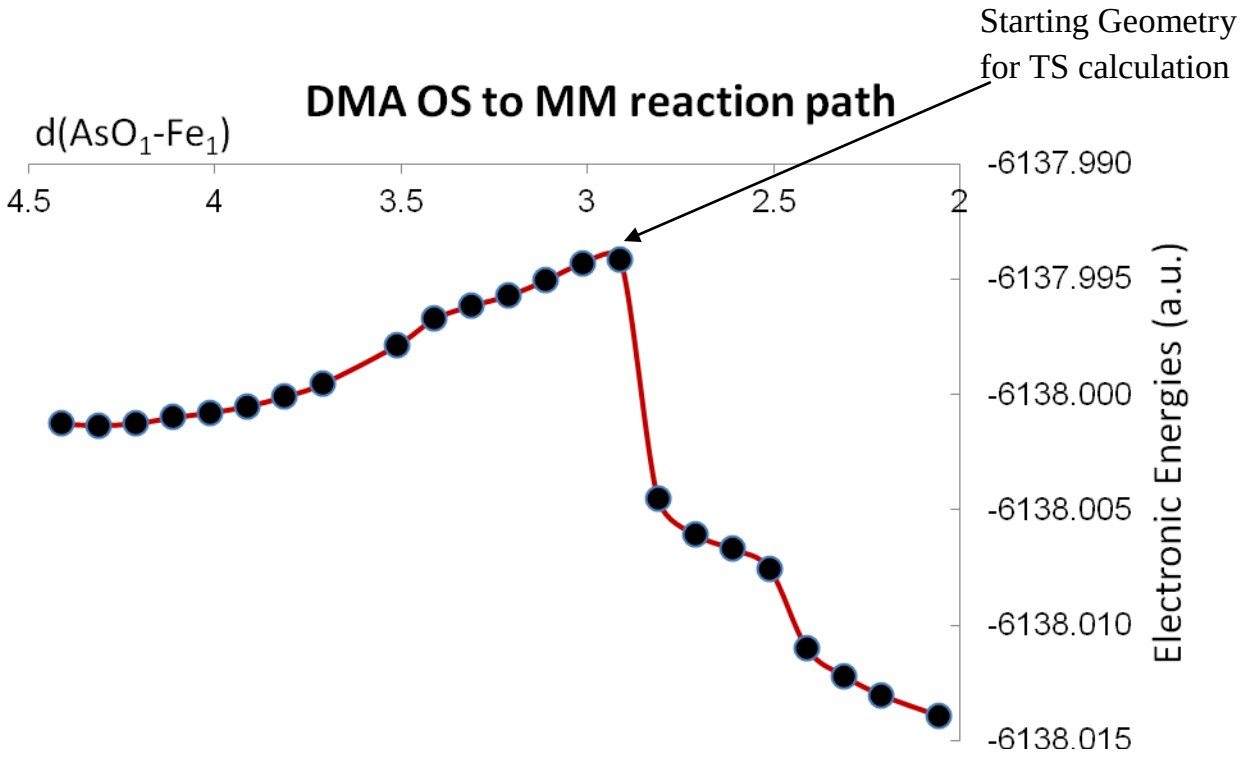

Figure 2.3 A step by step restricted optimization along a reaction pathway where the AsO-Fe distance is reduced by 0.1 Å each step.

The same technique is repeated to find the transition states between the monodentate and bidentate geometries. The point of maximum energy along the reaction pathway will then become the starting geometry for the transition state calculation.

Optimization for transition states in this thesis used the Berny algorithm[63] that is available in Gaussian when using the OPT=TS. Transition states were checked to have only one imaginary frequency that showed the transition from the reactant to the product when animated. Intrinsic reaction coordinate (IRC) calculations[64] were also conducted for some transition states as seen in Appendix C, to confirm that the transition state connects reactant to product.

2.3 Calculations Summary

Unless otherwise specified, the data presented in this thesis is from calculations performed using Gaussian 09, running on SHARCNET[65], at the B3LYP/6-311+G(d,p) level of theory, with the IEFPCM solvation model and GD3BJ dispersion corrections at 298.15 degrees Kelvin and 1 atmospheric pressure. The calculated geometries and frequencies were visualized using ChemCraft, Version.1.6 (build 315).

CHAPTER III. The Sorption of p-Arsanilic Acid onto Hydrated Iron (III) Oxyhydroxide Clusters

3.1 Overview

Aromatic organoarsenicals are still used as feed additives in the poultry industries in developing countries and the contaminated litter is used as fertilizer. These compounds enter the environment to interact with reactive soil components such as iron oxides. Little is known about these interactions at a molecular level. Density functional theory calculations for hydrated pAsA/iron oxide complexes can provide insight into complex formation, energies of reaction and vibrational frequencies. Gibbs free energies and enthalpies of adsorption for various types of ligand exchange reactions leading to inner- and outer-sphere complexes are calculated and compared to the well known arsenate system. Calculations show that the formation of inner- and outer-sphere pAsA/iron oxide complexes all thermodynamically favourable, but that the formation of monodentate complexes is most favourable. Interatomic As–Fe distances are calculated with and without dispersion corrections. It is shown that dispersion corrections can bring the arsenical closer to the iron oxyhydroxide surface by 0.1 – 0.2 Å for monodentate and outer-sphere complexes, but have little effect on bidentate complexes. In addition, transition state calculations show an activation barrier around +23kJ/mol in the formation of the bidentate complex from the monodentate complex. Desorption thermodynamics in the presence of phosphate and oxalic acid show that reactions are more favourable using oxalic acid as the desorbing agent.

3.2 Introduction

Aromatic organoarsenicals including p-arsanilic acid (4-aminophenyl arsonic acid, pAsA) and roxarsone (4-hydroxy- 3-nitrobenzenearsenic acid, ROX) are still used today as feed additives in developing countries such as China with intense poultry operations.[66] These organoarsenicals are added to poultry feed to control disease, stimulate growth, and improve both feed efficiency and feed conversion[67], but their negative effects have led to bans in Europe[68] and a voluntary suspension of them in North America.[69,70,71] These organoarsenicals are not metabolized in the poultry and are excreted chemically unchanged, while the manure is turned into pellets for use as fertilizers and sold commercially.[72] Once applied to soil, microbial activity and ultraviolet light[73,74,75] may also lead to the formation of other organic arsenic species, like DMA, as well as inorganic arsenic species.[76,77]

In this chapter the optimized geometries of pAsA in the bulk, as well as pAsA bound to iron oxyhydroxide clusters in a hydrated environment to mimic the solid/water interface are evaluated. We also investigate the reaction pathways going toward bidentate complexation, find transition state structures, analyze theoretical infrared spectra in comparison with experimental work and calculate Gibbs free energies, enthalpies and entropies of adsorption for various types of ligand exchange reactions leading to both inner- and outer-sphere complexes.

3.3 Results and Discussion

3.3.1 Hydration and the pAsA aromatic ring

The optimized geometries of the various pAsA species in the bulk with different number of explicit water molecules are shown in Figure 3.1 below. The optimized pAsA structures shown in Figure 3.1 have one negative charge. Since pAsA has pK_a values (see Table 1) at 4.1 (pK_{a2}) and 9.2 (pK_{a3}) the negatively charged species would be the dominant species in most environmental conditions and is the one species considered in this study.

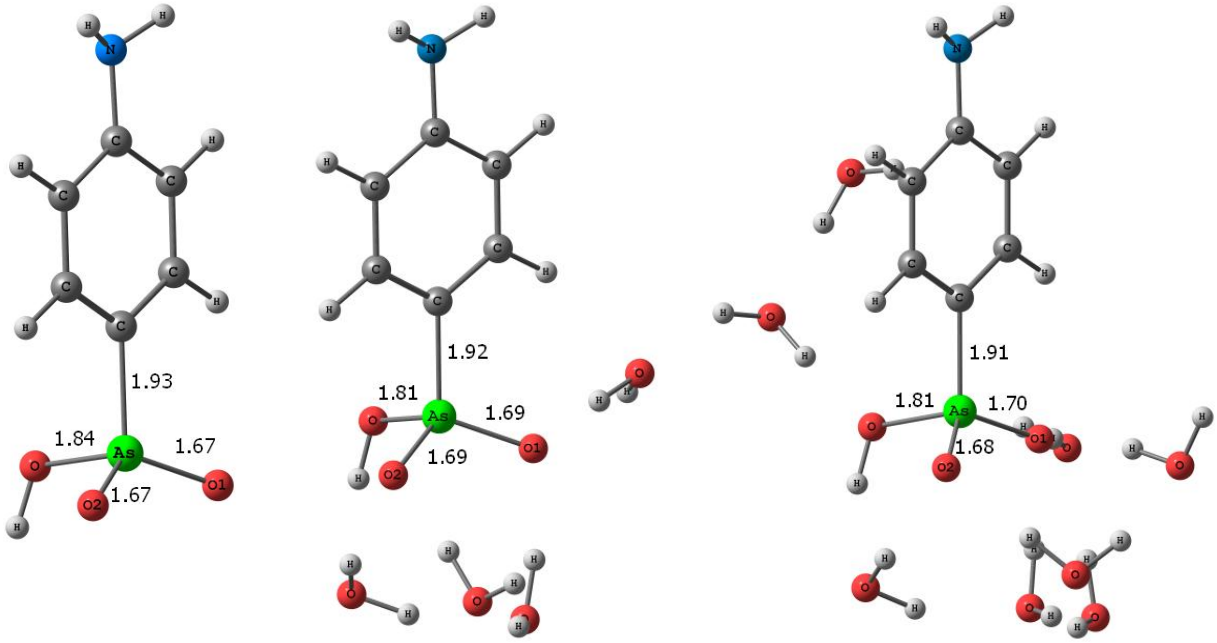

$pAsA^-$ $pAsA^- \cdot (H_2O)_4$ $pAsA^- \cdot (H_2O)_8$

Figure 3.1 Optimized structures of $pAsA^-$ surrounded by 0, 4 and 8 explicit waters. Bond lengths shown in Ångströms. Calculated using B3LYP/6-311+G(d,p) and the IEFPCM solvation model.

The calculated As-O bond distances, d(As-O), for the $pAsA^{-1}$ with different explicit waters range from 1.67-1.70 Å, for d(As-OH) they range from 1.81-1.84 Å and

for d(As-C) they range between 1.91-1.93 Å. The most significant difference is observed when going from 0 to 4 explicit water molecules. When going from 4 to 8 explicit waters some H_2O molecules migrate to the second solvation shell and the effect on the bond distances is not as significant. Further details on the changes in the geometry of $pAsA^-$ as more explicit waters are added (going from 0 to 4 to 8 explicit waters) are shown in Table 2. Table 2 also shows that using a different functional, like the M06-2X, with the same basis set and solvation model, has no significant effect on the geometry of pAsA either. Hence, for the purposes of this study and speed of computation, four explicit water molecules with the IEFPCM solvation model will be considered in most calculations.

Table 3.1 Calculated As-O and As-C bond distances (Å) for $pAsA^-$ clusters with various explicit water molecules. The structures with 0, 4 and 8 explicit waters are illustrated in Figure 3.1.

Geometries	**As-O_1**	**As-O_2**	**As-OH**	**As-C**
$pAsA^-$	1.67	1.67	1.84	1.93
$pAsA^- \cdot (H_2O)_4$	1.69	1.69	1.81	1.92
* $pAsA^- \cdot (H_2O)_4$	1.68	1.67	1.79	1.90
$pAsA^- \cdot (H_2O)_8$	1.68	1.69	1.81	1.91

*calculated with M06-2X/6-311+G(d,p) for comparison

The effects of rotating the aromatic ring of $pAsA^-$ on the electronic energy were also explored. The aromatic ring rotation was performed at four levels of solvation using constraint energy minimization calculations for $pAsA^-$ in the gas phase, with the IEFPCM solvation model, with IEFPCM and both 4 explicit waters and IEFPCM with 8 explicit waters. The C−C−As−O dihedral angle was rotated every 10° from −180 to

180° while the remaining bonds and angles were allowed to relax and the energies of the pAsA structures were tabulated at each point. Figure 3.2 shows the relative energy of the pAsA molecule as a function of the dihedral angle. It is observed that the relative energy minimum, for all four levels of solvation, is at a dihedral angle of around 20°. This minimum also corresponds with the position of the −OH group being roughly perpendicular to the aromatic ring (Figure 3.3). The energy maxima differ more when no explicit waters are present (red and brown lines) but peak at around d(C−C−As−O) ~ −77° and 103° with 4 and 8 explicit waters (green and purple lines). This minimum also corresponds with the position of the OH group on $pAsA^-$ being parallel to the aromatic ring. A reason for the lower energy might be that there is hyperconjugation occurring when the As–O σ bond is lined up with the π bonds of the aromatic ring. Hyperconjugation is known to stabilize molecules and affect the length of the sigma bonds with carbon leading to shorter bond distances.[78]

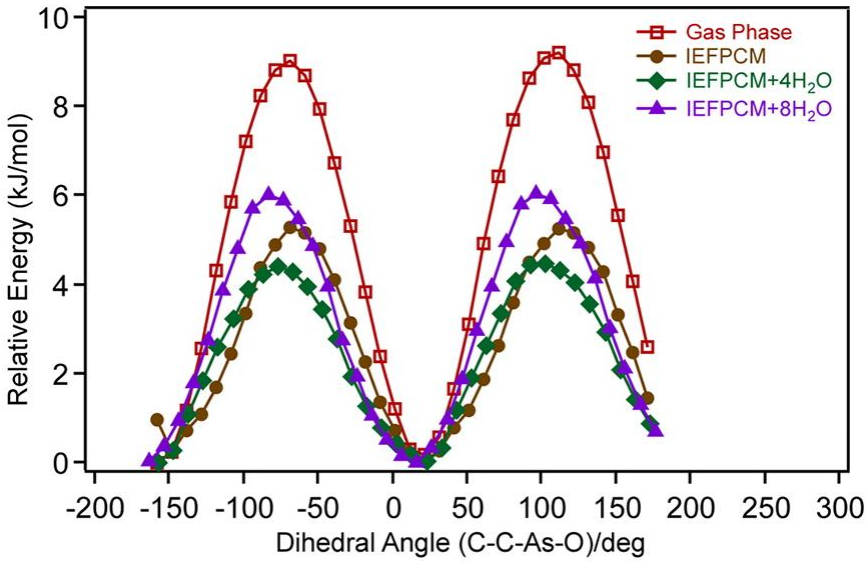

Figure 3.2 Relative energy of $pAsA^-$ as a function of dihedral angle (C–C–As–O). Dihedral angle restricted calculations in the gas phase and at various levels of solvation using B3LYP/6-311+G(d,p) level of theory.

Figure 3.3 shows the variation in the d(As–C) with respect to the changing d(C−C−As−O) that confirms this idea. Figure 3.3 also illustrates how adding explicit water molecules decreases the As–C bond length and the experimentally determined d(As-C) = 1.907 Åvalue reported for the crystalline structure of pAsA is approached.[79]

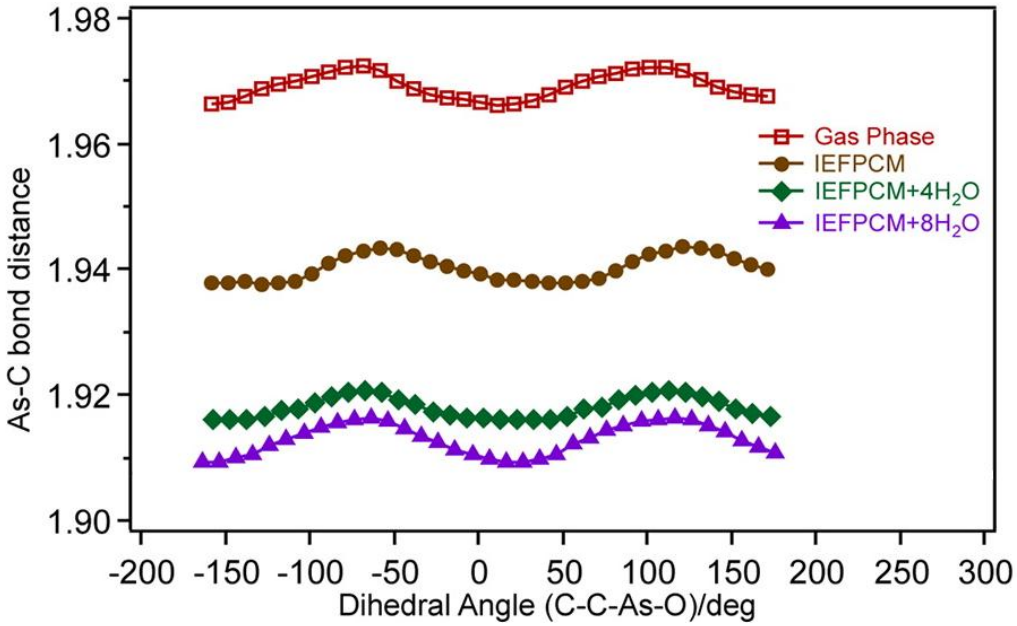

Figure 3.3 As–C bond lengths in the gas phase and at various levels of hydration. The energy is at a minimum when d(C–C–As–O) ~ 20°.

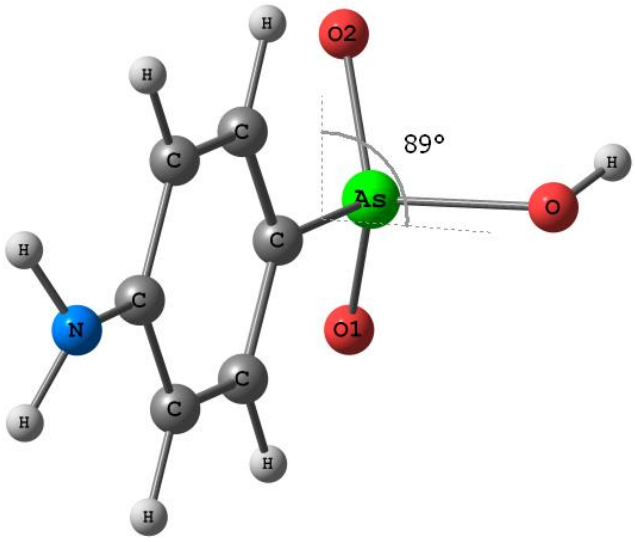

Figure 3.4 The energy minimum corresponds to the position of the OH group being roughly perpendicular (90°) to the aromatic ring.

3.3.2 Complexation of pAsA with iron (III) oxyhydroxide clusters

The adsorption of pAsA onto iron oxyhydroxides can produce different types of complexes via ligand exchange. Figure 3.5 shows optimized geometries of hydrated pAsA-iron oxyhydroxide clusters in the outer-sphere (OS), monodentate mononuclear (MM) and bidentate binuclear (BB) configurations and Table 3.2 shows the structural parameters of these pAsA complexes. The OS complex is adsorbed through hydrogen bonds with inter-atomic d(As-Fe) of 5.21 and 5.58 Å with the two iron centers Fe1 and Fe2 respectively. The inner-sphere MM and BB complexes are formed after ligand exchange and formation of covalent bonds with the Fe atoms in the iron oxyhydroxide surface. The interatomic As–Fe distances for the MM complex are 5.21 and 5.58 Å, while for the BB complex they are 3.29 and 3.43 Å.

Table 3.2 Predicted As-O, Fe-O bond distances (Å) and As-Fe inter-atomic distances (Å) of OS, MM, BB and TS complexes of pAsA with iron oxyhydroxides. Calculated with B3LYP/6-311+G(d,p) and IEFPCM.

OS, MM and BB pAsA complexes	As-Fe_1	As-Fe_2	As-O_1	As-O_2	As-C	As-OH	Fe_1-O_1	Fe_2-O_2
OS pAsA · $(H_2O)_4$ $Fe_2(OH)_4(OH_2)_4$	5.21	5.58	1.68	1.69	1.91	1.80	-	-
MM pAsA-$Fe_2(OH)_5(OH_2)_3$ ·$(H_2O)_5$	4.92	3.54	1.66	1.70	1.90	1.82	-	2.06
***MM** pAsA-$Fe_2(OH)_5(OH_2)_3$ ·$(H_2O)_5$	4.66	3.48	1.65	1.69	1.88	1.79	-	2.03
TS pAsA-$Fe_2(OH)_5(OH_2)_3$ ·$(H_2O)_5$	3.98	3.35	1.66	1.71	1.91	1.81	-	2.08
BB pAsA-$Fe_2(OH)_5(OH_2)_3$ ·$(H_2O)_5$	3.43	3.29	1.68	1.69	1.90	1.80	2.19	2.11

*calculated with M06-2X/6-311+G(d,p) for comparison with the B3LYP/6-311+G(d,p)

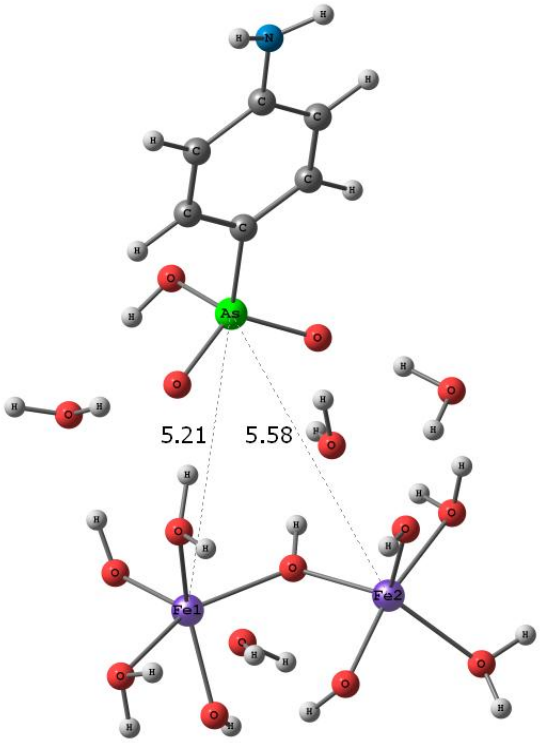

OS pAsA Complex

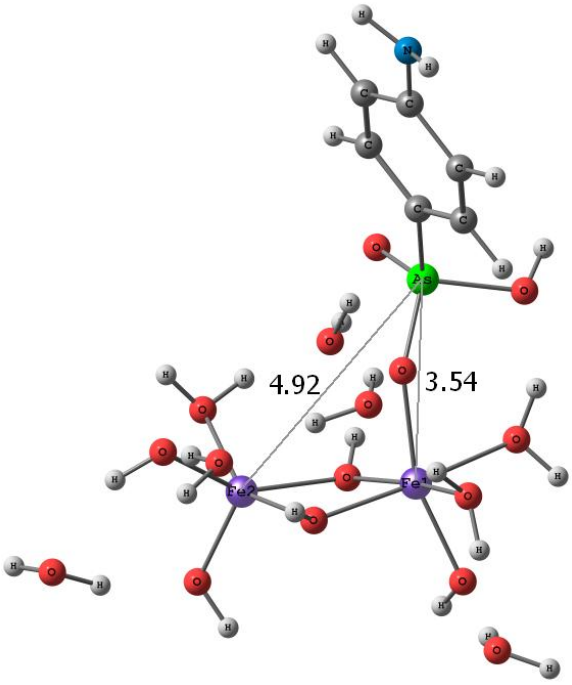

MM pAsA Complex

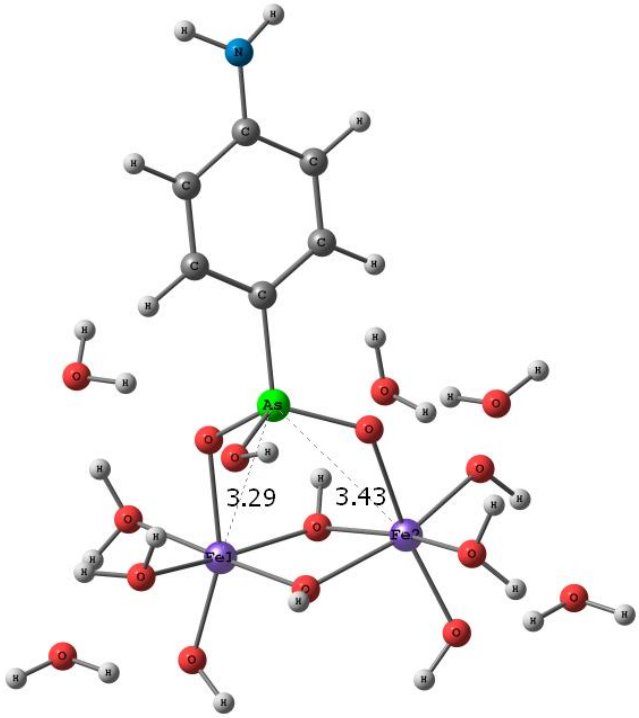

BB pAsA Complex

Figure 3.5 Energy minimized structures of pAsA complexes. Calculated using B3LYP/6-311+G(d,p) and IEFPCM.

The d(As-O) for the OS complex are 1.68 and 1.69 Å, and the As–OH bond is 1.80 Å. Similarly, the d(As=O) for complex B (MM) is 1.66 Å, showing more of a double bond character while As–OH is 1.82 Å, while the d(As-OFe) bond is 1.70 Å. For the BB complex, the d(As–OFe) bonds are 1.68 and 1.69 Å and the As–OH bond is 1.80 Å. Moreover, Table 3.2 also shows the geometry of the energy minimized MM arsenate using the M06-2X functional marked with a star (*). The biggest variation in the MM complexes calculated with the two functionals is the inter-atomic As-Fe_1 distance that differs by 0.26 Å (or ~ 5.3%). The transition state of pAsA transitioning from the MM to the BB complex was also calculated as described in Chapter 2, and is shown in Figure 3.6.

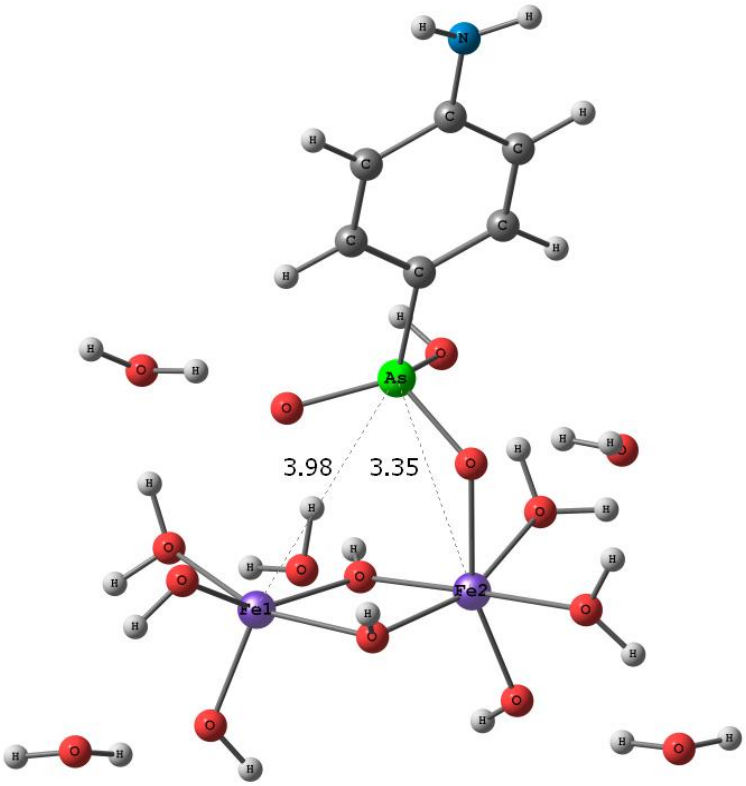

Figure 3.6 Transition state structure of pAsA going toward BB from the MM complex. Calculated at B3LYP/6-311+G(d,p) and IEFPCM solvation model.

The d(As-O) for the TS complex is very similar to the MM complex at 1.66 and 1.71 Å and the d(As–OH) is 1.81 Å. The inter-atomic distance d(As-Fe) is as expected, almost midway between the MM and BB complexes at 3.98 and 3.35 Å from the iron centers Fe1 and Fe2 respectively.

3.3.3 Adsorption Thermodynamics

Calculating the enthalpies (ΔH_{ads}) and Gibbs free energies (ΔG_{ads}) of adsorption for various hypothetical reactions can reveal the types of complexes that are most thermodynamically favourable. In a neutral environment the $pAsA^-$ species (dominant in the pH range 4.1 - 9.2) reacts with the positively charged iron oxyhydroxide surface (e.g. goethite, hematite). Reactions would occur via ligand exchange to form either the neutral outer-sphere or an inner-sphere complex as shown in Figure 3.5 and listed in Table 3.2 The ΔH_{ads}, ΔG_{ads} and ΔS_{ads} values are calculated as shown in Equations 2.13, 2.14 and 2.15 respectively in Chapter 2. Hence the thermal corrections to enthalpy, H_{corr}, thermal corrections to Gibbs free energy, G_{corr}, and their sums to the electronic energies are needed in order to calculate ΔH_{ads}, ΔG_{ads} and ΔS_{ads}. These values are shown in Table 3.3 below.

Table 3.3 Electronic energies (E_0), thermal corrections to enthalpy (H_{corr}), thermal corrections to Gibbs free energy (G_{corr}) and their sums ($E_0 + H_{corr}$) and ($E_0 + G_{corr}$) in atomic units. Optimized using B3LYP/6-311+G(d,p) and IEFPCM solvation.

Reactants	**Energy (E_0)**	**H_{corr}**	**G_{corr}**	**$E_0 + H_{corr}$**	**$E_0 + G_{corr}$**
$pAsA^- \cdot (H_2O)_4$	-3055.39301	0.24932	0.17325	-3055.14369	-3055.21976
* $pAsA^- \cdot (H_2O)_4$	-3055.03462	0.25314	0.17961	-3054.78148	-3054.85501
$Fe_2(OH)_5(OH_2)_5^+ \cdot (H_2O)_4$	-3595.01158	0.32945	0.22837	-3594.68212	-3594.78321
* $Fe_2(OH)_5(OH_2)_5^+ \cdot (H_2O)_4$	-3594.48640	0.33362	0.23799	-3594.15278	-3594.24842
pAsA complexes	**Energy (E_0)**	**H_{corr}**	**G_{corr}**	**$E_0 + H_{corr}$**	**$E_0 + G_{corr}$**
OS $pAsA \cdot (H_2O)_4\ Fe_2(OH)_4(OH_2)_4$	-6268.05485	0.44342	0.32345	-6267.61143	-6267.73140
MM $pAsA\text{-}Fe_2(OH)_5(OH_2)_3 \cdot (H_2O)_5$	-6268.06994	0.44252	0.31756	-6267.62742	-6267.75239
***MM** $pAsA\text{-}Fe_2(OH)_5(OH_2)_3 \cdot (H_2O)_5$	-6267.35964	0.44821	0.32804	-6266.91144	-6267.03161
BB $pAsA\text{-}Fe_2(OH)_5(OH_2)_3 \cdot (H_2O)_5$	-6268.05858	0.44182	0.31360	-6267.61676	-6267.74499
Transition State	**Energy (E_0)**	**H_{corr}**	**G_{corr}**	**$E_0 + H_{corr}$**	**$E_0 + G_{corr}$**
TS $pAsA\text{-}Fe_2(OH)_5(OH_2)_3 \cdot (H_2O)_5$	-6268.05472	0.44036	0.31126	-6267.61435	-6267.74346
Leaving water groups	**Energy (E_0)**	**H_{corr}**	**G_{corr}**	**$E_0 + H_{corr}$**	**$E_0 + G_{corr}$**
H_2O	-76.46641	0.02497	0.00354	-76.441439	-76.462869
$(H_2O)_2$	-152.93967	0.05253	0.01958	-152.88715	-152.90155
$(H_2O)_3$	-229.41401	0.08012	0.03813	-229.33390	-229.37589
$(H_2O)_5$	-382.37265	0.13567	0.08274	-382.23698	-382.28990
* $(H_2O)_5$	-382.18935	0.13715	0.08455	-382.05220	-382.10481

*calculated with M06-2X/6-311+G(d,p) for comparison with the B3LYP/6-311+G(d,p)

Table 3.4 shows the calculated ΔH_{ads}, ΔG_{ads}, and ΔS_{ads} values for various adsorption reactions of pAsA onto iron oxyhydroxides using the electronic energies with the thermal corrections listed in Table 3.3. Reactions 1 - 4 in Table 3.4 show the formation of OS, MM and BB complexes and their ΔH_{ads}, ΔG_{ads}, and ΔS_{ads}. The pAsA reactions 1−4 in Table 3.4 are all thermodynamically favourable with a negative ΔG_{ads}, with Reaction 2 that leads to the formation of MM pAsA being the most favourable, followed by BB (Reaction 4) and then OS (Reaction 1). Reaction 3 in Table 3.4 was

calculated using a different functional (M06-2X) for comparison with results using the B3LYP functional. Calculations with both methods predict exothermic and exergonic reactions for the formation of MM pAsA complexes, but differ by about 20% in their values. These calculations are in agreement with current experimental findings using ATR-FTIR showing that the majority of pAsA adsorbs on hematite in a monodentate fashion.[80]

Table 3.4 Calculated ΔH_{ads}, ΔG_{ads} (kJ/mol) and ΔS_{ads} (kJ/mol K) for hypothetical adsorption reactions of pAsA and iron oxyhydroxide. Reactions energies used from Table 3.3 and converted to kJ/mol (where 1 a.u. = 2625.5 kJ/mol)

pAsA adsorption reactions	$\Delta \mathbf{H}_{ads}$	$\Delta \mathbf{G}_{ads}$	$\Delta \mathbf{S}_{ads}$
$[HO_3AsC_6H_4NH_2]^- \cdot (H_2O)_4 + [Fe_2(OH)_5(OH_2)_5]^+ \cdot (H_2O)_4 \rightarrow$			
1. **OS** pAsA $\cdot (H_2O)_4$ $Fe_2(OH)_5(OH_2)_4 + (H_2O)_5$	-59.3	-48.1	-0.0374
2. **MM** pAsA-$Fe_2(OH)_5(OH_2)_3 \cdot (H_2O)_5 + (H_2O)_5$	-101	-103	0.00646
3. *** MM** pAsA-$Fe_2(OH)_5(OH_2)_3 \cdot (H_2O)_5 + (H_2O)_5$	-77.1	-86.6	0.0318
4. **BB** pAsA-$Fe_2(OH)_5(OH_2)_3 \cdot (H_2O)_5 + (H_2O)_5$	-73.3	-83.8	0.0352
Reaction with different leaving groups	$\Delta \mathbf{H}_{ads}$	$\Delta \mathbf{G}_{ads}$	$\Delta \mathbf{S}_{ads}$
5. **OS** pAsA $\cdot (H_2O)_4$ $Fe_2(OH)_5(OH_2)_4 + 5(H_2O)$	+18.9	-112	0.440
6. **OS** pAsA $\cdot (H_2O)_4$ $Fe_2(OH)_5(OH_2)_4 + (H_2O)_2 + (H_2O)_3$	-17.5	-15.4	-0.00704
7. **MM** pAsA-$Fe_2(OH)_5(OH_2)_3 \cdot (H_2O)_5 + 5(H_2O)$	-23.1	-167	0.484
8. **MM** pAsA-$Fe_2(OH)_5(OH_2)_3 \cdot (H_2O)_5 + (H_2O)_2 + (H_2O)_3$	-59.5	-70.5	0.0370
9. **BB** pAsA-$Fe_2(OH)_5(OH_2)_3 \cdot (H_2O)_5 + 5(H_2O)$	+4.87	-148	0.513
10. **BB** pAsA-$Fe_2(OH)_5(OH_2)_3 \cdot (H_2O)_5 + (H_2O)_2 + (H_2O)_3$	-31.5	-51.1	0.0657
Transition State reaction	$\Delta \mathbf{H}_{ads}$	$\Delta \mathbf{G}_{ads}$	$\Delta \mathbf{S}_{ads}$
11. **TS** pAsA-$Fe_2(OH)_5(OH_2)_3 \cdot (H_2O)_5 + (H_2O)_5$	-67.0	-79.8	0.0429

*calculated with M06-2X/6-311+G(d,p) for comparison with the B3LYP/6-311+G(d,p)

Reactions 5-10 in Table 3.4 show the same reactions but with different leaving water groups leading to the OS, MM and BB pAsA complexes. The minimum energy water clusters used in these reactions are shown in Appendix A. It is necessary to show

that the type of water leaving group affects the sign and values of these state functions. Take for example, Reactions 4, 9 and 10 that form the BB complex and where the only difference is the way the water leaving groups are represented. In reaction 4 the waters leaving groups are treated as a five-water cluster, while in reaction 9 they are treated individually and multiplied by five. While reaction 9 yielded a more exergonic value for ΔG_{ads} (-148 kJ/mol) than reaction 4 (-83.8 kJ/mol), it did so with a big increase in the entropy, ΔS_{ads}. Reaction 10 considers the same reaction but with a two-water cluster and three-water cluster as leaving groups. This reaction is also exergonic (-51.1 kJ/mol) with a lower ΔS_{ads} but not as low as Reaction 4. Throughout this thesis, the decision is made to use the water molecules leave as a cluster in order to minimize the entropy and to more accurately depict bulk water interactions.

Figure 3.7 shows the relative energy values for the OS and BB complexes as well as the transition state TS relative to the lowest energy MM complex (i.e. $\Delta\Delta G_{ads}$). From Figure 3.7 we see that the activation barrier for the formation of the BB pAsA complex from the MM pAsA complex is +23.4 kJ/mol. For comparison this is ten times higher than the thermal energy at room temperature ($0.008315\ kJ\cdot K^{-1}\cdot mol^{-1} \times 298\ K = 2.48$ kJ/mol).

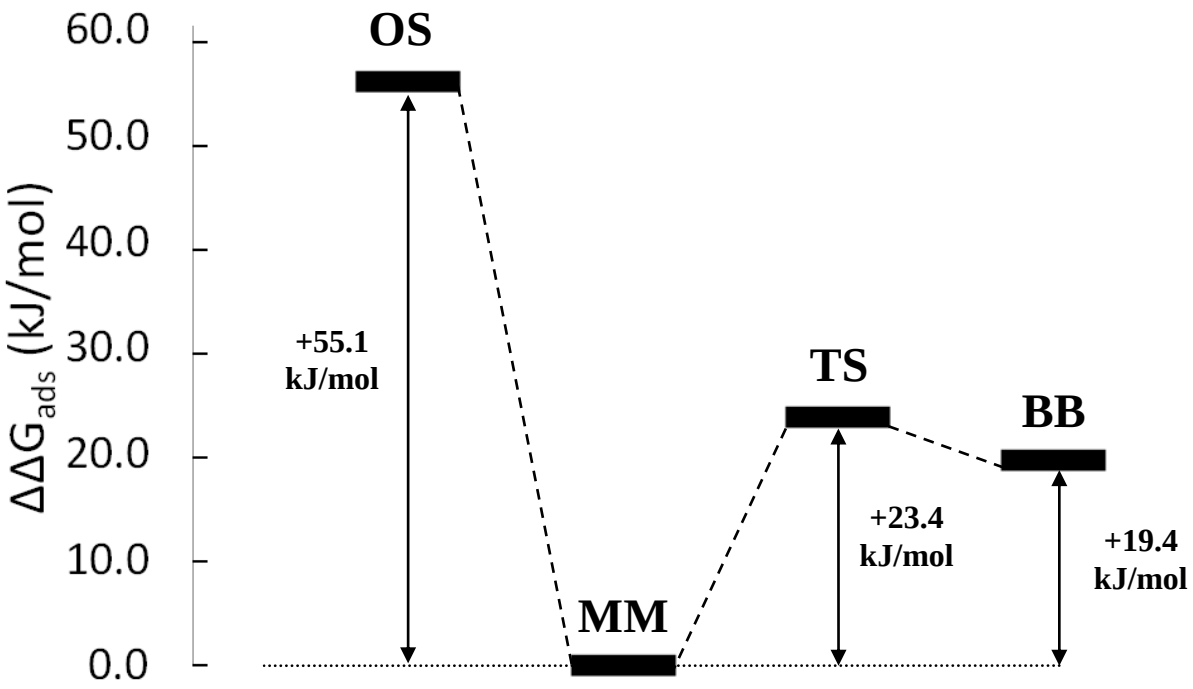

Figure 3.7 Energies for the OS, BB and TS pAsA complexes relative to the lowest energy MM complex shown in kJ/mol.

A similar activation barrier was found for transition state in the formation of the BB arsenate complex from the MM arsenate complex, at +26 kJ/mol. The arsenate data is shown in Appendix B. The difference between the arsenate and pAsA activation barriers is not significant enough to explain why arsenate preferentially forms bidentate complexes while pAsA preferentially forms monodentate complexes, thus suggesting the formation of mostly MM complexes for pAsA and mostly BB complexes for arsenate is thermodynamically driven and not kinetically driven.

Recent DFT studies[81] showing the adsorption of arsenate on ferric hydroxides in an aqueous environment reported a ΔG_{ads} of −55 kJ/mol and an activation barrier of +112 kJ/mol for the formation of the neutral BB complex from the MM complex. This

study shows general agreement with data reported in this paper but the activation barrier of +26 kJ/mol is much lower. The most significant difference between the two studies is the addition of explicit water molecules in our calculations. The inherently unstable transition state complex (Figure 3.6) could be stabilized via bonding to explicit water molecules. This is a known effect and can be quite pronounced, referred to as water-assisted reaction[82] or water-catalyzed reaction.[83] Understanding the role that explicit water molecules have in lowering the activation energy remains an area of current research.[84,85]

3.3.4 Desorption Thermodynamics

Arsenic contaminated manure that gets applied to agricultural fields also contains phosphate and organic compounds that compete for reactive sites on soil. The interaction of arsenicals with competing phosphate and organic compounds can determine their fate and mobility. To understand the effects arsenate and organics have on pAsA complexes, Gibbs free energies of desorption (ΔG_{des}) are calculated for a number of reactions.

When $pAsA^-$ leaves due to $H_2PO_4^-$ (phosphate) acting as a desorbing agent, the neutral bidentate binuclear HPO_4/iron oxide complex forms as, shown in Figure 3.8. Likewise, when $pAsA^-$ leaves due to $C_2O_4^{-2}$ (oxalic acid) acting as a desorbing agent, the negatively charged bidentate mononuclear (BM) C_2O_4/iron oxide complex forms, as shown in Figure 3.9. The energies of the complexes and the molecules needed for the desorption reactions are shown in Table 3.5 below, while the calculated ΔH_{des}, ΔG_{des} and

ΔS_{des} for the hypothetical desorption reactions of pAsA/iron oxide complexes with phosphate and oxalic acid as desorbing agents are shown in Table 3.6.

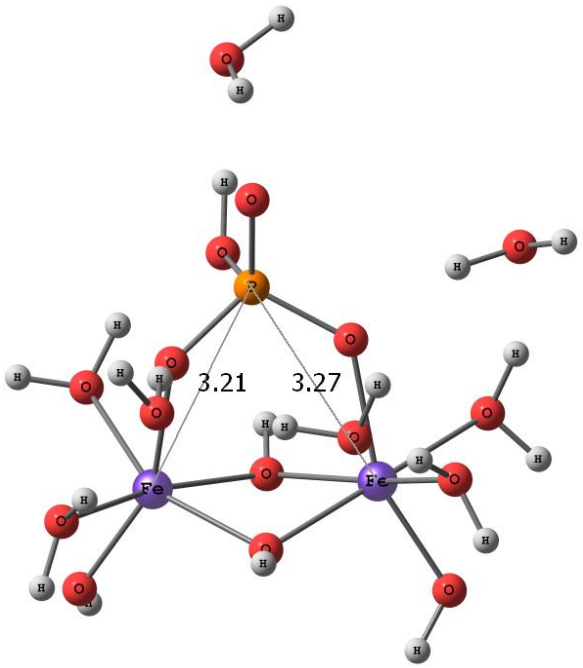

Figure 3.8 Energy minimized geometry of phosphate complex with iron oxyhydroxide. Calculated using B3LYP/6-311+G(d,p) and IEFPCM.

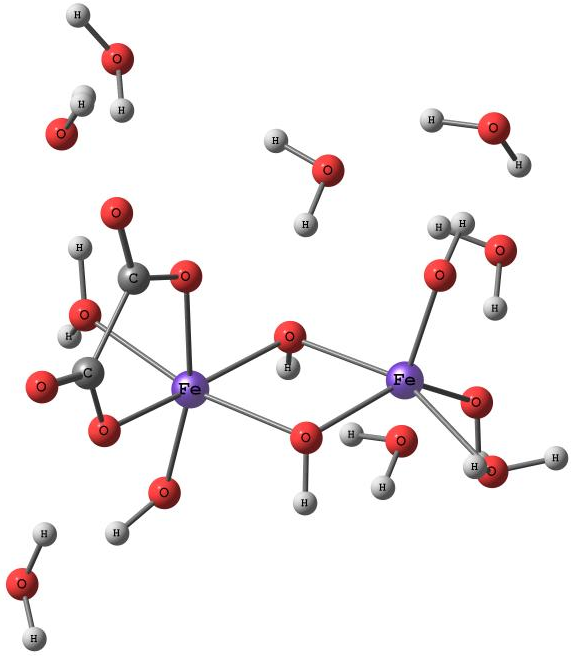

Figure 3.9 Energy minimized geometry of oxalic acid complex with iron oxyhydroxide. Calculated using B3LYP/6-311+G(d,p) and IEFPCM.

Table 3.5 Electronic energies (E_0), thermal corrections to enthalpy (H_{corr}), thermal corrections to Gibbs free energy (G_{corr}) and their sums ($E_0 + H_{corr}$) and ($E_0 + G_{corr}$) in atomic units for reactants and products needed in hypothetical desorption reactions. Optimized using B3LYP/6-311+G(d,p) and IEFPCM solvation.

Reactants	**Energy (E_0)**	**H_{corr}**	**G_{corr}**	**$E_0 + H_{corr}$**	**$E_0 + G_{corr}$**
$H_2PO_4^- \cdot (H_2O)_4$ (Phosphate)	-949.76309	0.15348	0.08763	-949.60960	-949.67545
$C_2O_4^{-2} \cdot (H_2O)_4$ (Oxalic Acid)	-683.46499	0.13841	0.06846	-683.32658	-683.39653
OS pAsA $\cdot (H_2O)_4$ $Fe_2(OH)_4(OH_2)_4$	-6268.05485	0.44342	0.32345	-6267.61143	-6267.73140
MM pAsA-$Fe_2(OH)_5(OH_2)_3 \cdot (H_2O)_5$	-6268.06994	0.44252	0.31756	-6267.62742	-6267.75239
BB pAsA-$Fe_2(OH)_5(OH_2)_3 \cdot (H_2O)_5$	-6268.05858	0.44182	0.31360	-6267.61676	-6267.74499
Products	**Energy (E_0)**	**H_{corr}**	**G_{corr}**	**$E_0 + H_{corr}$**	**$E_0 + G_{corr}$**
$pAsA^- \cdot (H_2O)_4$	-3055.39301	0.24932	0.17325	-3055.14369	-3055.21976
$pAsA^- \cdot (H_2O)_3$	-2978.91592	0.22195	0.15465	-2978.69396	-2978.76126
BB HPO_4-$Fe_2(OH)_4(OH_2)_4 \cdot (H_2O)_4$	-4085.95797	0.32009	0.21479	-4085.63788	-4085.74318
BM C_2O_4-$Fe_2(OH)_5(OH_2)_2^- \cdot (H_2O)_7$	-3972.62589	0.36111	0.24208	-3972.26478	-3972.38381

The desorption of OS pAsA is highly favourable with both phosphate and oxalic acid, having a ΔG_{ads} = -27.6 and -45.0 kJ/mol respectively. As seen in Table 3.6 desorption favourability of pAsA decreases in the order of OS > BB > MM, with the desorption of the most stable MM pAsA complex being a thermodynamically unfavourable reaction with both phosphate and oxalic acid. From this data it seems that oxalic acid would be the stronger desorbing agent when compared to $H_2PO_4^-$ since only oxalic acid leads to a thermodynamically favourable reaction for the desorption of BB pAsA. However, when it comes to phosphate as a desorbing agent it has also been posited that the desorption of inner-sphere pAsA complexes may depend on the acidity of the environment. The double negatively charged phosphate species, HPO_4^{-2}, more

prevalent at pH values > 7, was shown to lead to more exothermic reactions when used as the desorbing agent.[86]

Table 3.6 Calculated ΔH_{des}, ΔG_{des} (kJ/mol) and ΔS_{des} (kJ/mol K) for hypothetical desorption reactions of pAsA/iron oxide complexes with phosphate and oxalic acid as desorbing agents. Optimized using B3LYP/6-311+G(d,p) and IEFPCM solvation.

pAsA desorption with Phosphate	ΔH_{des}	ΔG_{des}	ΔS_{des}
1. **$H_2PO_4^-$** · $(H_2O)_4$ + **OS** pAsA · $(H_2O)_4$ $Fe_2(OH)_4(OH_2)_4$ → **BB** HPO_4-$Fe_2(OH)_4(OH_2)_4$ · $(H_2O)_4$ + $pAsA^-$ · $(H_2O)_4$	-28.3	-27.6	-0.00248
2. **$H_2PO_4^-$** · $(H_2O)_4$ + **MM** pAsA-$Fe_2(OH)_5(OH_2)_3$ · $(H_2O)_5$ → **BB** HPO_4-$Fe_2(OH)_4(OH_2)_4$ · $(H_2O)_4$ + $pAsA^-$ · $(H_2O)_4$	+13.6	+27.5	-0.0465
3. **$H_2PO_4^-$** · $(H_2O)_4$ + **BB** pAsA-$Fe_2(OH)_5(OH_2)_3$ · $(H_2O)_5$ → **BB** HPO_4-$Fe_2(OH)_4(OH_2)_4$ · $(H_2O)_4$ + $pAsA^-$ · $(H_2O)_4$	-14.3	+8.08	-0.0752
pAsA desorption with Oxalic Acid	ΔH_{des}	ΔG_{des}	ΔS_{des}
4. **$C_2O_4^{-2}$** · $(H_2O)_4$ + **OS** pAsA · $(H_2O)_4$ $Fe_2(OH)_4(OH_2)_4$ → **BM** C_2O_4-$Fe_2(OH)_5(OH_2)_2^-$ · $(H_2O)_7$ + $pAsA^-$ · $(H_2O)_3$	-54.4	-45.0	-0.0316
5. **$C_2O_4^{-2}$** · $(H_2O)_4$ + **MM** pAsA-$Fe_2(OH)_5(OH_2)_3$ · $(H_2O)_5$ → **BM** C_2O_4-$Fe_2(OH)_5(OH_2)_2^-$ · $(H_2O)_7$ + $pAsA^-$ · $(H_2O)_3$	-12.5	+10.1	-0.0757
6. **$C_2O_4^{-2}$** · $(H_2O)_4$ + **BB** pAsA-$Fe_2(OH)_5(OH_2)_3$ · $(H_2O)_5$ → **BM** C_2O_4-$Fe_2(OH)_5(OH_2)_2^-$ · $(H_2O)_7$ + $pAsA^-$ · $(H_2O)_3$	-40.4	-9.33	-0.104

3.3.5 Spectroscopic Analysis of pAsA adsorption

Theoretical studies can also aid in the interpretation and assignment of spectral features observed with ATR-FTIR for pAsA/iron oxyhydroxides complexes.[87] Table 3.7 shows the calculated stretching frequencies, ν(As−O), after adjusting for anharmonicity by a scaling factor of 1.0307. This scaling factor was calculated to minimize the residual between experimental and computational data for arsenicals and iron oxyhydroxide molecules at the B3LYP/6-311+G(d,p) IEFPCM level of theory.[88] Medium and strong vibrations, with an As-O bond stretch greater than 0.2 Å, were

considered meaningful and tabulated, while the weaker ν(As−O) vibrations below this limit were omitted from Table 3.7.

Table 3.7 Calculated ν(As-O) frequencies (cm^{-1}) for pAsA/iron oxyhydroxide complexes. Frequencies were adjusted for anharmonicity using a scaling factor of 1.0307.

OS complex	**ν(As-OFe)**	**ν(As-O)**	**ν(As-OH)**
OS pAsA · $(H_2O)_4$ $Fe_2(OH)_4(OH_2)_4$		**823, 828, 840, 853**	**629, 644**
MM complex	**ν(As-OFe)**	**ν(As-O)**	**ν(As-OH)**
MM pAsA-$Fe_2(OH)_5(OH_2)_3$ · $(H_2O)_5$	**830**	**892**	**603**
BB complex	**ν(As-OFe)**	**ν(As-O)**	**ν(As-OH)**
BB pAsA-$Fe_2(OH)_5(OH_2)_3$ · $(H_2O)_5$	**832**, **845**		**631, 648**

Experimental ν(As−O) results obtained from pAsA on goethite (FeOOH) show spectral features at 769, 789, 838 and 876 cm^{-1}, while for those on hematite (Fe_2O_3) spectral features are at 793, 840, and 883 cm^{-1}.[89] Figure 3.10 shows the correlation between experimental ν(As−O) values of pAsA on hematite (solid markers) and the theoretically calculated values listed in Table 3.7, as well as the correlation between experimental ν(As−O) values of pAsA on goethite (empty markers) and the theoretically calculated values listed in Table 3.7.

These results from experiment and theory support the idea that there can be formation of more than one type of surface complex for pAsA on iron oxyhydroxides, similar to other reports on the simultaneous formation of inner- and outer-sphere complexes of DMA with iron oxyhydroxides from experimental and DFT calculations.[90]

The spectral data in Table 3.7 also confirms that the 840 cm^{-1} spectral component that has been used to construct adsorption isotherms, pH envelopes, and kinetic curves[91,92,89] could arise from both inner- and outer-sphere surface complexes of pAsA. Experimental results also suggest that increasing organic substitution on the AsO_4 moiety increases the number of weakly bonded complexes.[93,94,95] This idea will be examined further as the DMA data are introduced.

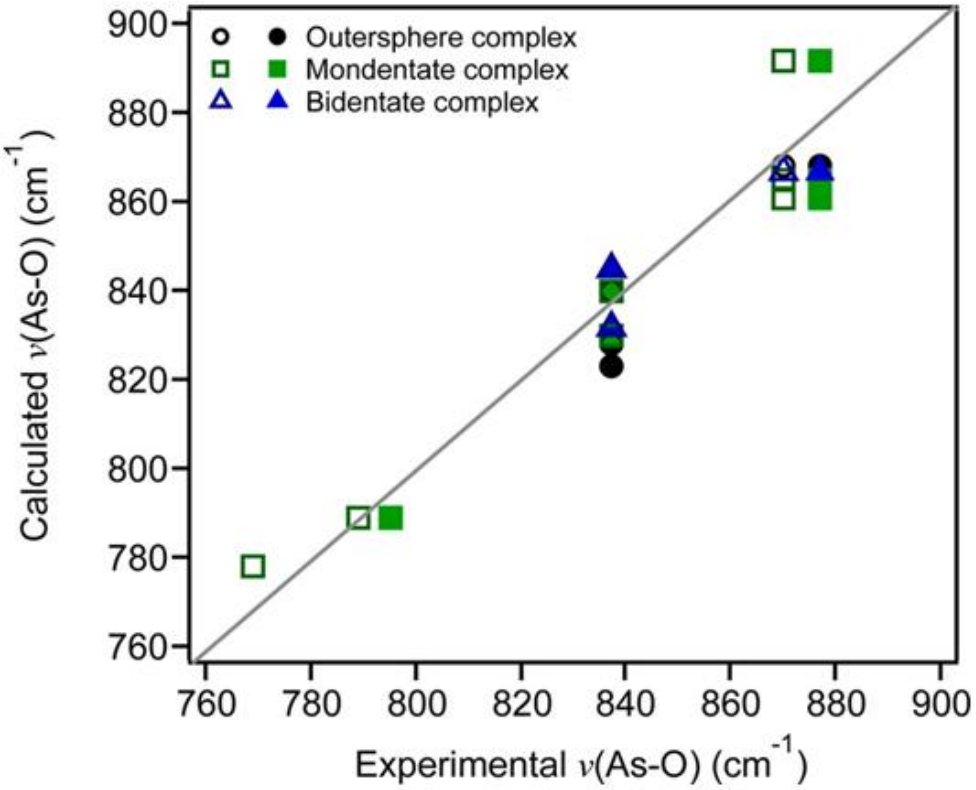

Figure 3.10 Correlation between experimental and calculated ν(As−O) frequencies with pAsA on hematite (soli markers) and goethite (empty markers). The vibrations from OS complexes are shown as black circles, the ones from MM complexes as green squares and the ones from BB complexes as blue triangles. Reprinted with permission from J. Phys. Chem. A, 2014, 118 (30), pp 5667–5679. Copyright 2014. American Chemical Society.

3.3.6 Dispersion Effects on pAsA complexes

Dispersion models deal with long range attractive van der Waals interactions that might be very useful in adsorption studies of this kind. This section analyses the effects that dispersion has on the OS, MM and BB pAsA complexes from Figure 3.5 when the GD3BJ dispersion model is introduced into the calculations. Figure 3.11 shows the optimized structures of the OS, MM and BB pAsA complexes with dispersion, while Table 3.8 compares the changes in the predicted As-O, Fe-O bond distances and As-Fe inter-atomic distances between complexes with and without dispersion. The data in Table 3.8 show that dispersion has an effect on the geometry of the pAsA complexes affecting in particular the inter-atomic distances, bringing the arsenical closer to the iron oxyhydroxide surface by 0.1 – 0.2 Å for the OS and MM complexes. The inter-atomic distances are mostly unaffected by dispersion for the BB complex.

Table 3.8 Comparison between predicted As-O, Fe-O bond distances (Å) and As-Fe inter-atomic distances (Å) of OS, MM and BB pAsA complexes with and without dispersion. Calculated with B3LYP/6-311+G(d,p) and IEFPCM with and without GD3BJ.

pAsA complexes	**As-Fe_1**	**As-Fe_2**	**As-O_1**	**As-O_2**	**As-C**	**As-OH**	**Fe_1-O_1**	**Fe_2-O_2**
OS pAsA complex	5.21	5.58	1.68	1.69	1.91	1.80	-	-
OS pAsA complex (GD3BJ)	5.09	5.40	1.68	1.69	1.90	1.79	-	-
MM pAsA complex	4.92	3.54	1.66	1.70	1.90	1.82	-	2.06
MM pAsA complex (GD3BJ)	4.74	3.52	1.66	1.70	1.90	1.82	-	2.06
BB pAsA complex	3.43	3.29	1.68	1.69	1.90	1.80	2.19	2.11
BB pAsA complex (GD3BJ)	3.41	3.27	1.68	1.69	1.89	1.80	2.19	2.11

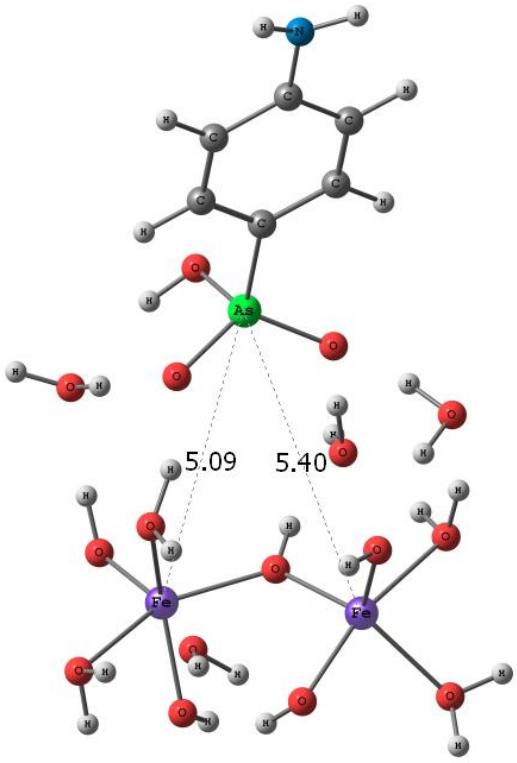

OS pAsA with GD3BJ dispersion

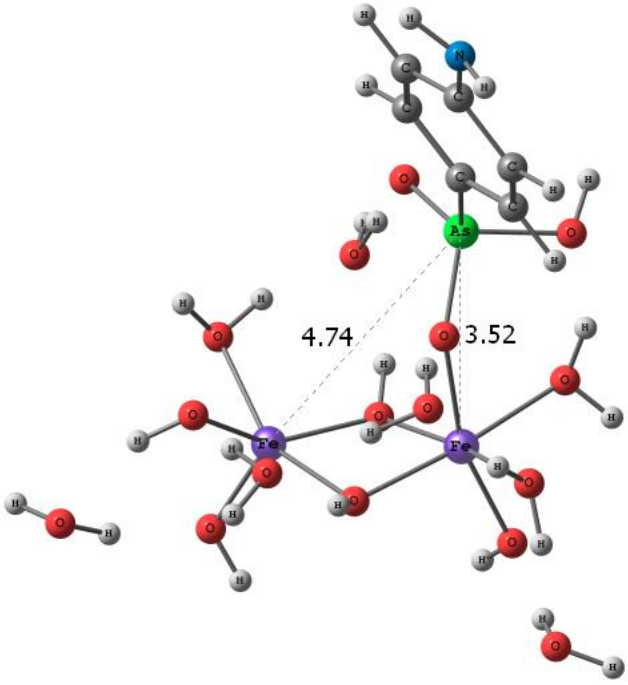

MM pAsA with GD3BJ dispersion

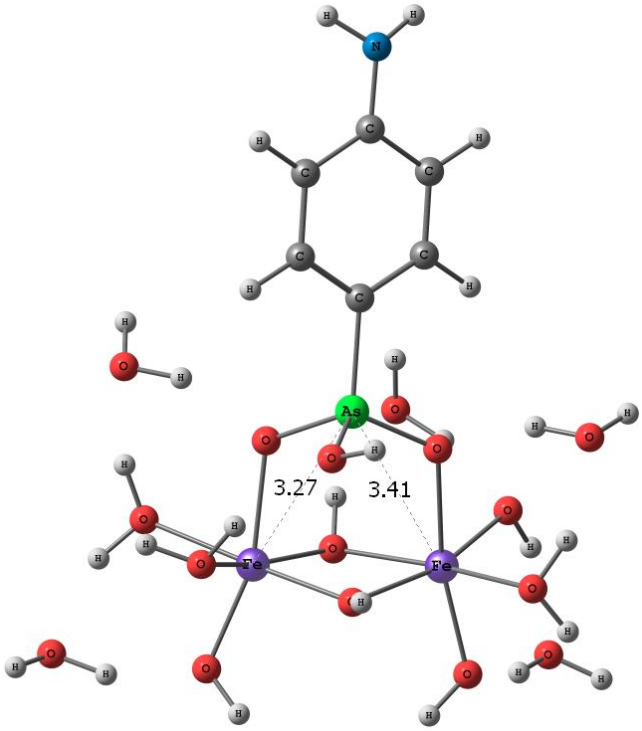

BB pAsA with GD3BJ dispersion

Figure 3.11 Energy minimized structures of pAsA complexes. Calculated using B3LYP/6-311+G(d,p) IEFPCM and GD3BJ dispersion.

The energies of the OS, MM and BB pAsA complexes are shown in Table 3.9. Also shown in Table 3.9 are the relative Gibbs free energy values for the OS and BB complexes relative to the lowest energy MM complex (i.e. ΔΔG) in kJ/mol, calculated similarly as the data shown in Figure 3.7. As observed from the calculated ΔΔG, the BB complex is less thermodynamically favourable than the MM complex, as is also the case without dispersion. However, adding dispersion brings the two complexes much closer together in energies with a ΔΔG = +3.67 kJ/mol between the MM and BB complexes, when compared to ΔΔG = +19.4 kJ/mol between the MM and BB complexes shown in Figure 3.7. The ΔΔG value for the OS complexes relative to MM did not differ much when comparing the case with and without dispersion (+58.1 kJ/mol vs. +55.1 kJ/mol respectively).

Table 3.9 Electronic energies (E_0), thermal corrections to enthalpy (H_{corr}), thermal corrections to Gibbs free energy (G_{corr}) and their sums ($E_0 + H_{corr}$) and ($E_0 + G_{corr}$) in atomic units for OS, MM and BB complexes of pAsA with iron oxyhydroxide with the ΔΔG relative to the MM complex shown in kJ/mol. Optimized using B3LYP/6-311+G(d,p) and IEFPCM with *GD3BJ*.

pAsA Complexes	**Energy (E_0)**	**$E_0 + H_{corr}$**	**$E_0 + G_{corr}$**
OS pAsA · $(H_2O)_4$ $Fe_2(OH)_4(OH_2)_4$	-6268.16505	-6267.721237	-6267.840344
MM pAsA-$Fe_2(OH)_5(OH_2)_3$ · $(H_2O)_5$	-6268.18186	-6267.738843	-6267.862480
BB pAsA-$Fe_2(OH)_5(OH_2)_3$ · $(H_2O)_5$	-6268.17450	-6267.732080	-6267.861082
			ΔΔG (kJ/mol)
MM pAsA-$Fe_2(OH)_5(OH_2)_3$ · $(H_2O)_5$ → **OS** pAsA · $(H_2O)_4$ $Fe_2(OH)_4(OH_2)_4$			**+58.1**
MM pAsA-$Fe_2(OH)_5(OH_2)_3$ · $(H_2O)_5$ → **BB** pAsA-$Fe_2(OH)_5(OH_2)_3$ · $(H_2O)_5$			**+3.67**

From the data in Tables 3.8 and 3.9 where dispersion is used and the comparison with the previous OS, MM and BB complexes in this section, it is clear that dispersion corrections have an effect on the optimized geometries, affecting inter-atomic distances, particularly the OS and MM complexes, as well as the Gibbs free energies, as seen from the much smaller difference in the ΔΔG between the MM and BB complexes when using dispersion, compared to the one without dispersion (Figure 3.7). Moving forward, all calculations for the organo-arsenicals DMA and MMA will include the GD3BJ dispersion model.

3.4 Conclusions

The pAsA results reported in this chapter show that the formation of inner- and outer-sphere complexes of pAsA with iron oxyhydroxide is thermodynamically favourable and that the formation of the MM complex is the most favourable. Transition state calculations showed that activation energies of +23.4 kJ/mol are required to form the BB pAsA complex as it transitions from the MM complex. Desorption energies of pAsA showed that the desorption of the outer-sphere complex is highly favourable with both phosphate and oxalic acid as the desorbing agents, but that favourability of pAsA desorption decreases in the order of OS > BB > MM, with the desorption of the MM complex being slightly unfavourable.

Frequency calculations confirm that the 840 cm^{-1} spectral component used previously to construct adsorption isotherms, pH envelopes, and kinetic curves arises from both inner- and outer-sphere surface complexes of pAsA. Combined with data

about thermodynamic favourability and the transition state calculation, it is likely that this 840 cm^{-1} spectral component has major contributions from monodentate pAsA complexes.

Adding dispersion to the calculations was shown to affect the inter-atomic distances of outer-sphere and monodentate pAsA the most, bringing the pAsA molecule closer to the iron oxyhydroxide surface. Dispersion corrections also bring the energies of the monodentate and bidentate pAsA complexes closer together, with the MM pAsA complex still being the most favourable.

CHAPTER IV. Sorption of Dimethylarsinic Acid onto Hydrated Iron (III) Oxyhyhroxide Clusters

4.1 Overview

Reaction pathway information and transition states are essential for understanding the adsorption mechanisms of DMA at the liquid–solid interface. A detailed computational analysis of the complexes of DMA on iron oxyhydroxides that includes activation energies, transition states, Gibbs free energies of adsorption, Mulliken charges and charge redistribution upon adsorption is presented in this chapter. The As–O bond stretching vibrations are also analysed and compared with experimental spectroscopic data. Dispersion corrections are included because experimentally DMA tends to form mostly outer-sphere complexes. It is shown that dispersion corrections are important when dealing with outer-sphere complexes and that there is a high activation barrier of roughly +43 kJ/mol in the transition from the monodentate to bidentate DMA complex. Additionally, the extended iron oxyhydroxide surface with four Fe centres is introduced and analysis of the charge distribution upon adsorption of DMA reveals that electrostatics may play a role in the transition from outer-sphere to monodentate complexes.

4.2 Introduction

Dimethylarsinic acid (DMA) is an important organo-arsenical detected in arsenic speciation studies of environmental samples. It is created as a byproduct in the pyrolysis of oil shale[96] and has also been used as a herbicide in the past.[97] Bio-methylation through the Challenger mechanism (Figure 1.1) can also transform inorganic forms of arsenic into DMA.[98] Since DMA has a lower affinity to iron oxides when compared to iAs and other organoarsenicals, it is also more mobile in the environment.[99] Higher mobility also poses a greater risk of contamination, such as nearby water supplies. DMA have also been detected in the leachates of landfills rich in waste containing arsenic such as glass, alloys, and semiconductors[100] and in the urine of animals as metabolic products of inorganic arsenic.[101]

In this chapter the optimized geometries of DMA in aqueous solution and DMA bound to iron oxyhydroxide clusters are evaluated. The effects on DMA adsorption when extending the iron oxyhydroxide surface to 4 core Fe atoms is analyzed and are compared to the smaller 2Fe surface. Theoretical infrared spectra will again be analyzed and calculated Gibbs free energies, enthalpies and entropies of adsorption for various types of ligand exchange reactions are calculated and compared for the 2Fe and 4Fe clusters. Moreover, Mulliken charges are calculated for each complex to gain greater insight into how charge redistributes upon adsorption, as well as study the electrostatics interactions between the negatively charged arsenical and the positively charged iron oxyhydroxide surface.

4.3 Results and Discussion

4.3.1 DMA complexation with iron oxyhydroxides

The optimized geometry of hydrated DMA is shown in Figure 4.1 below. The molecule is very symmetrical, so the d(As-O) values are both 1.70 Å and the d(As-C) values are 1.94 Å. The adsorption of DMA onto iron oxyhydroxides produces the OS, MM and BB configurations. In this case however we compare how the 2Fe and 4Fe complexes differ. The outer-sphere 2Fe and 4Fe DMA complexes are shown in Figure 4.2 below.

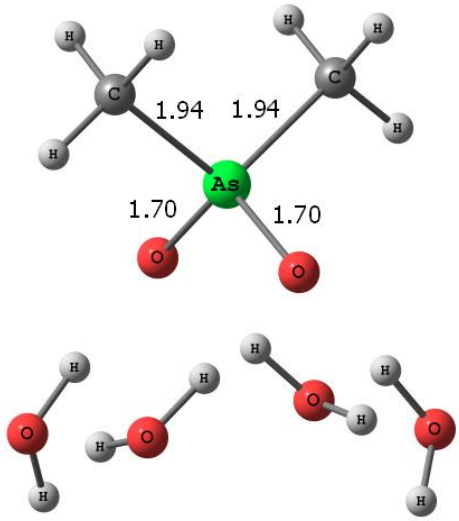

Figure 4.1 Energy minimized structure of hydrated DMA.
Calculated using B3LYP/6-311+G(d,p) IEFPCM and GD3BJ dispersion.

The immediate differences between the two OS complexes are their inter-atomic distances. The d(As-Fe) values for the OS(2Fe) DMA complex are 4.81 and 4.72 Å, while the d(As-Fe) values for the OS(4Fe) DMA complex are 5.50 and 5.92 Å. Similarly, the optimized MM(2Fe) and MM(4Fe) DMA complexes are shown in Figure

4.2 below with inter-atomic d(As-Fe) distances 3.36 and 4.05 Å for the MM(2Fe) complex and 3.40 and 4.76 Å for the MM(4Fe) complex. This is a difference greater than 15% between the two Fe modelled surfaces.

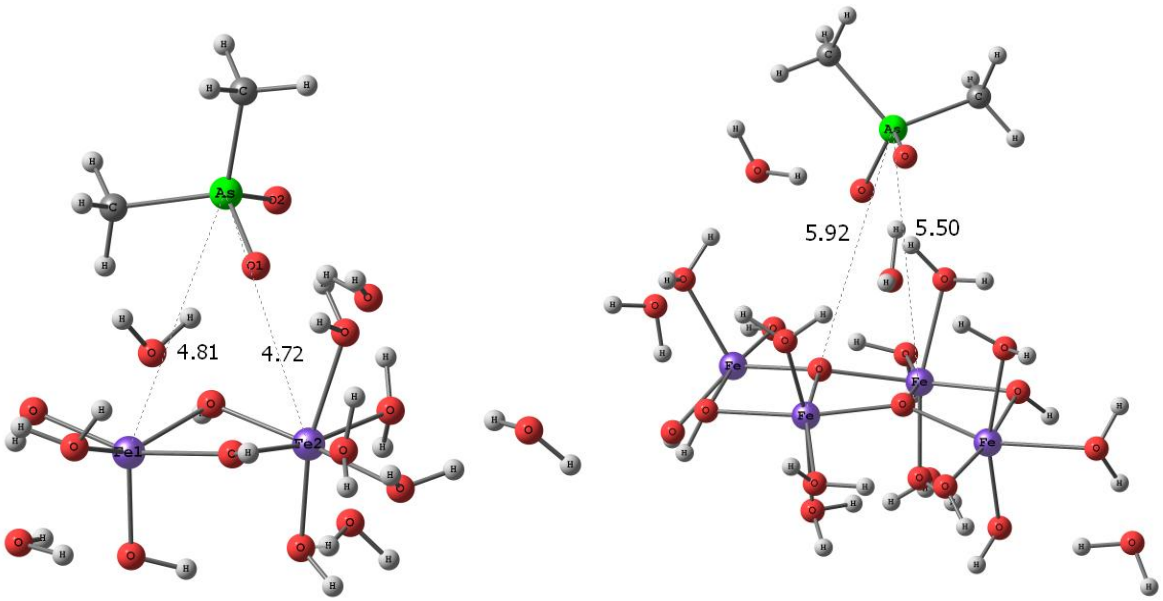

Figure 4.2 Energy minimized structures of OS(2Fe) and OS(4Fe) DMA Complexes. Calculated using B3LYP/6-311+G(d,p) IEFPCM and GD3BJ dispersion.

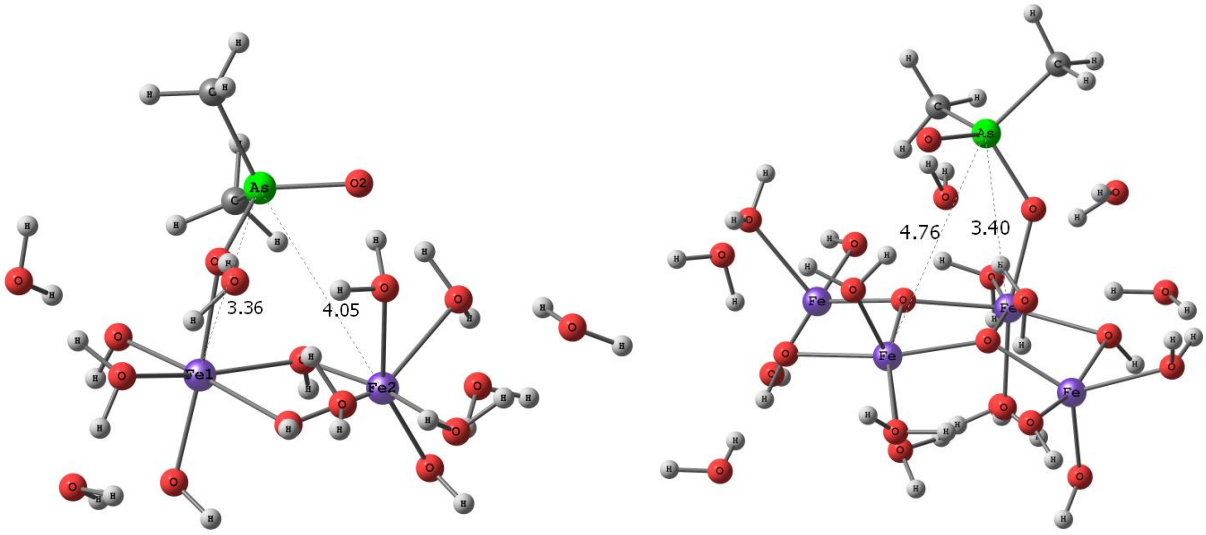

Figure 4.3 Energy minimized structures of MM(2Fe) and MM(4Fe) DMA Complexes. Calculated using B3LYP/6-311+G(d,p) IEFPCM and GD3BJ dispersion.

The effects of the two extra Fe atoms are more noticeable when comparing the OS complexes (Figure 4.2) with a difference greater than 20% in their d(As-Fe) inter-atomic distances. The MM complexes also show a difference greater than 15% in their d(As-Fe) inter-atomic distances. The inter-atomic distances of the OS complex, with the extended 4Fe surface, are more consistent with experimental d(As-Fe) values reported, that show distances greater than 5.0 Å for arsenate OS species.[102] The extra Fe-atoms create a wider surface that hinders an over-relaxation of the complex. As the DMA comes closer to the adsorption site of the 2Fe surface, it is observed that the model cluster becomes distorted since the DMA molecule has more freedom to tilt and wrap around the sides of the cluster to find its optimal minimum energy. It is observed that for the extended OS(4Fe) and MM(4Fe) clusters there is no wrapping around the surface and the DMA molecule has its methyl groups sticking up, perpendicular to the surface, whereas they are tilted to the side for the OS(2Fe) and MM(2Fe) complexes. Hence, over-relaxation is partly responsible for the shorter d(As-Fe) values in the 2Fe clusters. Note that the two modelled surfaces are meant to be surrogates for a real iron oxyhydroxide surface. As such, the less distorted 4Fe DMA complexes would better resemble the global minima for a macroscopic surface.

This over-relaxation problem is not observed in the BB complexes, since the geometry is much more restricted. When comparing the BB complexes, the d(As-Fe) distances for the BB(2Fe) complex are 3.32 and 3.29 Å, while for the BB(4Fe) complex the d(As-Fe) distances are 3.34 and 3.27 Å, as shown in Figure 4.4. The geometries of all the 2Fe and 4Fe complexes of DMA are summarized in Table 4.1 below. It is also

observed from Table 4.1 that adding dispersion shortens the d(As-Fe) distances when comparing the 2Fe complexes with those without dispersion in parentheses. This effect on the inter-atomic As-Fe distances was observed for pAsA in the previous chapter and was most noticeable for the OS and MM complexes.

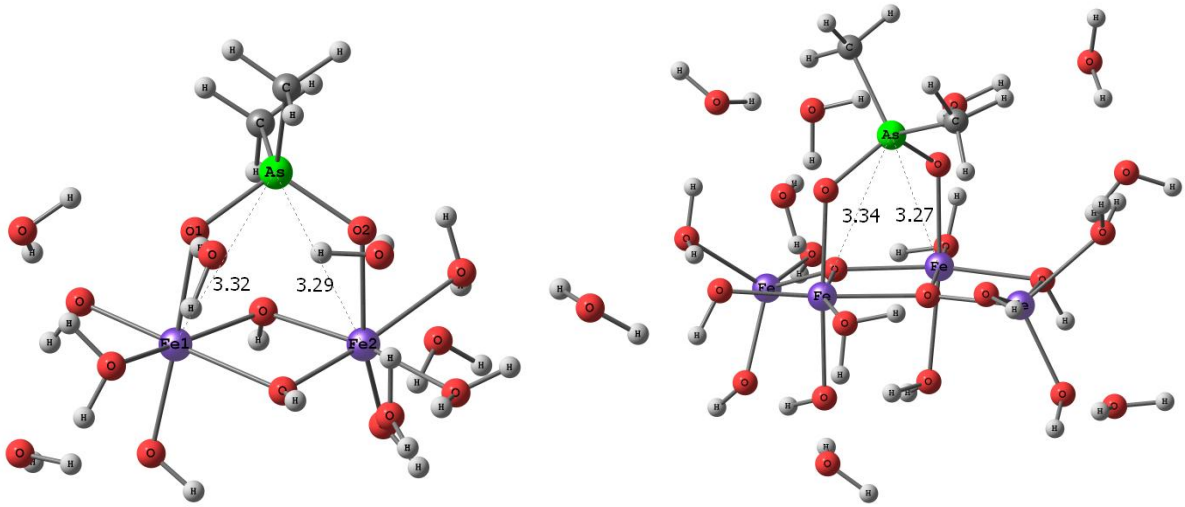

Figure 4.4 Energy minimized structures of BB(2Fe) and BB(4Fe) DMA Complexes. Calculated using B3LYP/6-311+G(d,p) IEFPCM and GD3BJ dispersion.

Table 4.1 Calculated As-O, Fe-O and As-Fe distances in Angstroms (Å) for DMA-iron oxyhydroxide complexes with 2 and 4 Fe centres. Calculated using B3LYP/6-311+G(d,p) IEFPCM and GD3BJ dispersion. The numbers in parentheses were calculated using the same method but *without* dispersion.[103]

DMA complexes	As-Fe_1	As-Fe_2	As-O_1	As-O_2	As-C_1	As-C_2	Fe_1-O_1	Fe_2-O_2
OS(2Fe)	4.81	4.72	1.72	1.69	1.93	1.93	-	-
	(5.28)	(4.84)	(1.70)	(1.71)	(1.94)	(1.94)		
OS(4Fe)	5.50	5.92	1.71	1.69	1.94	1.94	-	-
MM(2Fe)	3.36	4.05	1.72	1.70	1.93	1.93	2.06	-
	(3.36)	(5.05)	(1.70)	(1.73)	(1.93)	(1.93)		
MM(4Fe)	3.40	4.76	1.73	1.68	1.93	1.93	1.96	-
BB(2Fe)	3.32	3.29	1.71	1.72	1.93	1.93	2.11	2.07
	(3.36)	(3.43)	(1.74)	(1.71)	(1.93)	(1.93)		
BB(4Fe)	3.34	3.27	1.70	1.73	1.92	1.93	2.07	2.01

Figure 4.5 shows stepwise optimization calculations along the reaction pathway of DMA as it goes from an OS complex to form the MM complex with an electronic activation barrier of +18.6 kJ/mol. The peak along this reaction pathway is used to find the transition state between the OS and MM complex (TS1) as explained in the theoretical section. The transition state TS1 computed this way is shown in Figure 4.6. The inter-atomic distances for the TS1 transition state are d(As-Fe_1) = 4.07 Å and d(As-Fe_2) = 4.74 Å. Similarly, Figure 4.7 shows the stepwise optimization calculations along the reaction pathway of DMA as it goes from a MM to a BB complex with an electronic activation barrier of +42.2 kJ/mol. At this point it is also important to note that the large drops in energy of the reaction pathways seen in Figures 4.5 and 4.7 are due to the formation of new hydrogen bonds that render the structure more stable. The forming and breaking of hydrogen bonds as the reactions proceeds is also the reason for the asymmetry in these potential profiles. Thus, reversing these reactions to take the path from product back to reactant will not produce exactly the same profile, albeit similar activation barriers would be expected.

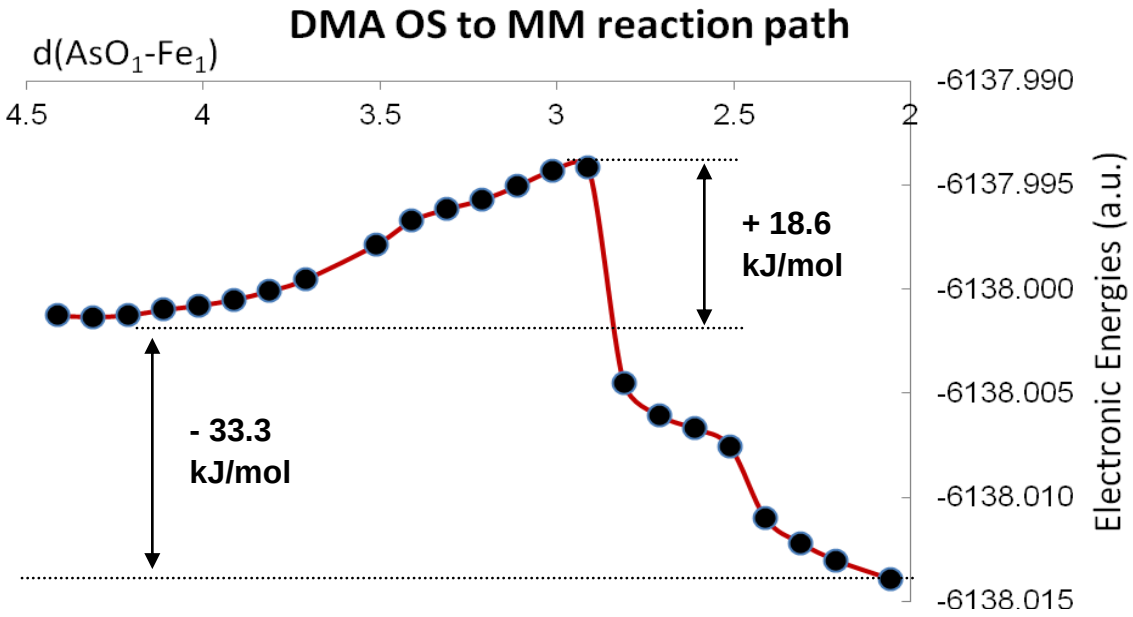

Figure 4.5 Electronic energies for the transition from OS to MM DMA-iron oxyhydroxide complex. The MM complex is lower in energy than the OS complex by -33.3 kJ/mol and there is an activation barrier of +18.6 kJ/mol.

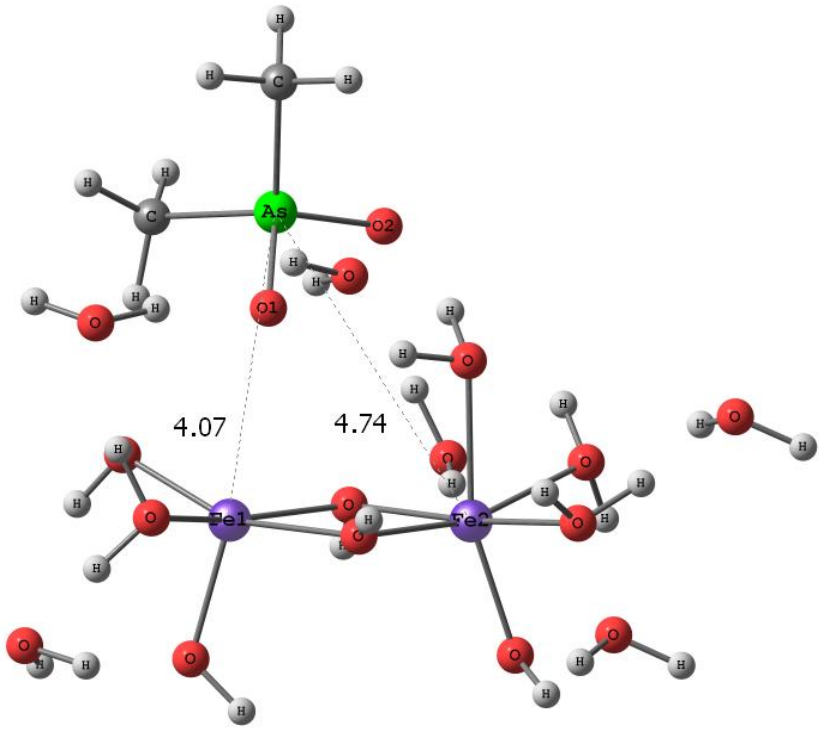

Figure 4.6 Optimized structure of DMA transition state complex TS1. Calculated using B3LYP/6-311+G(d,p) with IEFPCM and GD3BJ dispersion.

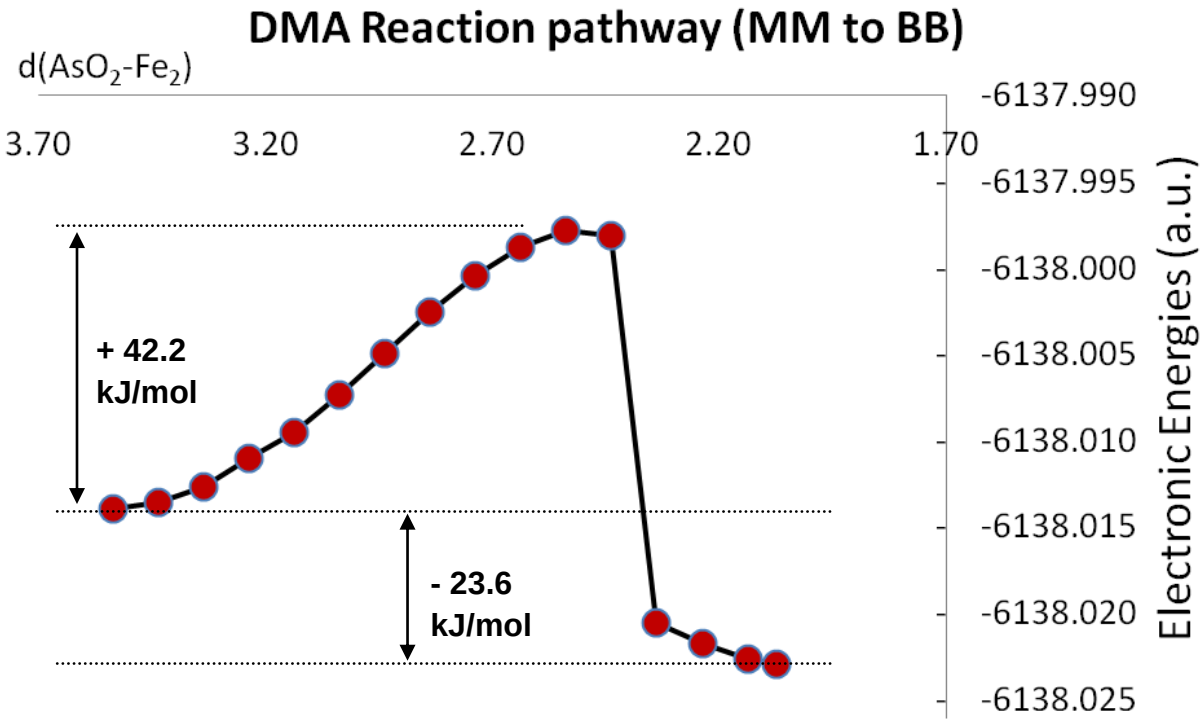

Figure 4.7. Electronic energies for the transition from a MM to a BB DMA/iron oxyhydroxide complex. The BB complex is lower in energy than the MM complex by -23.6 kJ/mol and there is an activation barrier of +42.2 kJ/mol.

A higher activation barrier is likely the reason that DMA forms mostly OS and MM rather than BB on iron oxyhyroxides, as experiments over 100 minutes of reaction time have shown.[104,105] The larger energy barrier for the formation of the BB complex may stem from the inability of the polar water molecules to stabilize the nonpolar methyl groups in the transition state geometry. This is not the case for arsenate, as seen in Appendix B – Figure B2, where there are multiple smaller activation barriers in the transition from MM to BB ranging from +6.91 to +12.9 kJ/mol. These multiple smaller activation barriers in the arsenate system are attributed to the breaking and forming of new hydrogen bonds with the water molecules and hydroxyl groups of the iron

oxyhyroxide as the arsenate molecule moves closer. These small peaks in the transition from MM to BB for arsenate are in contrast with the DMA system where there is one big activation barrier (Figure 4.7) for the MM to BB transition.

Similarly to TS1 in Figure 4.6, the transition state TS2 shown in Figure 4.8 was calculated starting with the geometry from the highest point on the MM to BB pathway in Figure 4.7. The inter-atomic distances for TS2 are d(As-Fe_1) = 3.35 Å and d(As-Fe_2) = 3.54 Å. Both transition states TS1 and TS2 had a the negative frequency and animating it showed the movement from reactant to product. IRC calculations were also conducted for the DMA transition state between MM and BB as seen in Figure C1 and Table C1 in Appendix C, confirming that indeed the transition state connects reactant to product.

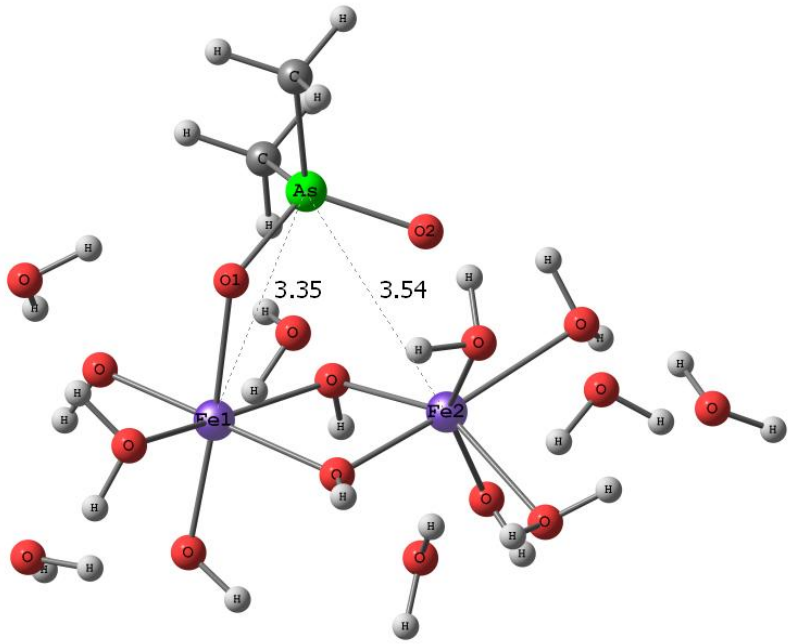

Figure 4.8 Optimized structure of DMA transition state complex TS2. Calculated using B3LYP/6-311+G(d,p) with IEFPCM and GD3BJ dispersion.

4.3.2 DMA Adsorption Thermodynamics

Table 4.2 shows the calculated electronic energies, E_0, as well as the electronic energies with the thermal corrections to enthalpies ($E_0 + H_{corr}$) and Gibbs free energies ($E_0 + G_{corr}$) for all the reactants and products needed in the adsorption reactions of DMA^- with the positively charged Fe2 and Fe4 surface clusters to form the neutral OS, MM and BB complexes. The ΔH_{ads}, ΔG_{ads} and ΔS_{ads} for various hypothetical reactions are then calculated using the value in Table 4.2 and Equations 2.13, 2.14 and 2.15 respectively and tabulated Table 4.3.

The enthalpies, Gibbs free energies and entropies of the transition state DMA complexes TS1 and TS2 are also calculated and listed in Table 4.3 in order to derive free energy activation barriers for these reactions. As seen from Table 4.3, the trend in the values of ΔG_{ads} show that the formation of the BB complex is the most thermodynamically favourable, for both the 2Fe and 4Fe complexes followed by MM and OS. The ΔG_{ads} values are -93.4, -68.2 and -39.9 kJ/mol for BB(2Fe), MM(2Fe) and OS(2Fe) respectively and -107, -59.6 and -52.3 kJ/mol for BB(4Fe), MM(4Fe) and OS(4Fe) respectively. The values in Table 4.3 can also be compared to the experimentally measured ΔH_{ads} value of -102 kJ/mol for the adsorption of DMA onto hematite nanoparticles.[105]

Table 4.2 Electronic Energies (E_0), Electronic Energies with Thermal Corrections to Enthalpy ($E_0 + H_{corr}$) and Electronic Energies with Thermal Corrections to Gibbs free Energy ($E_0 + G_{corr}$) for DMA/Iron Oxyhydroxide Complexes. Calculated using B3LYP/6-311+ G(d,p) with IEFPCM solvation and GD3BJ dispersion models.

Reactants	**(E_0)**	**($E_0 + H_{corr}$)**	**($E_0 + G_{corr}$)**
$DMA^- \cdot (H_2O)_4$	-2772.32700	-2772.12954	-2772.19608
$[\mathbf{Fe_2}(OH)_5(OH_2)_5]^+ \cdot (H_2O)_4$	-3595.07854	-3594.74811	-3594.84670
$[\mathbf{Fe_4}O_2(OH)_7(OH_2)_8]^+ \cdot (H_2O)_5$	-6730.89335	-6730.40782	-6730.54111
Fe2 DMA Clusters			
(Fe2) **OS** DMA $\cdot (H_2O)_6$ $Fe_2(OH)_5(OH_2)_4$	-6138.00126	-6137.55443	-6137.67821
TS1 DMA $\cdot (H_2O)_6$ $Fe_2(OH)_5(OH_2)_4$	-6137.99416	-6137.54850	-6137.67400
(Fe2) **MD** DMA-$Fe_2(OH)_5(OH_2)_4 \cdot (H_2O)_6$	-6138.01393	-6137.56603	-6137.68900
TS2 DMA-$Fe_2(OH)_5(OH_2)_4 \cdot (H_2O)_6$	-6137.99808	-6137.55040	-6137.67257
(Fe2) **BD** DMA-$Fe_2(OH)_5(OH_2)_3 \cdot (H_2O)_7$	-6138.02294	-6137.57466	-6137.69862
Fe4 DMA Clusters			
(Fe4) **OS** DMA $\cdot (H_2O)_5$ $Fe_4O_2(OH)_7(OH_2)_8$	-9197.33430	-9196.76283	-9196.91842
(Fe4) **MM** DMA-$Fe_4O_2(OH)_7(OH_2)_7 \cdot (H_2O)_6$	-9197.34267	-9196.76876	-9196.92120
(Fe4) **BB** DMA $Fe_4O_2(OH)_7(OH_2)_6 \cdot (H_2O)_7$	-9197.36490	-9196.78860	-9196.93938
Leaving Water Clusters			
$(H_2O)_3$	-229.41801	-229.33785	-229.37974
$(H_2O)_4$	-305.90291	-305.79462	-305.83868
$(H_2O)_6$	-458.86134	-458.69741	-458.75509

Table 4.3 Values of ΔH_{ads}, ΔG_{ads} and ΔS_{ads} for reactions of DMA with Iron Oxyhydroxide Clusters. Calculated using B3LYP/6-311+G(d,p) with IEFPCM solvation and GD3BJ dispersion.

DMA adsorption on 2Fe surface **DMA$^-$** · $(H_2O)_4$ + [**Fe$_2$**$(OH)_5(OH_2)_5]^+$ · $(H_2O)_4$ →	**$\Delta H°_{ads}$ (kJ mol^{-1})**	**$\Delta G°_{ads}$ (kJ mol^{-1})**	**$\Delta S°_{ads}$ (kJ mol^{-1}K^{-1})**
OS(2Fe) DMA · $(H_2O)_6$ $Fe_2(OH)_5(OH_2)_4$ + $(H_2O)_3$	**-38.4**	**-39.9**	**+0.00483**
TS1(2Fe) DMA ·$(H_2O)_6$ $Fe_2(OH)_5(OH_2)_4$ + $(H_2O)_3$	-22.8	-28.8	+0.0200
MM(2Fe) DMA-$Fe_2(OH)_5(OH_2)_4$ · $(H_2O)_6$ + $(H_2O)_3$	**-68.9**	**-68.2**	**-0.00228**
TS2(2Fe) DMA-$Fe_2(OH)_5(OH_2)_4$ ·$(H_2O)_6$ + $(H_2O)_3$	-27.8	-25.0	-0.00937
BB(2Fe) DMA-$Fe_2(OH)_5(OH_2)_3$ · $(H_2O)_7$ + $(H_2O)_3$	**-91.5**	**-93.4**	**+0.00638**
DMA adsorption on 4Fe surface **DMA$^-$** · $(H_2O)_4$ + [**Fe$_4$**$O_2(OH)_7(OH_2)_8]^+$ · $(H_2O)_5$ →	**$\Delta H°_{ads}$ (kJ mol^{-1})**	**$\Delta G°_{ads}$ (kJ mol^{-1})**	**$\Delta S°_{ads}$ (kJ mol^{-1}K^{-1})**
OS(4Fe) DMA · $(H_2O)_5$ $Fe_4O_2(OH)_7(OH_2)_8$	**-52.7**	**-52.3**	**-0.00152**
MM(4Fe) DMA-$Fe_4O_2(OH)_7(OH_2)_7$ · $(H_2O)_6$	**-68.3**	**-59.6**	**-0.0293**
BB(4Fe) DMA $Fe_4O_2(OH)_7(OH_2)_6$ · $(H_2O)_7$	**-120**	**-107**	**-0.0439**

Figure 4.9 shows the difference between ΔG_{ads} values of OS(2Fe), MM(2Fe) and BB(2Fe) complexes of DMA relative to the OS complex (i.e. the $\Delta\Delta G_{ads}$) and it includes the transition state geometries TS1 and TS2. The MM(2Fe) and BB(2Fe) complexes are lower in Gibbs free energy by -28.3 and -53.6 kJ mol^{-1} respectively, relative to the OS complex and the activation barrier from MM to BB is almost four times higher (+43.1 kJ/mol) than the activation barrier from OS to MM (+11.1 kJ/mol).

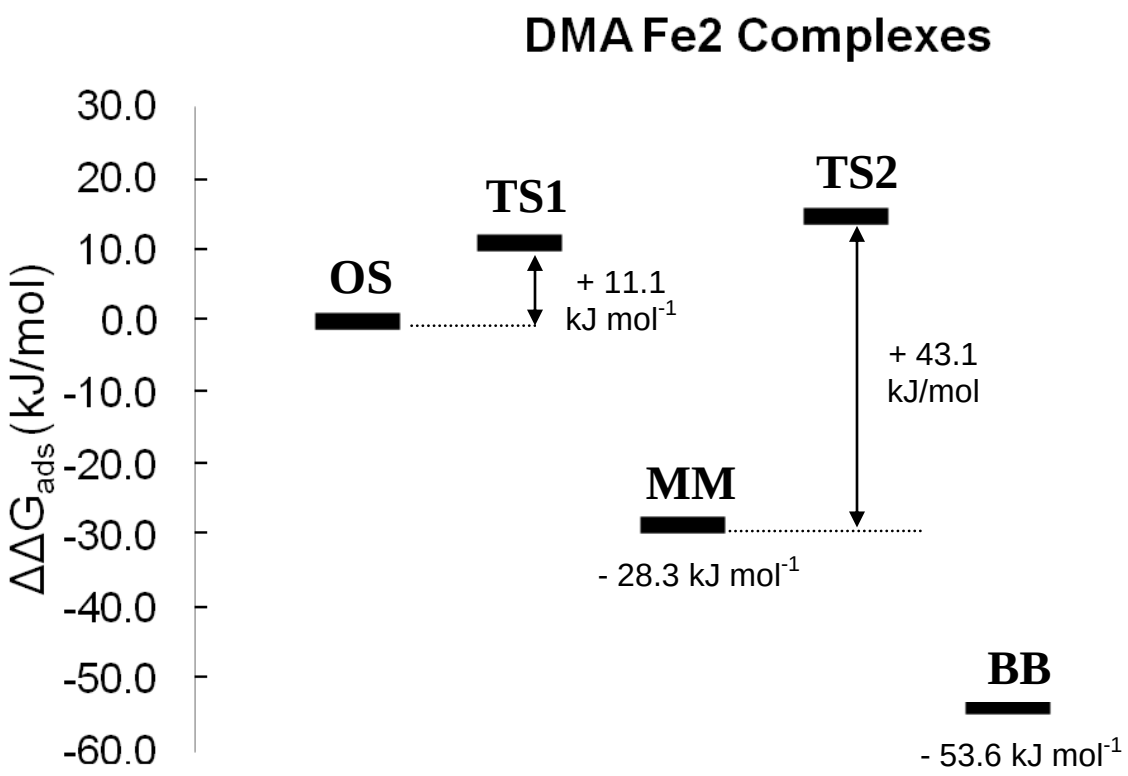

Figure 4.9 Difference in Gibbs free energies ($\Delta\Delta G_{ads}$) for DMA/(2Fe) clusters as per reactions listed in Table 4.3.

For comparison, a similar figure is included in Appendix B – Figure B3 for arsenate adsorption, showing the thermodynamic favourability of the MM and BB complexes with respect to the OS complex, at -51.5 and -82.8 kJ/mol respectively. A related study by Farrell and Chaudhary also reported calculations for arsenate adsorption on ferric hydroxides with a much higher activation barrier going from MM to BB than from OS to MM.[106] Their study however, showed higher activation barriers ranging from +62 to +73 kJ/mol for OS to MM and from +79 to +112 kJ/mol for MM to BB. The higher activation barriers seen in Farrell and Chaudhary's study can be explained by

the exclusion of explicit water molecules. As argued earlier the inclusion of explicit water molecules plays a major role in lowering the energy of the transition states.

The trend in the thermodynamic favourability (ΔG_{ads}) of DMA complex formation on the extended model 4Fe surface is similar to the 2Fe Surface: BB(4Fe) > MM(4Fe) > OS(4Fe). The formation of the BB complex is more favourable by 55.0 kJ mol^{-1} relative to the OS complex ($\Delta\Delta G_{ads}$), compared to 7.3 kJ mol^{-1} for the formation of the MD complex. The relative Gibbs free energies are shown in Figure 4.10 below.

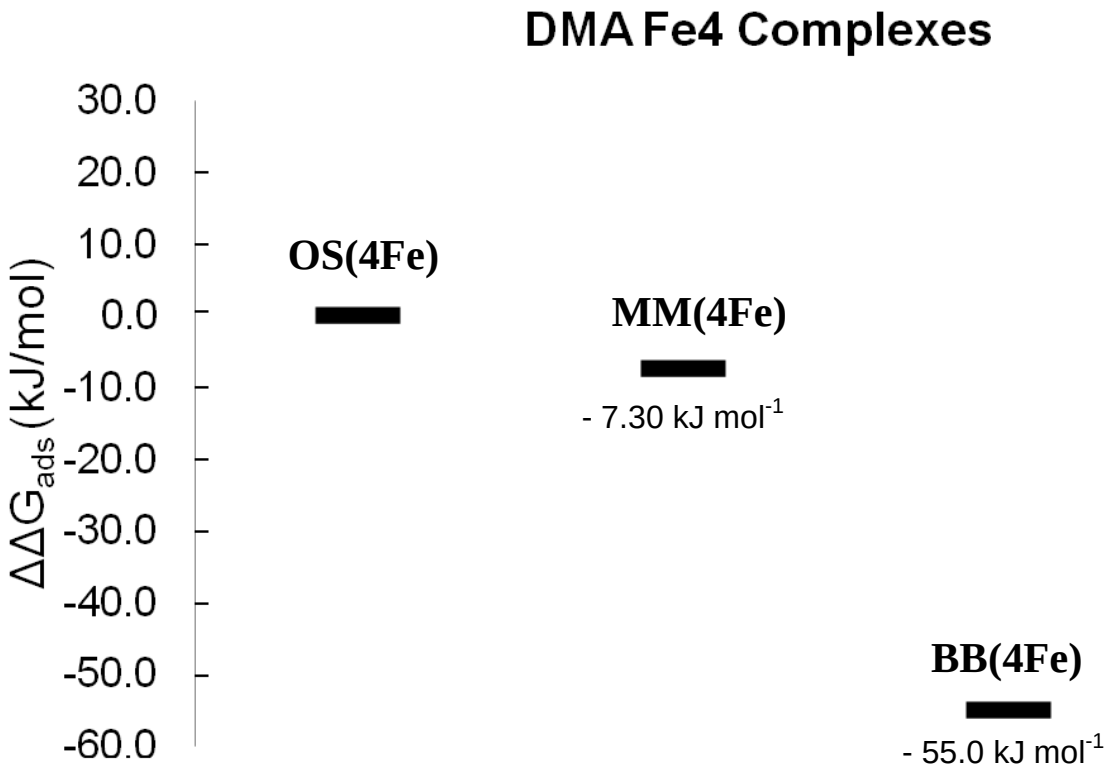

Figure 4.10 Difference in Gibbs free energies ($\Delta\Delta G_{ads}$) for DMA/(4Fe) iron oxyhydroxide clusters as per reactions listed in Table 4.3.

From Table 4.3 it is observed that there are similar energy differences between the BB and OS complexes when comparing the 4Fe and 2Fe complexes (-55.0 vs. -53.6 kJ/mol), but a greater difference between the MM and OS complexes (-7.30 vs. -26.3

kJ/mol). Thus, using the extended 4Fe surface shows that MM complex formation may be less thermodynamically favoured that the 2Fe model suggests. An explanation could also be the over-relaxation problem noted earlier. The DMA in the MM(2Fe) complex is allowed to wrap around the Fe surface and it ultimately finds a lower energy geometry. This effect is not visible in the case of MM(4Fe) because of a wider and more rigid surface that does not give the DMA molecule as much freedom to wrap around it and is thus less prone to over-relaxation. Hence, the extended 4Fe surface might tell a better (more realistic) story about the MM and OS complexes when using larger molecules that adsorb and can easily wrap around a smaller 2Fe surface. This is not the case for the BB complexes because the two covalent bonds with the iron oxyhydroxide surface keep the DMA molecule in place, regardless of the number of Fe atoms in the modelled surface.

4.3.3 Mulliken Charge Analysis

Allocating charges to the atoms in our OS, MM and BB DMA complexes is useful because it shows the distribution of the electron density in each complex, how it changes between the complexes, as well as the role that electrostatics may play in the adsorption process. Table 4.4 shows the Mulliken charge data of the DMA molecule, the 2Fe and 4Fe iron oxyhydroxide surfaces and the OS, MM and BB complexes they form.

Table 4.4 Mulliken charges for DMA/iron oxyhydroxide complexes with two Fe centers (top) and four Fe centres (bottom). Optimized using B3LYP/6-311+G(d,p) with IEFPCM solvation model and GD3BJ dispersion.

Atoms	Fe atoms	DMA	OS(2Fe) Complex	Δ MC*	MM(2Fe) Complex	Δ MC*	BB(2Fe) Complex	Δ MC*
Fe_1	0.7295		0.5230	-0.207	0.3633	-0.366	0.3831	-0.346
Fe_2	0.7629		0.6102	-0.153	0.8536	0.091	0.8009	0.038
Total Fe	**1.4924**		**1.1332**	**-0.359**	**1.2169**	**-0.275**	**1.1840**	**-0.308**
As		1.0534	1.1920	0.139	1.3204	0.267	1.2247	0.171
O_1		-0.8935	-0.8313	0.062	-0.6810	0.213	-0.6680	0.226
O_2		-0.8936	-0.9867	-0.093	-0.8769	0.017	-0.5944	0.299
Total O		**-1.7871**	**-1.8180**	**-0.031**	**-1.5579**	**0.229**	**-1.2624**	**0.525**
Atoms	**Fe atoms**	**DMA**	**OS(4Fe) Complex**	**Δ MC***	**MM(4Fe) Complex**	**Δ MC***	**BB(4Fe) Complex**	**Δ MC***
Fe_1	-0.07604		-0.28733	-0.211	-0.43847	-0.362	-0.33823	-0.262
Fe_2	0.19788		-0.52471	-0.723	-0.54318	-0.741	-0.55104	-0.749
Fe_3	0.66971		0.61621	-0.054	0.59560	-0.074	0.57869	-0.091
Fe_4	0.68788		0.52266	-0.165	0.45018	-0.238	0.46807	-0.220
Total Fe	**1.47943**		**0.32683**	**-1.153**	**0.06413**	**-1.415**	**0.15748**	**-1.322**
As		1.05340	1.16710	0.114	1.20060	0.147	1.308961	0.256
O_1		-0.89353	-0.86515	0.028	-0.71085	0.183	-0.357296	0.536
O_2		-0.89355	-0.95627	-0.063	-0.55242	0.341	-0.474140	0.419
Total O		**-1.78707**	**-1.82142**	**-0.034**	**-1.26326**	**0.524**	**-0.83144**	**0.956**

* ΔMC values are calculated by subtracting the Mulliken charge of the atoms in the vacant Fe oxyhydroxide and DMA molecule from the Mulliken charge of the same atoms in the Fe complexes.

The difference in Mulliken charge (ΔMC) was calculated relative to the uncomplexed 2Fe/4Fe surface and hydrated DMA and those of the OS, MM and BB complexes. Since both the Fe4 iron hydroxide and the 2Fe iron hydroxide surface models are assigned a charge of +1 in the calculation, the 4Fe surface will have a lower localized positive charge on each Fe atom. For example, when comparing the charge on

the Fe3 and Fe4, the middle atoms of the extended surface at +0.67 and +0.69 e^- respectively, they differ by about 10% to their analogous Fe1 and Fe2 atoms on the smaller iron oxyhydroxide surface at +0.73 and +0.76 e^- respectively (Table 4.4). To keep track of the change in the Mulliken charge as adsorption takes place and complexes transition from one into the other, Table 4.4 also lists the ΔMC (change in the Mulliken charge) that is obtained by subtracting the Mulliken charge of the atoms in the vacant iron oxyhydroxide by the Mulliken charge of the same atoms in the OS, MM and BB complexes.

The total sum of the Mulliken charges on the Fe atoms for the extended Fe4 surface changes from +1.48e^- to +0.33e^- to +0.06e^- and finally +0.16e^- when it transitions from the uncomplexed Fe4 surface to the OS(4Fe), MM(4Fe) and BB(4Fe) complexes respectively. Similarly, the total Mulliken charges on the O atoms change from -1.79e^- to -1.82e^- to -1.26e^- to -0.83e^-, when it moves from bulk DMA into the OS(4Fe), MM(4Fe) and BB(4Fe) complexes respectively. A similar ligand to metal charge transfer (LMCT) takes place for the 2Fe surface clusters where the sum of the Mulliken charges for Fe atoms changes from +1.49e^- to +1.13e^- to +1.22e^- to +1.18e^- as it transitions from the uncomplexed 2Fe surface to the OS(2Fe), MM(2Fe) and BB(2Fe) complexes respectively. Likewise, the total of the Mulliken charges on the O atoms changes from -1.79e^- to -1.82e^- to -1.56e^- to -1.26e^-, for the bulk DMA to the OS(2Fe), MM(2Fe) and BB(2Fe) complexes respectively. These changes in Mulliken charges show the redistribution of charge as adsorption takes place and transitions from OS to

MM to BB, as well as the role that electrostatic attraction might play in the formation of these complexes.

For both the 2Fe and 4Fe model surfaces, the Mulliken charges remain relatively constant for the O atoms on the DMA molecule in the transition from the bulk to the OS complex with only a small difference in the Mulliken charge (ΔMC) of -0.031e^- for OS(2Fe) and -0.034e^- for the OS(4Fe) complex. However, when the ΔMC of O atoms is analyzed as DMA transitions from OS to MM we see an increase in ΔMC = +0.229e^- for the MM(2Fe) and ΔMC = +0.524e^- when transitioning to the MM(4Fe) complex. This trend continues as the DMA transitions into a BB complex with an increase in the ΔMC = +0.525e^- when forming the BB(2Fe) complex and ΔMC = +0.956e^- when forming the BB(4Fe) complex. Likewise, the As atom becomes slightly more positively charged from +1.05e^- in the bulk to +1.19e^- for OS(2Fe) to +1.32e^- for MM(2Fe) to +1.22e^- for BB(2Fe). Likewise, As becomes slightly more positive as in transition from the bulk at +1.05e^- to +1.17e^- in OS(4Fe) to +1.20e^- for MM(4Fe) to +1.31e^- for BB(4Fe) complexes.

Overall, the Mulliken charge analysis shows that in the formation of the outer-sphere complexes there is very little charge transfer while the formation of the inner-sphere involves charge transfer. This suggests that the formation of the outer-sphere complex from the bulk is ionic in nature (i.e. purely electrostatic).

4.3.4 Spectroscopic Analysis of DMA Adsorption

Table 4.5 shows the calculated ν(As-O) for DMA and the OS, MM and BB complexes formed with iron oxyhydroxide model clusters with both two and four Fe centers. The table only shows medium and strong intensity ν(As-O) vibrations that have a bond length displacement greater than 0.3 Å. Bond length displacements below this limit were omitted. ATR-FTIR adsorption studies of DMA on hematite (Fe_2O_3) and goethite (FeOOH) have shown As-O stretching frequencies at 775, 793, 840, 877 cm^{-1} and 768, 787, 837 and 876 cm^{-1} for the DMA/hematite and the DMA/goethite complexes, respectively.[44] Table 4.5 displays raw data and does not correct for anharmonicity.

Table 4.5 Calculated ν(As−O) Frequencies (cm^{-1}) for DMA complexes with iron oxyhydroxide using B3LYP/6-311+G(d,p) with IEFPCM solvation and GD3BJ dispersion. The frequencies in brackets were calculated without dispersion for similar DMA/2Fe complexes.[38]

Complex	ν(As-O)	ν(As-OFe)
OS(2Fe) DMA	757, 803	
	(754, 800)	
OS(4Fe) DMA	789, 809	
MM(2Fe) DMA	782	758, 782
		(739, 792)
MM(4Fe) DMA	835	790, 795
BB(2Fe) DMA		764, 781, 799
		(764, 773, 788, 790)
BB(4Fe) DMA		738, 811

* No scaling factor was used to correct for anharmonicity.

Table 4.5 values show reasonable agreement with experimental values, with the 2Fe complexes having As-O stretching frequencies between 757 – 803 cm^{-1} and the 4Fe complexes having As-O stretching frequencies between 738 – 835 cm^{-1}. It was previously reported[84] that a scaling factor of 1.0307 might be appropriate for anharmonic corrections when As and Fe calculations are performed at the B3LYP/6-311+G(d,p) level of theory with the IEFPCM solvation model. However, this correction factor did not consider dispersion or the extended 4Fe surface when it was computed. Therefore a better approximation at this correction factor can be made when the extended 4Fe data is used and dispersion is accounted for. By minimizing the sum of squares of the residual between calculated and experimental data, a new scaling factor will be suggested further down in the thesis.

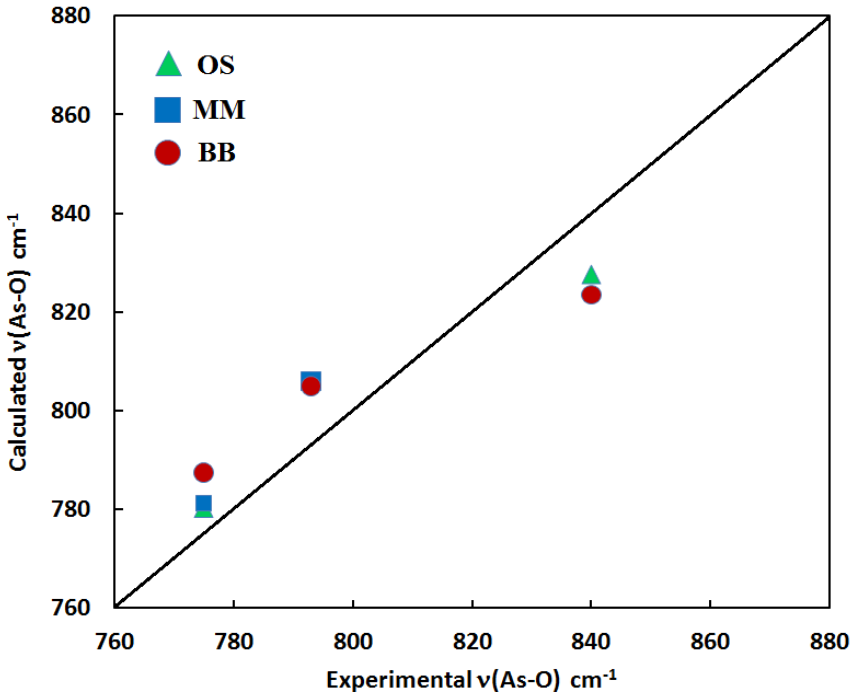

Figure 4.11 Correlation between calculated and experimental ν(As-O) frequencies for DMA on hematite for 2Fe complexes with anharmonic correction factor 1.0307.

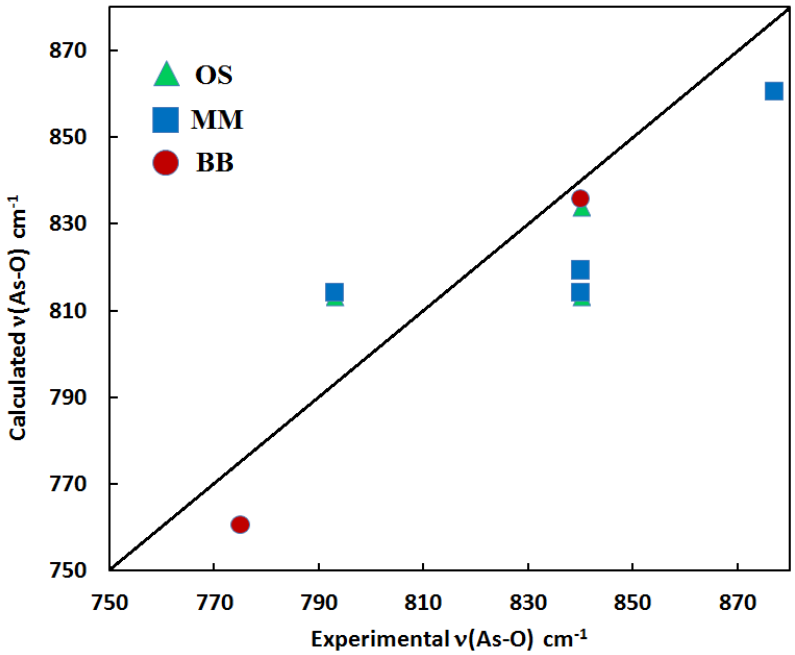

Figure 4.12 Correlation between calculated and experimental ν(As-O) frequencies for DMA on hematite for 4Fe complexes with anharmonic correction factor 1.0307.

Figures 4.11 and 4.12 show the correlation between the calculated and experimental frequencies for the 2Fe and 4Fe complexes respectively. A different way to view this correlation is illustrated in Figures 4.13, which shows the theoretical frequencies from the 2Fe complexes (left) and 4Fe complexes (right) overlapping experimental infrared spectra taken from Reference 32.

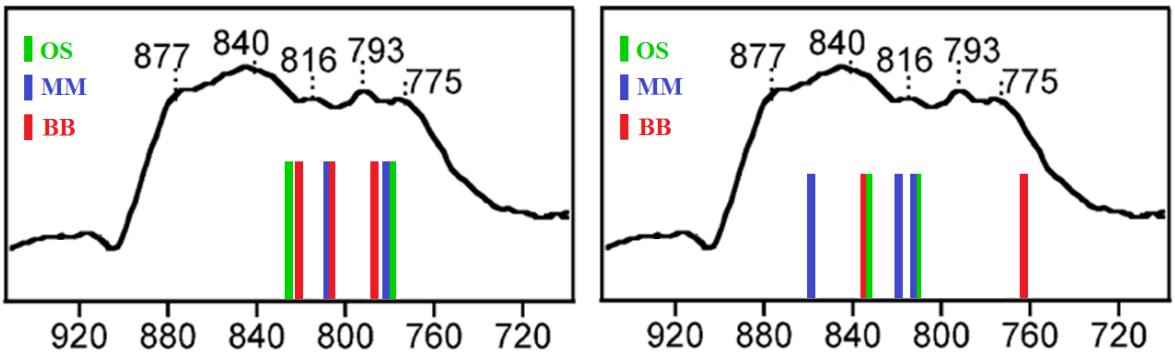

Figure 4.13 The correlation between theoretical and experimental data overlapped. The 2Fe complexes are shown on the left and the 4Fe complexes on the right.

4.4 Conclusions

The calculations in this chapter show that the formation of inner- and outer-sphere DMA-iron oxide complexes are thermodynamically favourable, but that the activation barrier for bidentate formation from monodentate is significantly higher than the activation barrier from outer-sphere to monodentate, which is not the case for the arsenate system. Extending the modelled surface to include 4 Fe centers produces geometries for DMA complexes that do not over-relax and are in better agreement with experimental bond distances. It is shown that an extended surface is particularly important for outer-sphere complexes, but that there is very little difference in the bidentate complex when modeling with 2 or 4 Fe centres model surfaces. Therefore, extending the surface to 4 Fe atoms could be valuable when studying outer-sphere complexes or larger molecules that tend to wrap around a smaller surface when performing energy optimizations.

The Mulliken charge distribution analysis revealed how electrostatic attraction plays a role in the formation of OS complexes and how charge is transferred from the ligand to the metal as inner sphere complexes form. Theoretical IR spectra were also compared with experimental studies to gain more insight into how adsorption takes place at a molecular level and aid in the interpretation of infrared spectra and peak assignment. It was shown, from the frequency calculations, that using a 3% adjustment to correct for anharmonic behaviour is adequate for arsenic complexes with iron

oxyhydroxides, but this correction factor may need adjustment to include dispersion models and the extended 4Fe surface.

CHAPTER V. Sorption of Monomethylarsonic Acid onto Hydrated Iron (III) Oxyhyhroxide Clusters

5.1 Overview

Monomethylarsonic acid is an important arsenic pollutant that was used historically as a herbicide on large agricultural fields and as a pesticide, in particular in the fight against the mountain pine beetle that has devastated forests in British Columbia. Once introduced into the environment, MMA can enter the food chain or be recycled to more mobile forms of arsenic that can contaminate nearby water sources. Density functional theory calculations can provide a better understanding of what happens to pollutants such as MMA at a molecular level when they enter the environment and interact with reactive components in the soil, such as iron oxyhydroxides. Energies, optimal geometries and vibrational frequencies for hydrated MMA complexes with iron oxyhydroxide clusters are computed and theoretical ligand exchange reactions are constructed to investigate the thermodynamics of inner- and outer-sphere complex formation. The Gibbs free energies and enthalpies of adsorption show that both inner- and outer-sphere complex formation is thermodynamically favourable with monodentate complexes being most favourable. Comparisons are made between the MMA, DMA and pAsA systems and it is shown that the MMA molecule behaves more like the mono-substituted pAsA rather than DMA when it adsorbs to iron oxyhydroxides.

The calculated As-Fe inter-atomic distances for MMA complexes are shown to be between 3.23 – 3.55 Å for inner-sphere complexes and between 5.17 – 5.23 Å for outer-sphere complexes. The theoretical infrared spectral data is compared to experiment and it is shown that the broad peaks observed experimentally in the range between 770 − 880 cm^{-1} could arise from monodentate and bidentate complexes of MMA with iron oxyhydroxides.

5.2 Introduction

Bio-methylation of inorganic arsenic by organisms that live in the soil and sediments is quite prevalent in the environment leading to the production of a variety of methylated arsenicals, like MMA, DMA or TMA, as explained by the Challenger mechanism presented earlier in Figure 1.1. Historically MMA, DMA and their sodium salts were also the most common ingredients used in pesticides and herbicides, but have been banned in many western countries because of their potential negative effects on the environment and human health.[10]

In Canada, MMA has been widely used in British Columbia to help suppress outbreaks of the Mountain pine beetle in the 1990s, but has since been retracted because of its potential negative effects. Blood samples from woodpeckers and other birds that feed on Mountain pine beetles from contaminated MMA trees showed an elevated level of total arsenic.[107, 108] Hence, the accumulation and transfer of organic arsenic within the food chain could be toxic to other wildlife and avian species in particular. The proposed metabolic pathway of MMA in birds is shown in Figure 5.1 below, with the excreted product being DMA.

The nature of MMA and DMA surface complexes formed varies depending on which metal oxide surface they interact with. On amorphous aluminum oxides (AAO), MMA and DMA was reported to form BB complexes when studied by FTIR spectroscopy and extended EXAFS techniques[109] but that was not observed with iron oxides, where MMA was observed to be mostly monodentate[110] and DMA was observed

to be more monodentate and outer-sphere.[111] The presence of extra methyl groups seems to affect the adsorption rate.[112]

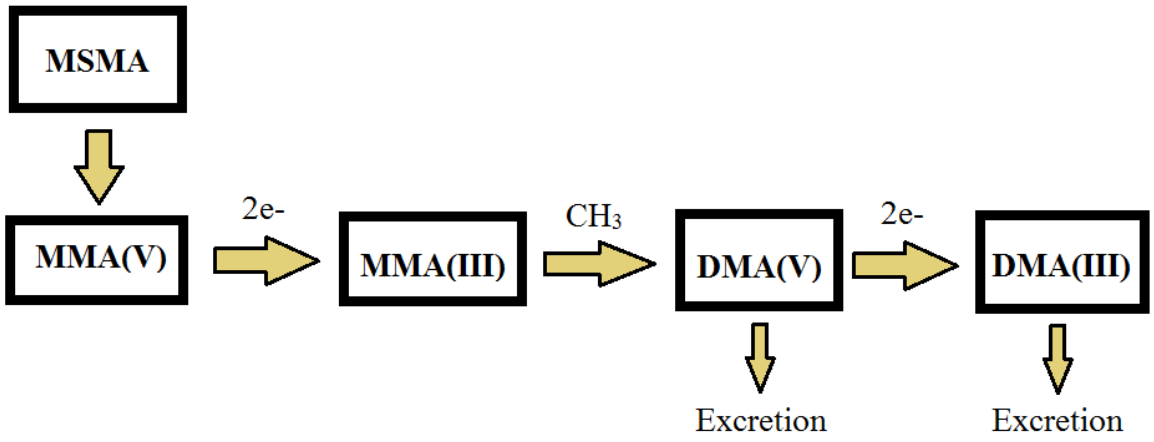

Figure 5.1 A proposed metabolic pathway for monosodium methanearsonate (MSMA) after ingestion and uptake. MMA naturally ionizes and is associated with sodium to form the sodium salt, MSMA. If MSMA is ingested by an animal, the high acidity of the stomach causes the hydrolization to MMA. After uptake, metabolism of the compound proceeds to dimethylarsinic acid (DMA) until excreted.
Reproduced from Reference 108 (Morrissery and Elliott, 2011)

In this chapter, the objective is to look at the optimized geometries of MMA in the bulk and MMA bound to iron oxyhydroxide clusters in a hydrated environment to study binding mechanisms. The extended iron oxyhydroxide surface, with 4 core Fe atoms, will be used to study the adsorption process since it more realistically simulates a surface, as concluded in the previous chapter. The theoretical infrared spectra were analyzed and calculated Gibbs free energies, enthalpies and entropies of adsorption for various types of ligand exchange reactions will be calculated.

5.3 Results and Discussion

5.3.1 MMA complexation with iron oxyhydroxides

The optimized geometry of the negatively charged species of hydrated MMA in the bulk is shown in comparison with the mono-substituted arsenical pAsA in Figure 5.2 below. Both arsenicals have very similar geometries with d(As-C) = 1.92 and 1.93 Å for pAsA and MMA respectively. The d(As-O) distances are all 1.69 Å for both arsenicals while the d(As-OH) differs slightly at 1.79 Å for MMA and 1.81 Å for pAsA.

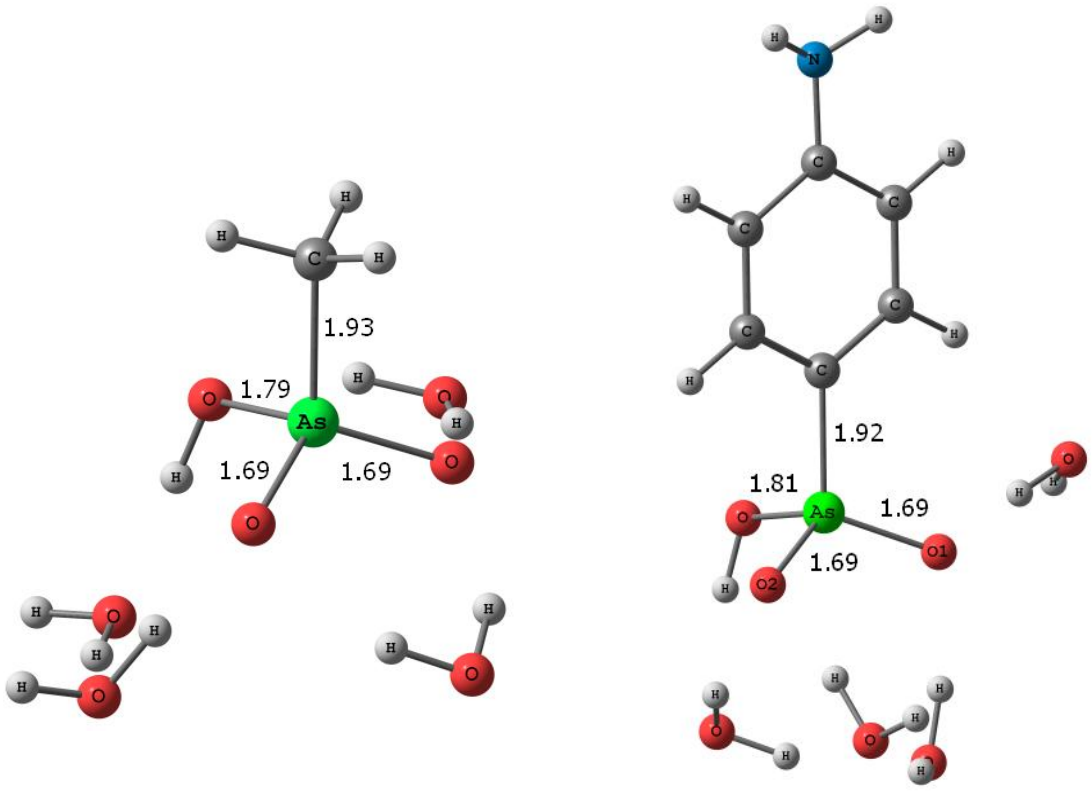

$MMA^- \cdot (H_2O)_4$ $pAsA^- \cdot (H_2O)_4$

Figure 5.2 Energy minimized structures of MMA and pAsA with surrounding explicit waters. Calculated using B3LYP/6-311+G(d,p) with IEFPCM and GD3BJ dispersion.

The adsorption of a negatively charged MMA molecule onto the positively charged iron oxyhydroxides surface will produces the three different types of OS, MM and BB complexes shown in Figure 5.3. The OS(4Fe) MMA complex is held in place through hydrogen bonds and has inter-atomic distances, d(As–Fe) equalling 5.23 and 5.75 Å. The MMA in the OS complex interacts with 3 core Fe atoms as illustrated in Figure 5.3, with the third d(As–Fe) at 5.17 Å. The As atom is slightly closer to that third Fe atom, but only because it is not an octahedral Fe. The inner-sphere MM and BB complexes are formed after ligand exchange and formation of covalent bonds with the Fe atoms in the extended iron oxyhydroxide surface. The inter-atomic distances d(As–Fe) for the MM(4Fe) complex are 3.55 and 4.92 Å, while for the BB(4Fe) complex they are 3.23 and 3.47 Å. The predicted geometries of the OS, MM and BB MMA complexes are shown in Table 5.1 below.

For comparison, Figure D1 in Appendix D also shows the MM(4Fe) complex of MMA optimized without dispersion having inter-atomic As-Fe distances of 3.60 and 5.01Å, amounting to only a 2% difference between the MM(4Fe) complex with and without the dispersion corrections (see Table 5.1). These results further strengthen the argument that even for the extended surfaces, dispersion corrections do not affect inner sphere complexes as much and they might only be necessary when dealing with outer-sphere complexes.

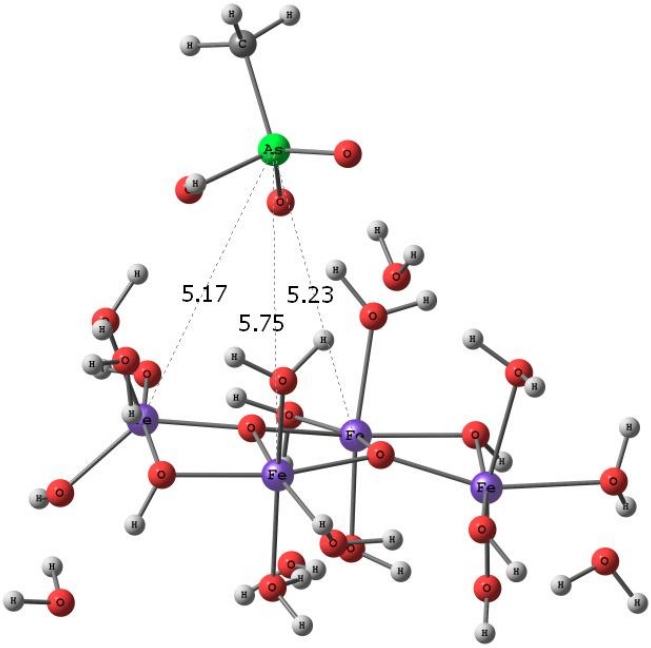

OS(4Fe) MMA

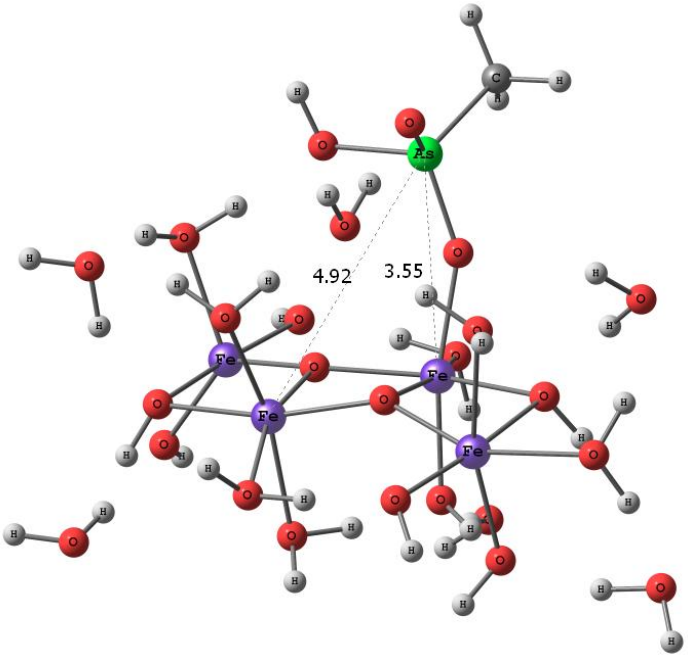

MM(4Fe) MMA

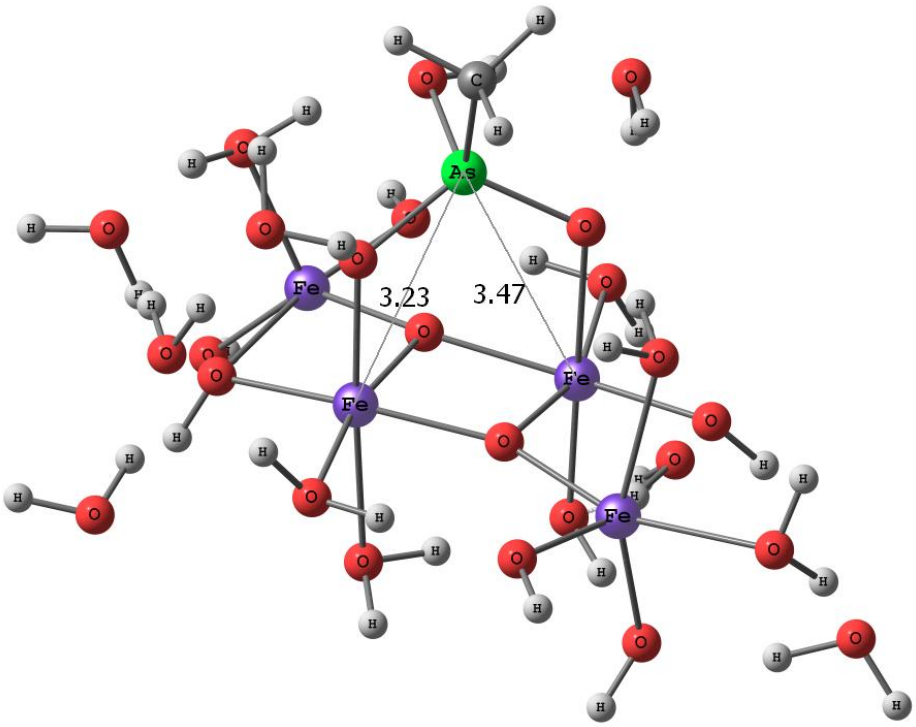

BB(4Fe) MMA

Figure 5.3 Optimized MMA Complexes with B3LYP/6-311+G(d,p) IEFPCM and GD3BJ dispersion

Table 5.1 Predicted As-O, Fe-O bond distances (Å) and As-Fe inter-atomic distances (Å) of OS, MM and BB complexes of MMA with the extended iron oxyhydroxides surface. Calculated using B3LYP/6-311+G(d,p) with IEFPCM solvation and GD3BJ dispersion models.

MMA complexes	**As-Fe_1**	**As-Fe_2**	**As-O_1**	**As-O_2**	**As-C**	**As-OH**	**Fe_1-O_1**	**Fe_2-O_2**
MMA (bulk)	-	-	1.69	1.69	1.93	1.79	-	-
OS(4Fe) MMA complex	5.23	5.75	1.67	1.67	1.93	1.83	-	-
MM(4Fe) MMA complex	4.92	3.55	1.67	1.67	1.92	1.82	-	1.98
MM(4Fe) without dispersion	5.01	3.60	1.67	1.68	1.93	1.83	-	2.00
BB(4Fe) MMA complex	3.23	3.47	1.69	1.70	1.92	1.79	2.03	2.37

When the MMA complexes are compared to the DMA complexes (see Table 4.1) and pAsA complexes (see Table 3.8) it is apparent that MMA has more in common with pAsA with similar inter-atomic distances for the OS, MM and BB complexes. This similarity is explained by their common geometry, both being mono-substituted arsenicals and having an OH group bonded to the arsenic.

5.3.2 MMA adsorption Thermodynamics

The calculated electronic energies (E_0), the electronic energies with the thermal corrections to enthalpies ($E_0 + H_{corr}$) and Gibbs free energies ($E_0 + G_{corr}$) for the reactants and products needed in the adsorption reactions of MMA^- with Fe4 clusters are shown in Table 5.2 below. The ΔH_{ads}, ΔG_{ads} and ΔS_{ads} for various reactions leading to the OS, MM and BB complexes of MMA with iron oxyhydroxide are shown in Table 5.3 below.

Table 5.2 Electronic Energies (E_0), Electronic Energies with Thermal Corrections to Enthalpy ($E_0 + H_{corr}$) and Electronic Energies with Thermal Corrections to Gibbs Free Energy ($E_0 + G_{corr}$) for MMA complexes with the extended iron oxyhydroxide surface. Calculated using B3LYP/6-311+ G(d,p) with IEFPCM solvation and GD3BJ dispersion.

Reactants	**(E_0)**	**($E_0 + H_{corr}$)**	**($E_0 + G_{corr}$)**
$MMA^- \cdot (H_2O)_4$	-2808.25945	-2808.08550	-2808.15308
$[Fe_4O_2(OH)_7(OH_2)_8]^+ \cdot (H_2O)_5$	-6730.89335	-6730.40782	-6730.54111
4Fe MMA complexes			
OS(4Fe) $MMA \cdot (H_2O)_5\ Fe_4O_2(OH)_7(OH_2)_8$	-9233.26872	-9232.71923	-9232.87276
MM(4Fe) $MMA\text{-}Fe_4O_2(OH)_7(OH_2)_7 \cdot (H_2O)_6$	-9233.28004	-9232.72897	-9232.87972
BB(4Fe) $MMA\ Fe_4O_2(OH)_7(OH_2)_6 \cdot (H_2O)_7$	-9233.27602	-9232.72350	-9232.87613
Leaving Water Cluster			
$(H_2O)_4$	-305.90291	-305.79462	-305.83868

As seen from Table 5.3, the trend in the values of ΔG_{ads} show that the formation of the MM(4Fe) complex is the most thermodynamically favourable, followed by BB(4Fe) and OS(4Fe). The ΔG_{ads} values are -63.6, -54.1 and -45.3 kJ/mol for MM(4Fe), BB(4Fe) and OS(4Fe) respectively. The formation of the MM(4Fe) complex for MMA is more thermodynamically favourable (ΔG_{ads} = -63.6 kJ/mol) than the equivalent MM(4Fe) complex for DMA with a ΔG_{ads} = -59.6 kJ/mol, while the formation of the OS(4Fe) and BB(4Fe) complexes of MMA are less thermodynamically favourable than their DMA equivalents.

Table 5.3 Values of ΔH_{ads}, ΔG_{ads} and ΔS_{ads} for reactions of MMA with iron oxyhydroxide clusters. Calculated using B3LYP/6-311+G(d,p) with IEFPCM solvation and GD3BJ dispersion.

MMA adsorption onto 4Fe surface $MMA^- \cdot (H_2O)_4 + [Fe_4O_2(OH)_7(OH_2)_8]^+ \cdot (H_2O)_5 \rightarrow$	**ΔH_{ads} (kJ mol^{-1})**	**ΔG_{ads} (kJ mol^{-1})**	**ΔS_{ads} (kJ mol^{-1}K^{-1})**
OS(4Fe) $MMA \cdot (H_2O)_5\ Fe_4O_2(OH)_7(OH_2)_8$	-53.9	-45.3	-0.0289
MM(4Fe) $MMA\text{-}Fe_4O_2(OH)_7(OH_2)_7 \cdot (H_2O)_6$	-79.5	-63.6	-0.0534
BB(4Fe) $MMA\text{-}Fe_4O_2(OH)_7(OH_2)_6 \cdot (H_2O)_7$	-65.1	-54.1	-0.0368

Figure 5.4 shows the $\Delta\Delta G_{ads}$ for the OS(4Fe), MM(4Fe) and BB(4Fe) complexes of MMA relative to the MM complex. The MM(4Fe) is the most thermodynamically favourable complex, followed by the BB(4Fe) and then by the OS(4Fe) complexes. Even though MMA has a methyl group it does not act like DMA (with 2 methyl groups) when it comes to complex formation, but it is rather more similar to pAsA complexation (see Figure 3.7) where the MM complex is the most thermodynamically favourable. The stability of MM complexes could be due to the fact that both pAsA and MMA are mono-substituted arsenicals which have more rotational freedom to find a lower energy configuration, with further stability being achieved when the oxygen atoms and hydroxyl groups form hydrogen bonds with the iron oxide surface. In comparison, the DMA molecule will not achieve the most thermodynamically favourable position in the monodentate configuration with its bulky methyl groups sticking out to the side, but rather in the bidentate configuration with its methyl groups sticking upward.

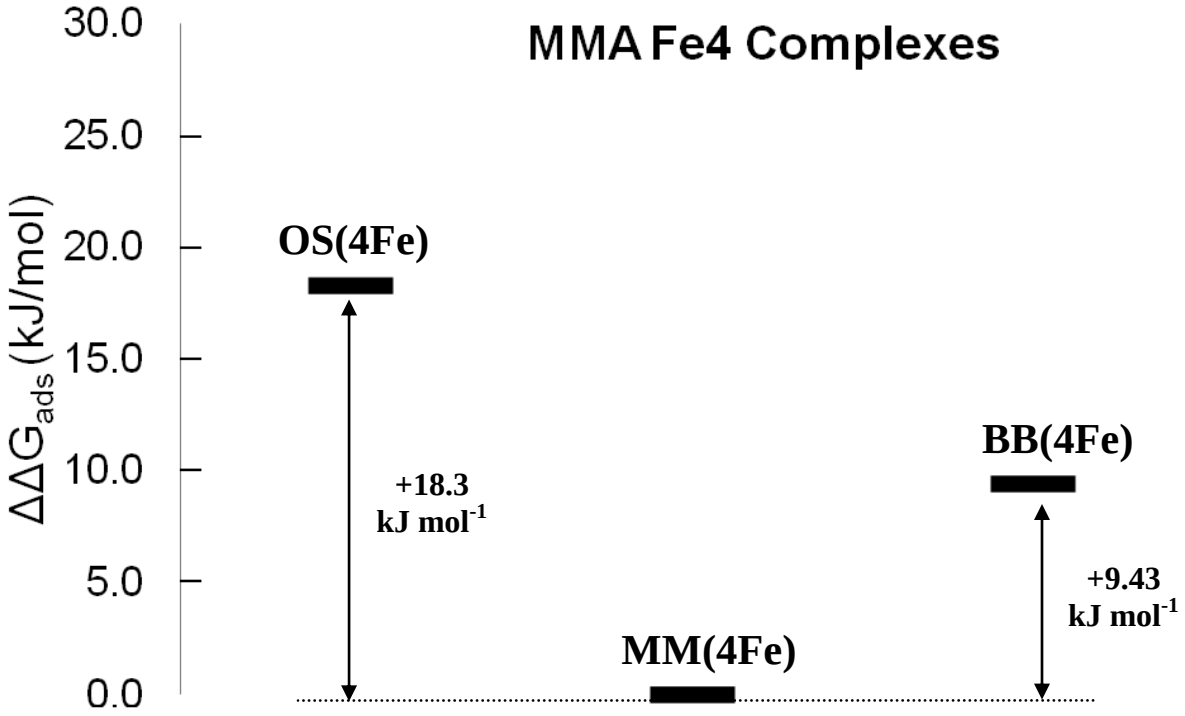

Figure 5.4. Differences in the Gibbs free energies ($\Delta\Delta G_{ads}$) for MMA/(4Fe) iron oxyhydroxide clusters relative to MM(4Fe). Calculated using the reactions listed in Table 5.3.

5.3.3 Spectroscopic Analysis of MMA adsorption

Table 5.4 shows the calculated ν(As-O) of medium and strong intensity with a bond length displacement greater than 0.3 Å for the OS(4Fe), MM(4Fe) and BB(4Fe) complexes of MMA with iron oxyhydroxide model clusters. ATR-FTIR adsorption studies of MMA on hematite (Fe_2O_3) nanoparticles have shown a broad absorption in the range of 770 and 880 cm^{-1} with the most pronounced features around 793, 840 and 877 cm^{-1}.[112] ATR-FTIR spectral analysis of MMA adsorbed onto hematite suggests that MMA forms mostly monodentate and some bidentate complexes.[105] The stretching frequencies in Table 5.4 are in good agreement with these experimental values even

without correction for anharmonicity, showing that As-O stretching frequencies range between 757 – 876 cm^{-1}. The features at 757 and 791 cm^{-1} stem from ν(As−OFe) in the bidentate complex, the 855 cm^{-1} feature stems from the ν(As−O) in the monodentate complex, while the higher wavenumbers at 862 and 876 cm^{-1} are from the formation of monodentate and bidentate respectively. These theoretical calculations give further evidence that the broad absorption in the range 770 − 880 cm^{-1} seen experimentally stems from both monodentate and bidentate complexes of MMA with iron oxides.

Table 5.4 Calculated ν(As−O)* Frequencies (cm^{-1}) for MMA complexes with iron oxyhydroxide using B3LYP/6-311+G(d,p) with IEFPCM solvation and GD3BJ dispersion.

MMA Complexes	**ν(As-O)**	**ν(As-OH)**	**ν(As-OFe)**
OS(4Fe) MMA	835, 854	573	
MM(4Fe) MMA	855	588	876
BB(4Fe) MMA		636	757, 791, 862

* No scaling factor was used to correct for anharmonicity.

Using the previously calculated 1.0307 scaling factor mentioned earlier would increase the calculated frequencies in Table 5.4 to the 780 – 903 cm^{-1} range for the 4Fe MMA complexes which is outside of the range of experimentally observed frequencies. This result suggests that the scaling factors previously used will need to be updated to include dispersion effects and the effects of an extended surface. The un-scaled frequencies in this case have a good correlation with experimental values as seen in Figure 5.5 below.

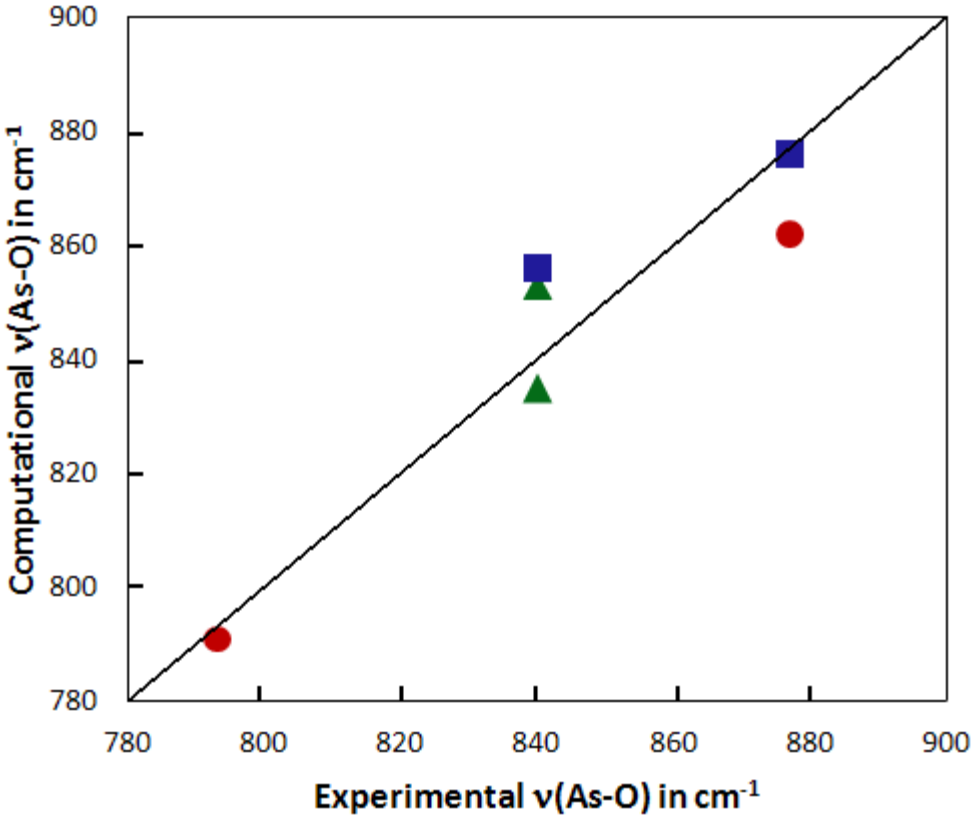

Figure 5.5 Correlation between calculated and experimental ν(As-O) frequencies for MMA on hematite without correction factors. The calculated MMA complexes are shown as follows: OS(4Fe) = green triangles, MM(4Fe) = blue squares and BB(4Fe) = red circles.

5.4 Conclusions

The DFT calculations in this chapter show that MMA follows a similar trend as pAsA and that the formation of inner- and outer-sphere complexes with iron oxyhydroxide is thermodynamically favourable, with the formation of the MM complex being the most favourable, followed by the bidentate and the outer-sphere complex, MM > BB > OS. The MMA system is considerably different than the DMA system where the BB complex is the most thermodynamically favourable.

Theoretical frequency calculations confirm that the spectral components could arise from both monodentate and bidentate surface complexes of MMA with iron oxyhydroxide. However, when combining the thermodynamics calculations with the spectral data, it is most likely that the major contribution comes from monodentate MMA complexes. Transition state calculations were not performed for 4Fe MMA complexes because of the complexity of having an extended surface and the restrictions of computational time. Nevertheless, assuming that MMA would have a similar high activation barrier as the DMA and pAsA complexes with 2Fe, the transition from monodentate to bidentate would further inhibit the formation of the bidentate complex.

CHAPTER VI. Conclusions and Significance

DFT calculations show that the formation of inner- and outer-sphere complexes with the three organoarsenicals studied, pAsA, MMA and DMA are thermodynamically favourable, but also that the activation barriers are important in determining whether OS, MM or BB complexes will form experimentally. It was shown that the mono-substituted arsenicals pAsA and MMA have more in common with each other than with DMA. For both pAsA and MMA, the trend in thermodynamic favourability is MM > BB > OS while for DMA it is BB > MM > OS. However, it is also argued that since the activation barrier for transition of DMA from MM to BB is also higher (twice as high as the one for pAsA and almost 4 times higher than arsenate), the formation of a BB complex is less likely for DMA, even if it is thermodynamically more favourable.

The calculations reported herein also include dispersion corrections, using the GD3BJ dispersion model, which previous theoretical studies of arsenicals on metal oxide clusters have not reported. It was shown that dispersion corrected DFT calculations affect the geometries of arsenical complexes with weaker interaction between adsorbate and substrate, such as the OS complexes, but that the geometries of MM and BB complexes are less affected by dispersion corrections.

Using an extended 4Fe iron oxyhydroxide surface with the MMA and DMA calculations also produced geometries that do not over-relax and are in good agreement with experimental bond distances. These 4Fe geometries were shown to be especially

useful for OS and MM complexes, where over-relaxation is a greater problem, but were not an issue with the BB complexes, since these geometries are held in place by two strong covalent bonds.

The Mulliken charge distribution analysis revealed how electrostatic attraction may play a role in the formation of DMA complexes and how the charge is redistributed as the DMA transitions from OS to MM to BB. Since there was little change in the Mulliken charges of atoms when the OS complexes formed the interaction between DMA and the surface is purely ionic. On the other hand, there was significant change in the Mulliken charges when the MM and BB complexes formed as the charge transferred from the ligand to the metal.

Comparing theoretical IR spectra with experimental work also provides additional insight into how adsorption takes place at the molecular level and aids in the interpretation of infrared spectra and the assignment of peaks. The theoretically calculated spectral features correlated well with experiments. However, the frequency calculations were adjusted with a scaling factor of 1.0307 to correct for anharmonicity, which was adequate for some calculations with iron oxides and arsenic complexes with the B3LYP/6-311+G(d,p) and the IEFPCM solvation model, but didn't take into account an extended surface, dispersion corrections and data from more arsenical complexes.

This scaling factor can be revised by minimizing M, the sum of squares of the residuals between the theoretical and experimental As-O stretching frequencies shown

in Equation 3.1 below. The method is an adaption of a similar one used by Merrick, Moran and Radom[113] but only considers the As-O stretching vibration of interest in calculations with arsenicals:

$$M = \min \sum R_i^{\,2} \qquad \text{(Equation 6.1)}$$

where R_i are the residual functions comprised of the differences between the scaled theoretical values of the ν(As-O) and the experimental ν (As-O), as shown in Equation 3.2 below:

$$R_i(F) = T_iF - E_i \qquad \text{(Equation 6.2)}$$

where T_i are the theoretically calculated ν(As-O) values and E_i are their corresponding experimental ones. The data for the calculations of a new scaling factor F that minimizes the Residual in shown in Table D1 in Appendix D. Thus it is recommended that a proper scaling factor to use to correct for anharmonicity for calculations with arsenicals and iron oxyhydroxides is F=1.0065. Although correcting for anharmonicity usually lowers the calculated harmonic frequency Merrick, Moran and Radom[113] have found that for lower frequencies this is often the reverse. In particular for the B3LYP functional their study suggests using a scaling factor of 1.0189 for lower frequencies. The 1.0065 correction factor calculated in this thesis is close (within 1.2%) to the one calculated by Merrick, Moran and Radom, but is specific for arsenicals and iron complexes that take into account solvation and dispersion effects.

The results presented in this thesis also have practical applications in the areas of soil remediation, water filtration and provide data for models that are designed to predict the fate of pollutants. By taking into account the arsenic species as a factor in the modeling and design process of remediation technologies, more efficient arsenic removal could be achieved. As an example, this thesis has shown that DMA has much higher activation barriers to overcome to form inner-sphere complexes with iron oxyhydroxides, thus making it more mobile than other arsenical species in iron rich soil. Conversely, once bidentate DMA complexes form they are more stable and thus DMA could become less mobile over time. Remediation efforts might benefit from knowing more precise time frames for the formation of these inner-sphere complexes. Experiments could be designed to address this question and offer a time frame for how long it would take DMA to form the more strongly bound inner-sphere complexes. One such experiment could be as simple as incubating a mixture of DMA with an iron oxide for various amounts of time and then testing how well a desorbing agent can remove the adsorbed arsenical. Alternatively, the activation barriers that were calculated in this thesis can be used to predict reaction rate constants. Calculating $\Delta G^{\ddagger}$, the difference in Gibbs free energy between the transition state and the reactants, can be used to find the reaction rate constant, k, using Equation 6.3 below[114]:

$$k = \frac{k_B T}{hc^{\circ}} e^{-\Delta G^{\ddagger} / RT} \qquad \text{(Equation 6.3)}$$

where k_B is Boltzmann's constant, h is Planck's constant, c^o is the standard state concentration, R is the molar gas constant and T is the temperature in degrees Kelvin.

For future directions, the work presented in this thesis could benefit from further investigations of organoarsenicals interacting with different kinds of environmentally relevant materials. Soil is a complex mixture of minerals, organic compounds and liquids and there are many materials to investigate, in particular interactions of organoarsenicals with other metal oxides, such as aluminum and manganese oxides. Another interesting idea to investigate is the effects of organic matter on the sorption of organoarsenicals. How would the presence of organics change the thermodynamics of adsorption and the activation barriers? Also, the calculations in this thesis used pure water to simulate hydration, but in the environment there are a lot of salts dissolved in water. Changing the value of the dielectric medium could be an easy way to simulate different type of environments without adding any additional molecules and keeping the computational costs relatively low. Simulating other dissolved charges when performing these calculations could have varying effects on the sorption of organoarsenicals, since the reactions are driven by electrostatics. Lastly, the work in this thesis was done on static molecules for the most energetically favourable situations. To observe what is really going on at the molecular level DFT molecular dynamics (DFT-MD) calculations would be an important next step. DFT-MD calculations would allow us to visualize the movements of the organoarsenicals as they interact with the metal oxide surfaces and give us a clearer picture of how the system evolves over time.

References

[1] Agency for Toxic Substances and Disease Registry (ATSDR). 2007. Public Health Statement – Arsenic. https://www.atsdr.cdc.gov/ToxProfiles/tp2-c1-b.pdf

[2] Huang, Y. C. In Arsenic in the environment, part I: Cycling and characterization; Nriagu, J. O., Ed.; Wiley-Interscience: NewYork, 1988.

[3] Mandal, B.K; Suzuki, K.T. Arsenic round the world: a review. Talanta, 58 (2002), 201-235.

[4] Bentley, R.; Chasteen, T.G. Microbial methylation of metalloids: arsenic, antimony, and bismuth. Microbiol. Molecular Biology Rev. 66 (2002), 250-271.

[5] Challenger, F. Biological methylation. Chem. Rev. 36 (1945), 315−361.

[6] Fendorf, S.; Nico, P.S.; Kocar, B.D.; Masue, Y.; Tufano, K.J. Chapter 12 – Arsenic Chemistry in Soils and Sediments. Developments in Soil Science, 34, (2010), 357-378.

[7] Brookins, D.G. Eh-pH Diagrams for Geochemistry. 1988. Springer-Verlag, Berlin.

[8] Smedley, P.L; Kinniburgh, D.G. A review of the source, behaviour and distribution of arsenic in natural waters. Applied Geochem. 17 (2002), 517-568.

[9] Ponthieu, M.; Pinel-Raffaitin, P.; Le Hecho, I.; Mazeas, L.; Amouroux, D.; Donard, O.; Pontin-Gautier, M. Speciation analysis of arsenic in landfill leachate. Water Res. 2007, 41, 3177–3185.

[10] MacLatchy, J., Metals Data from Base Metal Smelters and Refineries. Environment Canada, Industrial Programs Branch, Ottawa, 1992.

[11] Cullen, W.R., Is Arsenic an Aphrodisiac? The Sociochemistry of an Element, RBC Publishing, Cambridge, 2008.

[12] US FDA, 2015, Questions and Answers Regarding 3-Nitro (Roxarsone), http://www.fda.gov/AnimalVeterinary/SafetyHealth/ProductSafetyInformation/ucm258313.htm

[13] Garbarino, J.R .; Bednar, A.J.; Rutherford, D.W; Beyer, R.S., Wershaw, R.L., Environmental fate of roxarsone in poultry litter. I. degradation of roxarsone during composting. Environ. Sci. Technol. 2003, 37, 1509-1514.

[14] Jackson, B.P.; Seaman, J.C.; Bertsch, P.M., Fate of arsenic compounds in poultry litter upon land application. Chemosphere 2006, 65, 2028-2034.

[15] Brown, B.L.; Slaughter, A.D.; Schreiber, M.E., Controls on roxarsone transport in agricultural watersheds. Applied Geochem. 2005, 20, 123-133.

[16] Nuallain, C.O.; Cinneide, S.O., Thermodynamic ionization constants of aromatic arsonic acids. J. Inorg. Nucl. Chem., 1973, 35, 2871-2881.

[17] Wu, J.; Ho, P.C., Speciation of inorganic and methylated arsenic compounds by capillary zone electrophoresis with indirect UV detection application to the analysis of alkali extracts of As_2S_2 (realgar) and As_2S_3 (orpiment). J. of Chromatography A, (2004), 1026, 261-270.

[18] US EPA, 2011, Arsenic in Drinking Water, http://water.epa.gov/lawsregs/rulesregs/sdwa/arsenic/index.cfm

[19] Abhyankar, L. N.; Jones, M. R.; Guallar, E.; Navas-Acien, A. Arsenic Exposure and Hypertension: A Systematic Review. Environ. Health Perspect. 2012, 120, 494−500.

[20] Hirano, S.; Kobayashi Y.; Cui, X.; Kanno, S.; Hayakawa T.; Shraim, A. The accumulation and toxicity of methylated arsenicals in endothelial cells: important roles of thiol compounds, Toxicol. Appl. Pharmacol. 198 (2004), pp. 458–467.

[21] World Health Organization. Water-related diseases. Arsenicosis, 2001, [online] Available from http://who.int/water_sanitation_health/diseases/arsenicosis/en/

[22] Wickramasinghe, S. R.; Han, B.; Zimbron, J.; Shen, Z.; Karim, M. N. Arsenic Removal by Coagulation and Filtration: Comparison of Groundwaters from the United States and Bangladesh, Desalination, 169(3), 231-244 (2004).

[23] Dhuldhaj, U.P.; Yadav, I.C.; Singh, S.; Sharma, N.K. Microbial interactions in the arsenic cycle: Adoptive strategies and applications in environmental management. *Rev. Environ. Contam. Toxicol.* 2013, *224*, 1–38.

[24] Ali, I.; Khan, T.A.; Asim, M. Removal of arsenic from water by electrocoagulation and electrodialysis techniques. *Sep. Purif. Rev.* 2011, *40*, 25–42.

[25] Salameh, Y.; Al-Lagtah, N.; Ahmad, M.N.M.; Allen, S.J.; Walker, G.M. Kinetic and thermodynamic investigations on arsenic adsorption onto dolomitic sorbents. *Chem. Eng. J.* 2010, *160*, 440–446.

[26] Chutia, P.; Kato, S.; Kojima, T.; Satokawa, S. Arsenic adsorption from aqueous solution on synthetic zeolites. *J. Hazard. Mater.* 2009, *162*, 440–447.

[27] Liu, G.; Talley, J.W.; Na, C.; Larson, S.L.; Wolfe, L.G. Copper Doping Improves Hydroxyapatite Sorption for Arsenate in Simulated Groundwaters. *Environ. Sci. Technol.*, 2010, *44* (4), 1366–1372.

[28] Aredes, S.; Klein, B.; Pawlik, M. The removal of arsenic from water using natural iron oxide minerals. *Journal of Cleaner Production, 60, 2013, 71-76.*

[29] Aredes, S.; Klein, B.; Pawlik, M. The removal of arsenic from water using natural iron oxide minerals. *Journal of Cleaner Production, 60, 2013, 71-76.*

[30] PerkinElmer Technical Note. FT- IR Spectroscopy – Attenuated Total Reflectance (ATR) [online]. Available from http://shop.perkinelmer.com/content/TechnicalInfo/TCH_FTIRATR.pdf. 2005.

[31] Cowen, S.; Duggal, M.; Hoang, T.; Al-Abadleh, H.A. Vibrational Spectroscopic Characterization of Some Environmentally-Important Organoarsenicals: A Guide for Understanding the Nature of their Surface Complexes. Canadian Journal of Chemistry, 2008, 86(10), 942-950.

[32] Adamescu, A.; Mitchell, W.; Hamilton, I. P.; Al-Abadleh, H. A. Insights into the Surface Complexation of Dimethylarsinic Acid on Iron (Oxyhydr)oxides from ATR-FTIR Studies and Quantum Chemical Calculations. Environ. Sci. Technol. 2010, 44, 7802−7807.

[33] Grunwaldt, J.D.; Baiker, A. In situ spectroscopic investigation or heterogeneous catalysts and reaction media at high pressure. Phys. Chem. Chem. Phys., 2005,7, 3526-3539

[34] Sparks, D. L. Environmental Soil Chemistry, 1st ed.; Academic Press: San Diego, 1995.

[35] Luengo, C.; Brigante, M.; Antelo, J.; Avena, M. Kinetics of Phosphate Adsorption of Goethite: Comparing Batch Adsorption and ATR-IR Measurements. J. Colloid Interface Sci. 2006, 300, 511−518.

[36] Arai, Y.; Sparks, D. L. ATR-FTIR Spectroscopic Investigation on Phosphate Adsorption Mechanisms at the Ferrihydrite-Water Interface. J. Colloid Interface Sci. 2001, 241, 317−326.

[37] Tejedor-Tejedor, M. I.; Anderson, M. A. Protonation of Phosphate on the Surface of Goethite as Studied by CIR-FTIR and Electrophoretic Mobility. Langmuir 1990, 6, 602−611.

[38] Loring, J.S.; Sandtröm, M.H.; Norén, K.; Persson, P., Rethinking Arsenate coordination at the surface of goethite. Chem. Eur. J., 15 (2009) 5063-5072.

[39] Catalano, J.G.; Park, C.; Fenter, P.; Zhang, Z.; Simultaneous inner- and outer-sphere arsenate adsorption on corundum and hematite. Geochim. Cosmochim. Acta. 2008, 59: 3647–3653.

[40] Sherman, D.M.; Randall, S.R. Surface complexation of arsenic(V) to iron(III) (hydr)oxides: Structural mechanism from *ab initio* molecular geometries and EXAFS spectroscopy. Geochim. Cosmochim. Acta. 2003, *67*, 4223–4230.

[41] Adamescu, A.; Hamilton, I.P.; Al-Abadleh, H.A. Thermodynamics of dimethylarsinic acid and arsenate interactions with hydrated iron-(oxyhydr)oxide clusters: DFT calculations. Environ. Sci. Technol. 2011, 45, 10438–10444.

[42] Adamescu, A.; Hamilton, I.P.; Al-Abadleh, H.A. Density Functional Theory Calculations on the Complexation of p-Arsanilic Acid with Hydrated Iron Oxide Clusters: Structures, Reaction Energies and Transition States. Journal of Physical Chemistry A, 2014, 118, 5667-5679.

[43] Watts, H. D.; Tribe, L.; Kubicki, J. D. Arsenic Adsorption onto Minerals: Connecting Experimental Observations with Density Functional Theory Calculations. Minerals 2014, 4, 208−240.

[44] Adamescu, A.; Hamilton, I.; Al-Abadleh, H.A. Dispersion Effects on the Thermodynamics and Transition States of Dimethylarsinic acid Adsorption on Hydrated Iron-(oxyhydr)oxide Clusters from Density Functional Theory Calculations. Article ASAP, Journal of Physical Chemistry A. 2016

[45] Kubicki, J.D.; Kwon, K.D.; Paul, K.W.; Sparks, D.L. Surface complex structures modelled with quantum chemical calculations: Carbonate, phosphate, sulphate, arsenate and arsenite. *Eur. J. Soil Sci.* 2007, *58*, 932–944.

[46] Adamescu, A.; Gray, H.; Stewart, K.; Hamilton, I.; Al-Abadleh, H.A. "Trends in the frequencies of v(AsOxHx-1) [x = 2-4] in selected As(V)-containing compounds investigated using quantum chemical calculations", Canadian Journal of Chemistry, 2010, 88, 65-77.

[47] Adamescu, A.; Mitchell, W.; Hamilton I.; Al-Abadleh, H.A. "Insights into the Surface Complexation of Dimethylarsinic Acid on Iron (oxyhydr)Oxides from ATR-FTIR Studies and Quantum Chemical Calculations", Environmental Science and Technology, 2010, 44(20), 7802-7807.

[48] Koch, W.; Holthausen, M.C.; A Chemist's Guide to Density Functional Theory. 2000. Wiley-VCH.

[49] Parr, R. G.; Yang W.; Density-Functional Theory of Atoms and Molecules. 1989. Oxford University Press.

[50] Sholl D.S.; Steckel J.A. Density Functional Theory – A practical Introduction. 2009. Wiley.

[51] "The Nobel Prize in Chemistry 1998". *Nobelprize.org.* Nobel Media AB 2014. Web. 4 Sep 2016. <http://www.nobelprize.org/nobel_prizes/chemistry/laureates/1998/>

[52] Becke, A. D. Perspective: Fifty years of density-functional theory in chemical physics. *The Journal of Chemical Physics* 140 (18): 18A301, 2014.

[53] Lee, C.; Yang, W.; Parr, R.G. Development of the Colle-Salvetti correlation-energy formula into a functional of the electron density. *Phys. Rev. B*, 37 (1988) 785-89.

[54] Becke, A. D. Density-functional exchange-energy approximation with correct asymptotic-behavior. *Phys. Rev. A*, 38 (1988) 3098-100.

[55] Becke, A. D. Density-functional thermochemistry. III. The role of exact exchange. *J. Chem. Phys.*, 98 (1993) 5648-52.

[56] Tomasi, J.; Mennucci, B.; Cammi, R. Quantum mechanical continuum solvation models, Chem. Rev. 2005 August; 105(8)**:** 2999–3093.

[57] Grimme, S.; Steinmetz, M., Effects of london dispersion correction in density functional theory on structures of organic molecules in the gas phase. *Phys. Chem. Chem Phys.* 2013, *15*, 16031-16042.

[58] Grimme, S.; Steinmetz, M., Effects of london dispersion correction in density functional theory on structures of organic molecules in the gas phase. *Phys. Chem. Chem Phys.* 2013, *15*, 16031-16042.

[59] Hujo, W.; Grimme, S., Comparison of the performance of dispersion-corrected density functional theory for weak hydrogen bonds. *Phys. Chem. Chem Phys.* 2011, *13*, 13942-13950.

[60] Grimme, S.; Ehrlich, S.; Goerigk, L., Effect of the damping function in dispersion corrected density functional theory. *J. Comp. Chem.* 2011, *32*, 1456-1465.

[61] Kubicki, J. D. Self-consistent reaction field calculations of aqueous Al^{3+}, Fe^{3+}, and Si^{4+}: Calculated aqueous-phase deprotonation energies correlated with experimental ln(Ka) and pKa. J. Phys. Chem. A. 2001, 105, 8756–8762.

[62] Kosmulski, M., Ph-dependent surface charging and points of zero charge iii. Update. *J. Coll. Inter. Sci.* 2006, *298*, 730-741.

[63] Li, X.; Frisch, M.J. Energy-represented DIIS within a hybrid geometry optimization method," *J. Chem. Theory and Comput.*, 2 (2006) 835-39.

[64] K. Fukui, "The path of chemical-reactions - The IRC approach," *Acc. Chem. Res.*, 14 (1981) 363-368.

[65] Shared Hierarchical Academic Research Computing Network (SHARCNET). http://www.sharnet.ca.

[66] Zhang, F. S.; Li, Y. X.; Yang, M.; Li, W. Content of Heavy Metals in Animal Feeds and Manures from Farms of Different Scales in Northeast China. Int. J. Environ. Res. Pub. Health 2012, 9, 2658−2668.

[67] Jones, F. T. A Broad View of Arsenic. Poult. Sci. 2007, 86, 2−14.

[68] European Union. Council Directive 1999/29/Ec of 22 April 1999 on the Undesirable Substances and Products in Animal Nutrition. http://ec.europa.eu/food/fs/afs/substances/substances01_en.pdf.

[69] The Globe and Mail. Sales halted after arsenic found in chicken drug. (Aug. 25, 2011) http://www.theglobeandmail.com/life/health-and-fitness/sales-halted-after-arsenic-found-in-chicken-drug/article591962/

[70] U.S. Food and Drug Administration, FDA: Pfizer Will Voluntarily Suspend Sale of Animal Drug 3-Nitro (FDA Press Release June 8, 2011). http://www.fda.gov/NewsEvents/Newsroom/PressAnnouncements/ucm258342.htm

[71] Canadian Food Inspection Agency. Section E.5 List of Veterinary Drugs Not Permitted For Use in Equine Slaughtered for Food with Canadian Brand Name Examples (10 March, 2010). http://www.inspection.gc.ca/food/meat-and-poultry-products/manual-of-procedures/chapter-17/annex-e/eng/1370023131206/1370023203607

[72] Nachman, K. E.; Graham, J. P.; Price, L. B.; Silbergeld, E. K. Arsenic: A Roadblock to Potential Animal Waste Management Solutions. Environ. Health Perspect. 2005, 113, 1123−1124.

[73] Garbarino, J. R.; Bednar, A. J.; Rutherford, D. W.; Beyer, R. S.; Wershaw, R. L. Environmental Fate of Roxarsone in Poultry Litter. I. Degradation of Roxarsone During Composting. Environ. Sci. Technol. 2003, 37, 1509−1514.

[74] Cortinas, I.; Filed, J. A.; Kopplin, M.; Garbarino, J. R.; Gandolfi, A. J.; Sierra-Alvarez, R. Anaerobic Biotransformation of Roxarsone and Related N-Substituted Phenylarsonic Acids. Environ. Sci. Technol. 2006, 40, 2951−2957.

[75] Bednar, A. J.; Garbarino, J. R.; Ferrer, I.; Rutherford, D. W.; Wershaw, R. L.; Ranville, J. F.; Wildeman, T. R. Photodegradation of Roxarsone in Poultry Litter Leachates. Sci. Total Environ. 2003, 302, 237−245.

[76] Jackson, B. P.; Bertsch, P. M. Determination of Arsenic Speciation in Poultry Wastes by IC-ICP-MS. Environ. Sci. Technol. 2001, 35, 4868−4873.

[77] Cortinas, I.; Filed, J. A.; Kopplin, M.; Garbarino, J. R.; Gandolfi, A. J.; Sierra-Alvarez, R. Anaerobic Biotransformation of Roxarsone and Related N-Substituted Phenylarsonic Acids. Environ. Sci. Technol. 2006, 40, 2951−2957.

[78] Dewar, M. J. S.; Schmeising, H. N.A Re-Evaluation of Conjugation and Hyperconjugation: The Effects of Changes in Hybridisation on Carbon Bonds *Tetrahedron* 1959, 5, 166– 178.

[79] Nuttall, R. H.; Hunter, W. N.P-Arsanilic Acid, a Redetermination *Acta Cryst. C: Cryst. Struc. Comm.* 1996,C52, 1681– 1683.

[80] Arts, D.; Sabur, M. A.; Al-Abadleh, H. A. Surface Interactions of Aromatic Organoarsenical Compounds with Hematite Nanoparticles Using ATR-FTIR: Kinetic Studies. J. Phys. Chem. A 2013, 117, 2195− 2204.

[81] Farrell, J.; Chaudhary, B. K. Understanding Arsenate Reaction Kinetics with Ferric Hydroxides. Environ. Sci. Technol. 2013, 47, 8342− 8347.

[82] Antonczak, S.; Ruiz-Mpez, M. F.; Rivail, J. L., J. Am. Chem. Soc. 1994, 116, 3912−3921.

[83] Vöhringer-Martinez, E.; Hansmann, B.; Hernandez, H.; Francisco, J. S.; Troe, J.; Abel, B. Water Catalysis of a RadicalMolecule Gas-Phase Reaction. Science 2007, 315, 497−501.

[84] Du, B.; Zhang, W. Theoretical Study on the Water-Assisted Reaction of NCO with HCHO. J. Phys. Chem. A 2013, 117, 6883− 6892.

[85] Hatanaka, M.; Morokuma, K. Role of Water in Mukaiyama− Aldol Reaction Catalyzed by Lanthanide Lewis Acid: A Computational Study. J. Am. Chem. Soc. 2013, 135, 13972−13979.

[86] Adamescu, A; Hamilton, I.P.; Al-Abadleh, H.A. Density Functional Theory Calculations on the Complexation of p-Arsanilic Acid with Hydrated Iron Oxide Clusters: Structures, Reaction Energies and Transition States. Journal of Physical Chemistry A, 2014, 118, 5667-5679.

[87] Depalma, S.; Cowen, S.; Hoang, T. N.; Al-Abadleh, H. A. Adsorption Thermodynamics of p-Arsanilic Acid on Iron (Oxyhydr)- Oxides: In-situ ATR-FTIR Studies. Environ. Sci. Technol. 2008, 42, 1922−1927.

[88] Adamescu, A. Density Functional Theory Calculations on Hydrated Dimethylarsinic Acid and Iron Oxide Clusters. MSc, Wilfrid Laurier University, 2012. http://scholars.wlu.ca/etd/1125.

[89] Chabot, M.; Hoang, T. N.; Al-Abadleh, H. A. ATR-FTIR Studies on the Nature of Surface Complexes and Desorption Efficiency of p-Arsanilic Acid on Iron-(Oxyhydr)oxides. Environ. Sci. Technol. 2009, 43, 3142−3147.

[90] Adamescu, A.; Mitchell, W.; Hamilton, I. P.; Al-Abadleh, H. A. Insights into the Surface Complexation of Dimethylarsinic Acid on Iron (Oxyhydr)Oxides from ATR-FTIR Studies and Quantum Chemical Calculations. Environ. Sci. Technol. 2010, 44, 7802−7807.

[91] Depalma, S.; Cowen, S.; Hoang, T. N.; Al-Abadleh, H. A. Adsorption Thermodynamics of p-Arsanilic Acid on Iron (Oxyhydr)- Oxides: In-situ ATR-FTIR Studies. Environ. Sci. Technol. 2008, 42, 1922−1927

[92] Mitchell, W.; Goldberg, S.; Al-Abadleh, H. A. In-situ ATR-FTIR and Surface Complexation Modeling Studies on the Adsorption Thermodynamics of Mono- and Di-Substituted Organoarsenicals on Iron-(Oxyhydr)Oxides. J. Colloid Interface Sci. 2011, 358, 534−540.

[93] Arts, D.; Sabur, M. A.; Al-Abadleh, H. A. Surface Interactions of Aromatic Organoarsenical Compounds with Hematite Nanoparticles Using ATR-FTIR: Kinetic Studies. J. Phys. Chem. A 2013, 117, 2195− 2204.

[94] Tofan-Lazar, J.; Al-Abadleh, H. A. ATR-FTIR Studies on the Adsorption/Desorption Kinetics of Dimethylarsinic Acid on Iron-(Oxyhydr)Oxides. J. Phys. Chem. A 2012, 116, 1596−1604.

[95] Tofan-Lazar, J.; Al-Abadleh, H. A. Kinetic ATR-FTIR Studies on Phosphate Adsorption on Iron-(Oxyhydr)oxides in the Absence and Presence of Surface Arsenic: Molecular-Level Insights into the Ligand Exchange Mechanism. J. Phys. Chem. A 2012, 116, 10143−10149.

[96] Fish, R.H.; Brinckman, F.E.; Jewett, K.L., Fingerprinting inorganic arsenic and organoarsenic compounds in in situ oil shale retort and process waters using a liquid chromatograph coupled with an atomic absorption spectrometer as a detector. *Environ. Sci. Technol.* 1982, *16*, 174-179.

[97] Pelley, J., Common arsenical pesticide under scrutiny. *Environ. Sci. Technol. A-Pages* 2005, *39*, 122A-123A.

[98] Ravenscroft, R.; Brammer, H.; Richards, K. *Arsenic pollution: A global synthesis*; Wiley-Blackwell: Malden, MA, 2009.

[99] Lafferty, B.J.; Loeppert, R.H., Methyl arsenic adsorption and desorption behavior on iron oxides. *Environ. Sci. Technol.* 2005, *39*, 2120-2127.

[100] Ponthieu, M.; Pinel-Raffaitin, P.; Le Hecho, I.; Mazeas, L.; Amouroux, D.; Donard, O.; Pontin Gautier,M. Speciation analysis of arsenic in landfill leachate *Water Res.* 2007, 41, 3177-3185.

[101] Hayakawa, T.; Kobayashi, Y.; Cui, X.; Hirano, S.A new metabolic pathway of arsenite: Arsenic–glutathione complexes are substrates for human arsenic methyltransferase Cyt19 *Arch. Toxicol.* 2005, 79, 183–191

[102] Catalano, J.G.; Park, C.; Fenter, P.; Zhang, Z., Simultaneous inner- and outer-sphere arsenate adsorption on corundum and hematite. *Geochim. Cosmochim. Acta* 2008, *72*, 1986-2004.

[103] Adamescu, A.; Hamilton, I.P.; Al-Abadleh, H.A., Thermodynamics of dimethylarsinic acid and arsenate interactions with hydrated iron-(oxyhydr)oxide clusters: Dft calculations. *Environ. Sci. Technol.* 2011, *45*, 10438-10444.

[104] Tofan-Lazar, J.; Al-Abadleh, H.A., Atr-ftir studies on the adsorption/desorption kinetics of dimethylarsinic acid on iron-(oxyhydr)oxides. *J. Phys. Chem. A* 2012, *116*, 1596-1604.

[105] Sabur, M.A.; Goldberg, S.; Gale, A.; Kabengi, N.J.; Al-Abadleh, H.A., Temperature-dependent atr-ftir and calorimetric studies on arsenicals adsorption from solution to hematite nanoparticles. *Langmuir* 2015, *31*, 2749-2760.

[106] Farrell, J.; Chaudhary, B.K., Understanding arsenate reaction kinetics with ferric hydroxides. *Environ. Sci. Technol.* 2013, *47*, 8342-8347.

[107] Morrissey, C. A.; Albert, C. A.; Dods, P. L.; Cullen, W. R.; Lai, V. W.-M.; Elliott, J. E. Arsenic accumulation in bark beetles and forest birds occupying mountain pine beetle infested stands treated with monosodium methanearsonate. Environ. Sci. Technol. 2007, 41, 1494-1500.

[108] Morrissery, C. A.; Elliott, J. E. Toxic Trees: Arsenic Pesticides, Woodpeckers, and the Mountain Pine Beetle. Wildlife Ecotoxicology, 2011, Volume 3, 239 - 265.

[109] Shimizu, M.; Ginder-Vogel, M.; Parikh, S. J.; Sparks, D. L.Molecular scale assessment of methylarsenic sorption on aluminum oxide *Environ. Sci. Technol.* 2010, 44, 612– 617.

[110] Sabur, Md Abdus, "SURFACE COMPLEXATION OF MONOSUBSTITUTED ORGANOARSENICALS ON HEMATITE: ATR-FTIR INVESTIGATIONS" (2014). *Theses and Dissertations (Comprehensive).*Paper 1638. http://scholars.wlu.ca/etd/1638

[111] Tofan-Lazar, Julia Miss, "ATR-FTIR STUDIES ON THE KINETICS OF DIMETHYLARSINIC ACID (DMA) SURFACE COMPLEXATION WITH IRON(OXYHYDR)OXIDES" (2012). *Theses and Dissertations (Comprehensive).* Paper 1611. http://scholars.wlu.ca/etd/1611

[112] Sabur, M. A.; Al-Abadleh, H. A. Surface Interactions of Monomethylarsonic Acid with Hematite Nanoparticles Using ATR-FTIR: Adsorption and Desorption Kinetics, Canadian Journal of Chemistry, 2015, 93, 1927 - 1304.

[113] Merrick, J. P.; Moran, D.; Radom, L. An evaluation of harmonic vibrational frequency scale factors *J. Phys. Chem. A* 2007, 111, 11683– 11700.

[114] Engel, T.; Reid, P. Physical Chemistry, Second Edition. Pearson Prentice Hall, 2010.

Appendix A – Optimized Water Clusters

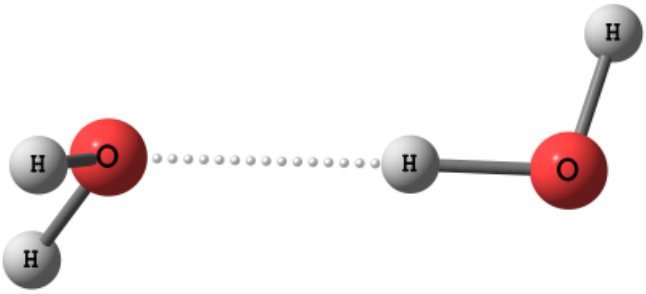

Figure A1 $(H_2O)_2$

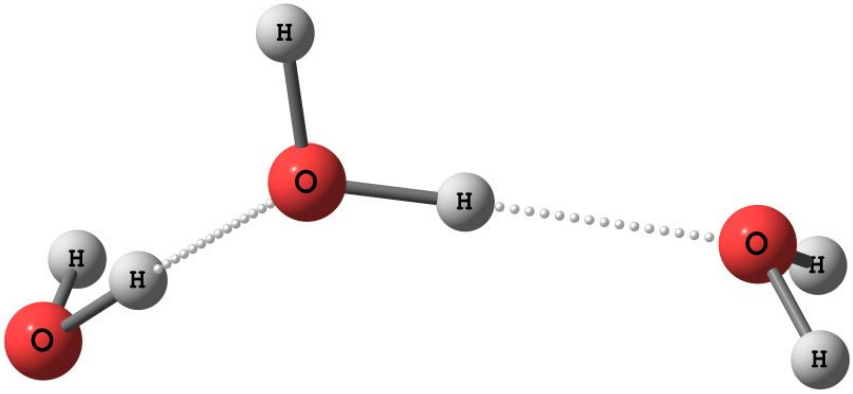

Figure A2 $(H_2O)_3$

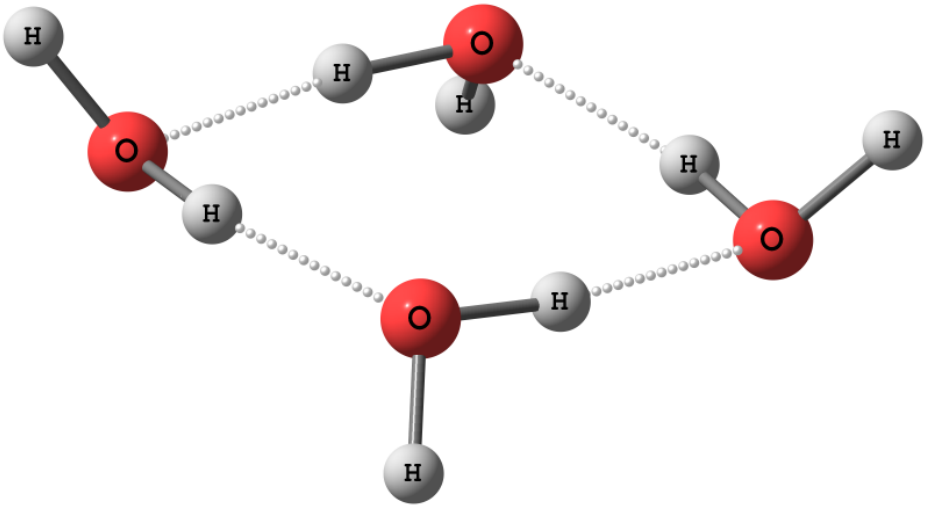

Figure A3 $(H_2O)_4$

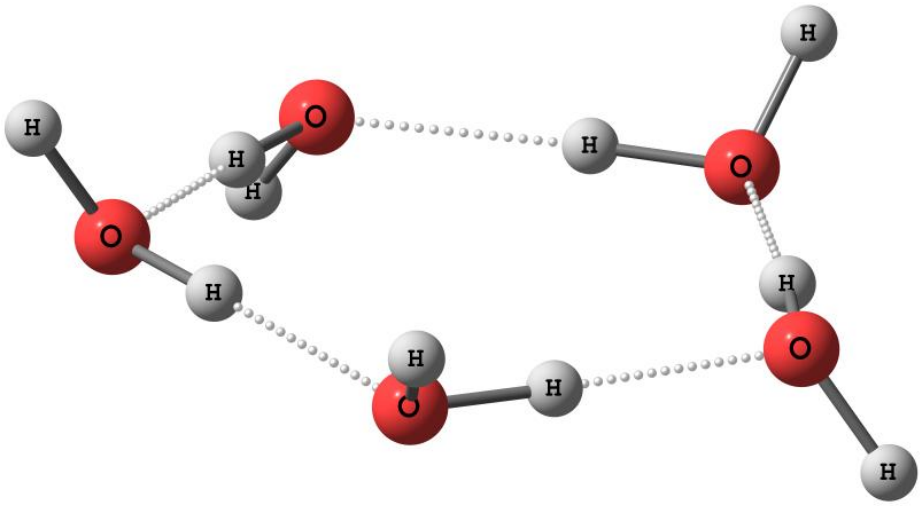

Figure A4 $(H_2O)_5$

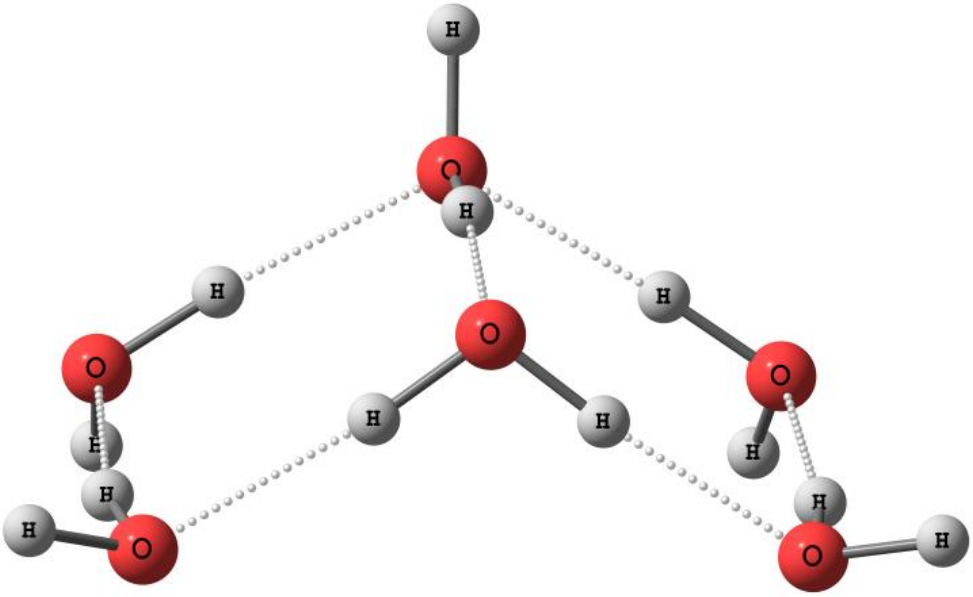

Figure A5 $(H_2O)_6$

Appendix B – Arsenate Complexes

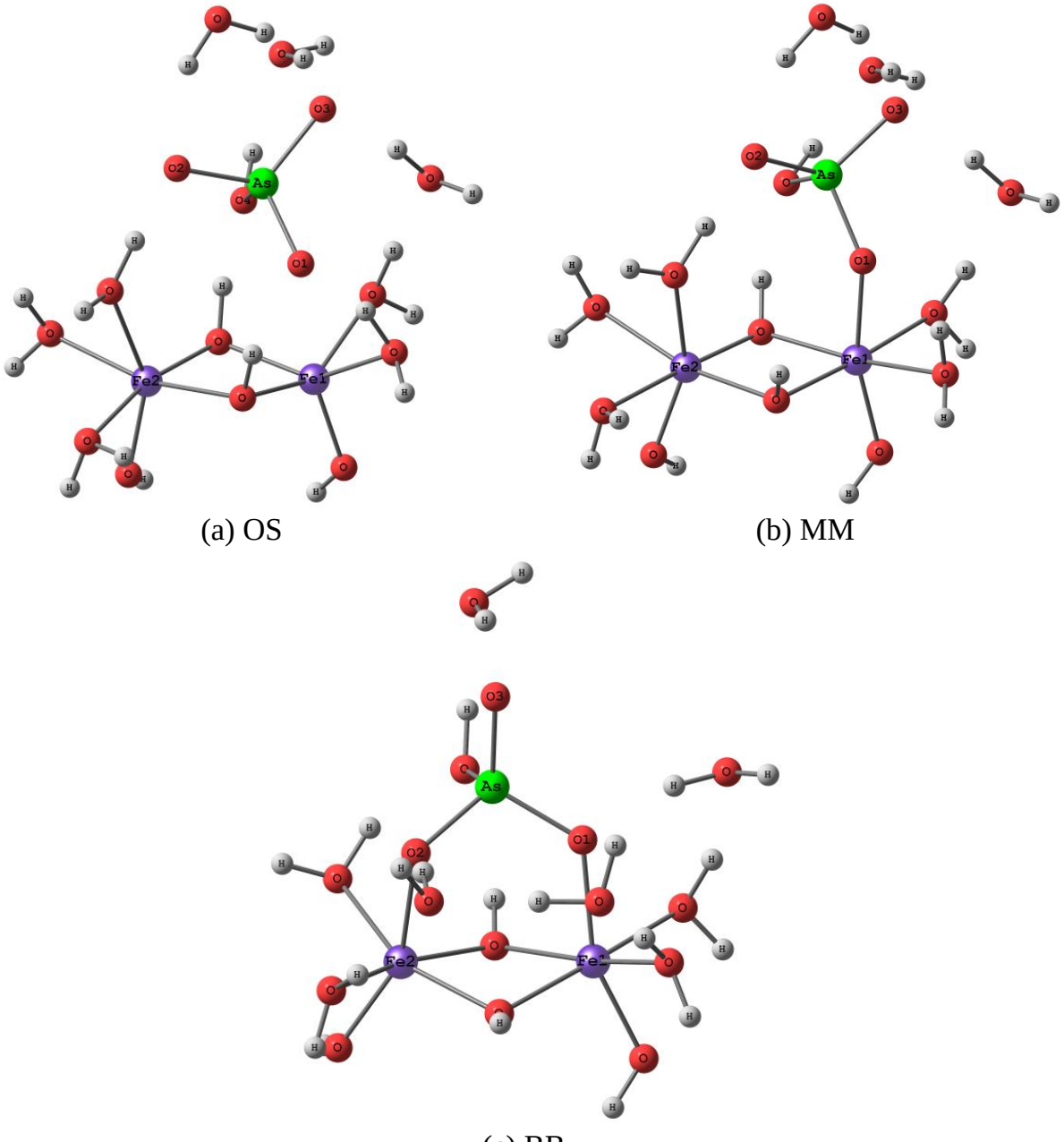

(a) OS

(b) MM

(c) BB

Figure B1. Arsenate complexes on iron oxyhydroxides: (a) outersphere (OS), (b) monodentate mononuclear (MM) and (c) bidentate binuclear (BB) calculated using B3LYP/6-311+G(d,p) with the IEFPCM solvation and GD3BJ dispersion.

Figure B1 shows the optimized geometries of arsenate OS, MM and BB complexes on iron oxyhyroxides at the same level of theory as the organoarsenicals pAsA, DMA and MMA presented in this thesis with their calculated distances shown in Table B1.

Table B1. Calculated As-O, Fe-O and As-Fe distances in Angstroms (Å) for arsenate complexes on iron oxyhydroxides shown in Figure B1. Calculated using B3LYP/6-311+G(d,p) with the IEFPCM solvation model and GD3BJ dispersion.

Complexes	**As-Fe_1**	**As-Fe_2**	**As-O_1**	**As-O_2**	**As-O_3**	**As-OH**	**Fe_1-O_1**	**Fe_2-O_2**
OS(2Fe)	4.03	4.27	1.69	1.69	1.69	1.82	-	-
MM(2Fe)	3.40	4.27	1.70	1.68	1.69	1.80	1.99	-
BB(2Fe)	3.30	3.26	1.72	1.70	1.66	1.79	2.05	2.04

The reaction pathway electronic energy calculations between the MM and BB complexes are illustrated in Figure B2 below. Figure B2 shows that the arsenate transition from from MM to BB has multiple activation barriers at +6.91, +12.6 and +12.9 kJ/mol.

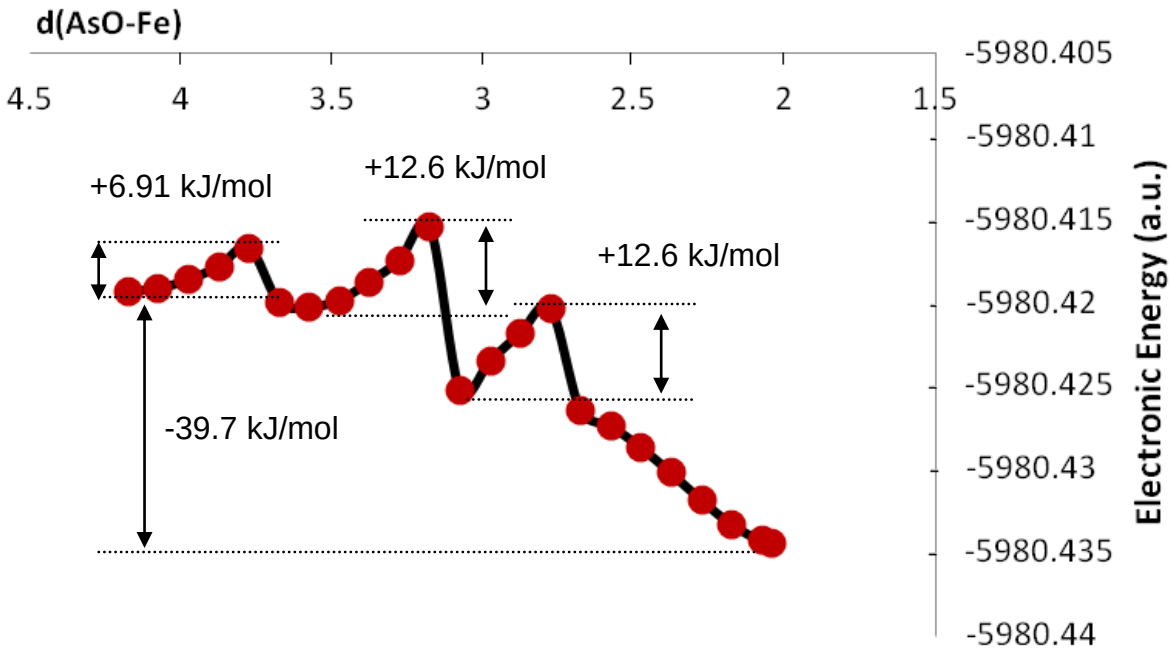

Figure B2. Electronic energies for the arsenate transition from an MM to a BB complex with iron oxyhydroxide. The BB complex is lower in energy than the MM complex by -39.7 kJ/mol and there are several small activation barriers observed.

The arsenate MM and BB complexes are lower in Gibbs free energy by -51.5 and -82.8 kJ/mol respectively, relative to the OS complex as shown in Figure B3 below.

The calculated As-O stretching frequencies for Arsenate are presented in Table B2.

Only stretching frequencies greater than 0.3 Å are shown.

Table B2. Calculated ν(As−O)* Frequencies (cm^{-1}) for Arsenate complexes with iron oxyhydroxide using B3LYP/6-311+G(d,p) with IEFPCM solvation and GD3BJ dispersion.

Arsenate Complexes	ν(As-O)	ν(As-OH)	ν(As-OFe)
OS(2Fe) Arsenate	777, 807, 824	592,	
MM(2Fe) Arsenate	783, 833	614, 625	812, 837
BB(2Fe) Arsenate	874	613	753, 783, 805

* No scaling factor was used to correct for anharmonicity.

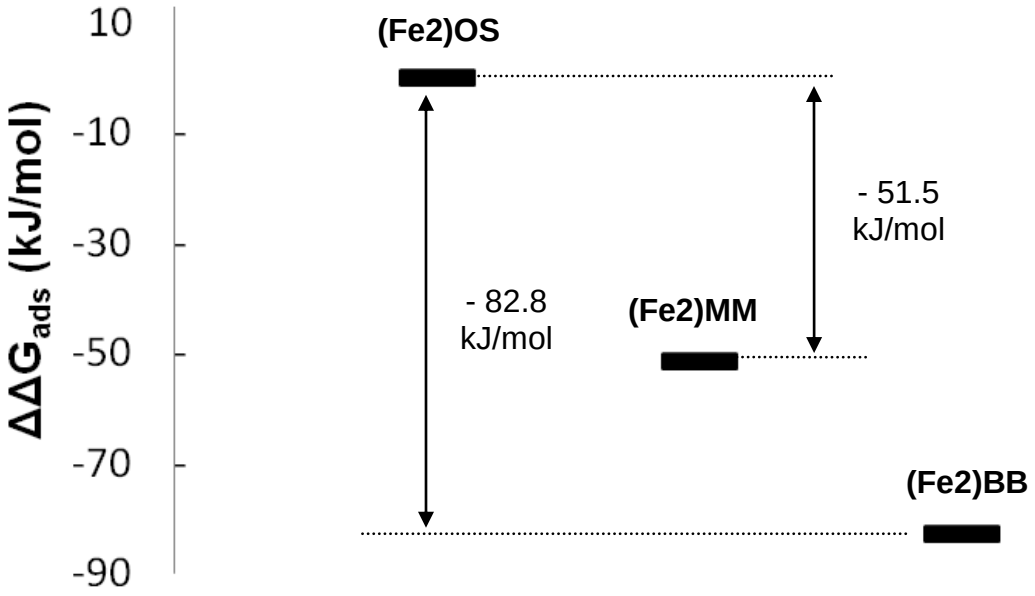

Figure B3. Difference in Gibbs free energies for arsenate adsorption onto iron-oxyhydroxide. The arsenate OS, MM and BB complexes are shown in Figure B1.

Appendix C – IRC Calculation for DMA transition state

Table C1. IRC Calculations starting from the Transition State TS2 geometry of DMA. The data shows both reverse and forward IRC calculations going toward the reactant MM(2Fe) and product BB(2Fe) complexes of DMA with iron oxyhydroxide.

	As-O distance (Å)	Electronic Energy (a.u.)
Reverse IRC Calculations	2.42186	-6137.9981203
	2.43605	-6137.9980994
	2.45024	-6137.9980866
Transition State	2.46443	-6137.9980824
Forward IRC Calculations	2.47863	-6137.9980872
	2.49282	-6137.9981015
	2.50702	-6137.9981254

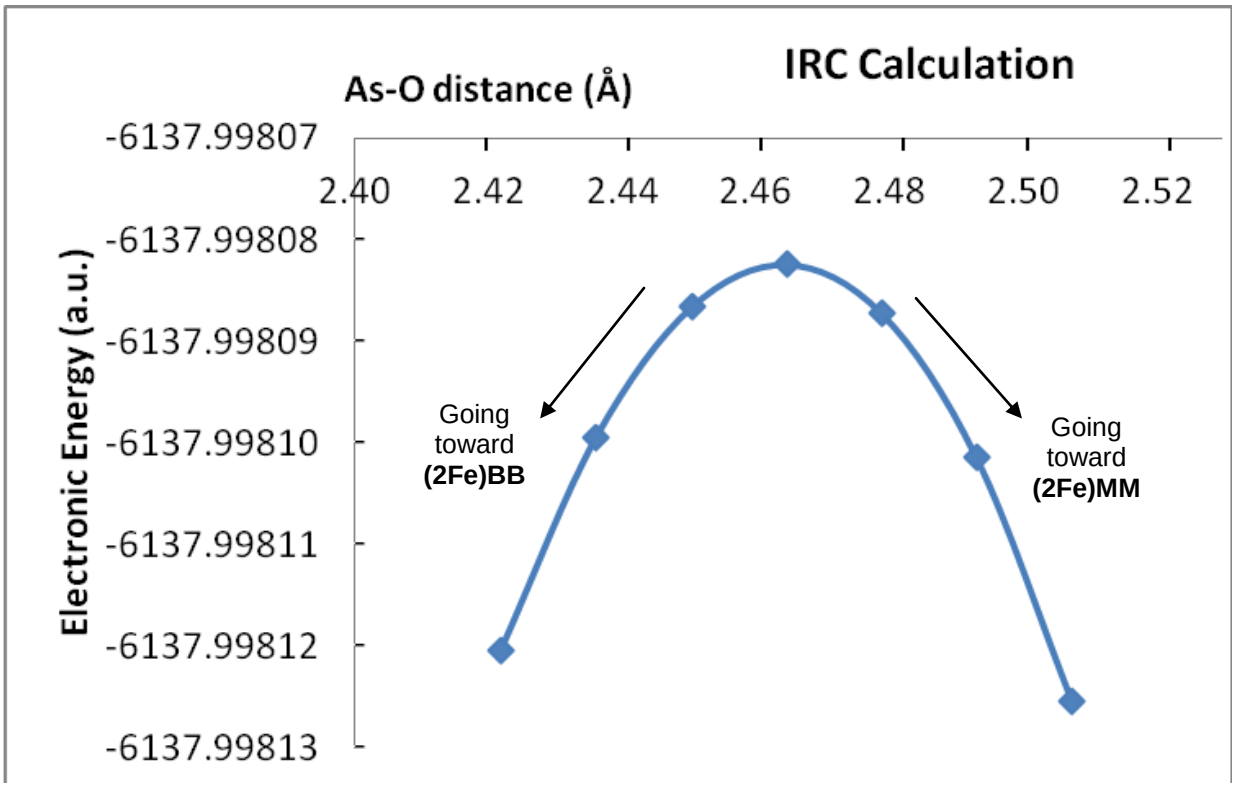

Figure C1. IRC calculations showing the DMA transition state connecting reactant (MM complex) to product (BB complex).

Appendix D – Monodentate (4Fe)MMA complex without dispersion

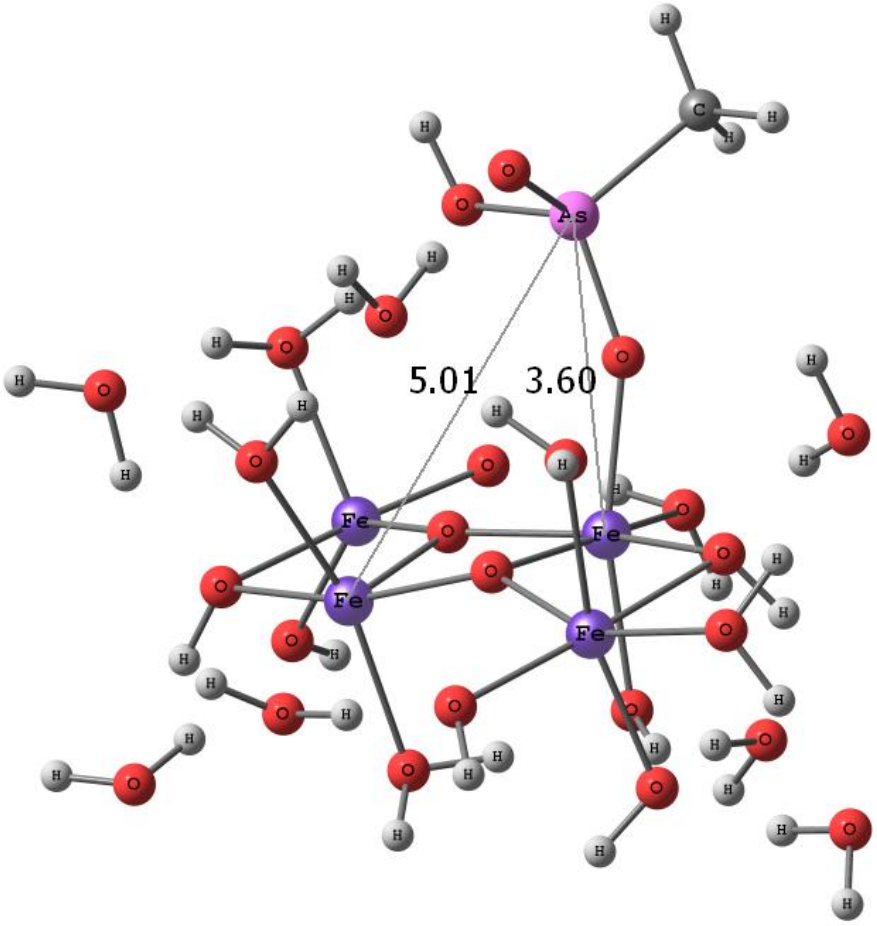

Figure D1. Monodentate MMA on modeled on an extended iron oxyhydroxide surface using B3LYP/6-311+G(d,p) and the IEFPCM solvation model.

Appendix E – Scaling factor calculations

Table E1. Data for scaling factor calculations

Molecule	Theoretical ν(As-O) (cm^{-1})	Experimental ν(As-O) (cm^{-1})	Scaled with F = 1.0065	Square of Residual
OS(2Fe) DMA	757	775	762	169.1
	803	793	808	234.1
MM(2Fe) DMA	782	793	787	34.1
	758	775	763	143.9
	782	793	787	34.1
BB(2Fe) DMA	764	775	769	35.5
	781	793	786	46.9
	799	793	804	127.1
OS(4Fe) DMA	789	793	794	1.5
	809	793	814	455.4
MM(4Fe) DMA	835	840	841	0.3
	790	793	795	4.9
	795	793	800	52.5
BB(4Fe) DMA	738	775	743	1032.3
	811	840	816	559.2
OS(2Fe) pAsA	808	795	813	336.1
	839	837	845	56.8
MM(2Fe) pAsA	821	837	826	112.0
	870	877	876	1.6
BB(2Fe) pAsA	818	837	823	185.0
	833	837	838	2.2
OS(4Fe) MMA	835	840	841	0.3
	854	840	860	385.6
MM(4Fe) MMA	855	840	861	426.1
	876	877	882	22.9
BB(4Fe) MMA	791	793	796	10.4
	862	877	868	86.7
			∑	**4556.3**